Fabrication and Characterization of Freestanding Single Crystal Diamond and Silicon Microresonators

Thèse N° 9862

Teodoro GRAZIOSI

Acceptée sur proposition du jury

Prof. L. Thévenaz, président du jury
Prof. N. Quack, directeur de thèse
Prof. S. Gröblacher, rapporteur
Prof. W. Pernice, rapporteur
Prof. G. Villanueva, rapporteur

2019

EPFL
ÉCOLE POLYTECHNIQUE
FÉDÉRALE DE LAUSANNE

Acknowledgements

Acknowledgements

Abstract

Microresonators are fundamental building blocks of any photonic integrated circuit, as they can be used as filters, modulators, sensors, and to enhance light emission. If these resonators are suspended and are free to oscillate, we can exploit the interaction of the optical and mechanical resonance. Demonstration of the fundamental interactions between the optical and mechanical fields, as well as applications based on this physics, were already presented for other material systems such as silicon, silicon oxide, or silicon nitride. Single crystal diamond is a strong candidate to realise high quality resonators due to the excellent material properties. The mechanical properties, such as stiffness, low intrinsic damping, and high thermal conductivity, are critical for mechanical oscillators with high frequency and high quality factor, which is strongly correlated to the noise of the oscillator. The wide transparency range and the low absorption enable operation in a large wavelength range spanning from near ultraviolet to far infrared. Diamond can host very bright emitters, based on defects of the diamond lattice, which can be employed as single photon sources, quantum memories, or very sensitive magnetic sensors. Chemical resistance to most acids or bases permit operations in aggressive environments. For these reasons, single crystal diamond is an attractive platform for integrated photonics and micro- or nanomechanics, and it should be possible to realize low noise optomechanical resonators.

However, compared to more established material systems, microfabrication of single crystal diamond is not easy. High quality single crystal diamond substrates are available, to date, only as bulk plates, therefore it is important to develop fabrication strategies that isolate optically and mechanically a thin diamond layer from the rest of the diamond substrate. Over the last years, several approaches have been proposed and in this work two methods will be employed: 3D milling using a focused ion beam to create micrometer sized disks supported by a narrow pillar; and etching of the bulk diamond using a plasma which is selective to particular crystal planes of the single crystal diamond. Using these processes, single crystal diamond microresonators were realized, measuring optical quality factors of 5700 and 42 000 at telecom wavelengths, respectively, and of 3100 and 10 500 at visible wavelengths, respectively.

Single crystal silicon is similar in many aspects to single crystal diamond, with the material properties being slightly worse. However, silicon benefits from decades of knowledge developed for integrated electronic circuits and integrated silicon photonics circuits. Silicon photonics is now extensively used in telecommunications to interface the optical links to

electronics. Commercial foundries started to offer silicon photonics services, either within the CMOS fabrication or with dedicated processes. Micro Electro Mechanical Systems represent a way to expand on the capability of photonic integrated circuits by providing low power and/or reconfigurable components. In this context, optomechanical oscillators were realized by postprocessing an IMEC iSiPP50G silicon photonics chip. Optical quality factors of 300 000 were measured at telecom wavelengths. Mechanical oscillations are supported at 250 MHz, with quality factors of 1800 measured at ambient conditions.

Sommario

I microrisonatori sono componenti fondamentali dei circuiti fotonici integrati, date le possibili applicazioni come filtri, modulatori, sensori, o per fotoamplificazione. Inoltre, se sospesi e liberi di oscillare, è possiblie sfruttare l'interazione tra la risonanza ottica e l'oscillazione meccanica. In bibliografia esistono dimostrazioni dell'interzione tra i campi elettromagnetici e meccanici, e di applicazioni basate su tale effetti, basati su materiali come silicio, ossido di silicio, o nitruro di silicio (e molti altri). Tra i diversi materiali in cui realizare questi componenti, il diamante monocristallino è senza dubbio un ottimo candidato, datene le proprietà eccellenti. La rigidezza, la dissipazione intrinseca del cristallo e l'elevata conducibilità termica sono importanti per oscillatori meccanici con frequenza e fattori di qualità elevati, i quali sono fortemente correlati al rumore di fase dell'oscillatore. La finestra di trasparenza larga e l'assorbimento ridotto permettono di operare con un intervallo di lunghezze d'onda che va dall'ultravioletto prossimo all'infrarosso. Il reticolo del diamante può ospitare dei difetti capaci di emettere radiazione molto luminosa. Tali difetti possono essere usati per l'emissione di fotoni singoli, come memorie quantistiche o come ottimi sensori di campi magnetici. Infine, l'inerzia chimica verso acidi e basi permette l'utilizzo in ambienti aggressivi. Per le proprietà elencate, il diamante monocristallino è una piattaforma ideale per la fabricatione di circuiti fotonici integrati e per la micro- e nanomeccanica; quindi dovrebbe essere possibile creare risonatori optomeccanici con rumore ridotto.

Sfortunatamente, la fabbricazione di strutture microscopice in diamante monocristallino non è semplice rispetto ad altri substrati più comuni. In particolare, substrati di qualità di diamante monocristallino sono, al momento, disponibili solo sotto forma di placche bulk, quindi è necessario sviluppare dei processi capaci di isolare otticamente e meccanicamente la struttura sottile in diamante dal resto del substrato. Negli ultimi anni, diverse strategie sono state proposte. Questo lavoro presenta due di queste strategie: "fresatura" tridimensionale mediante fascio ionico focalizzato, capace di creare un disco di dimensioni micrometriche, supportato da un pillastro; rimozione di parte del substrato usando un plasma selettivo verso particolari piani cristallini del diamante. Con questi due processi, sono stati realizzati microrisonatori capaci di supportare risonanze ottiche con fattori di qualità rispettivamente di 5700 e 42 000, misurati a lunghezze d'onda usate per telecomunicazioni, mentre a lungezze d'onda vicine al rosso rispettivamente di 3100 e 10 500.

Sotto diversi aspetti, il silicio monocristallino è simile al diamante monocristallino, avendo

Sommario

proprietà eccellenti seppur leggermente peggiori del diamante. D'altra parte, la fabbricazione di circuiti integrati e circuiti fotonici integrati in silicio beneficia di decenni di conoscenza e tecnologie. In particolare, i circuiti fotonici in silicio sono attualmente utilizzati nell'ambito delle telecomunicazioni per l'interfaccia tra le connessioni mediante fibre ottiche e l'elettronica. Fabbriche specializzate in semiconduttori offrono processi per realizzazione di circuiti integrati basate sulla fabbricazione di circuiti CMOS o specializzate per la fotonica. I componenti *Micro Electro Mechanical Systems* offrono la possibilità di estendere le capacità dei circuiti fotonici integrati grazie alla possibilità di realizare componenti a basso consumo energetico e/o riconfigurabili. In questo contesto, sono stati realizzati risonatori optomeccanici partendo da *chip* fabbricati con il processo iSiPP50G di IMEC. Sono stati misurati fattori di qualità ottici fino a 300 000 a lunghezze d'onda usate per telecomunicazioni, e oscillazioni meccaniche con fattori di qualità di 1800 a 250 MHz in condizioni ambiente.

Contents

Contents

List of common symbols

g_{om}	optomechanical coupling rate
g_0	vacuum optomechanical coupling strength
m	azimuthal mode number
P_{th}	optomechanical threshold power
$Q_{m,TED}$	Thermoelastic damping contribution to Q_m
$Q_{o,abs}$	optical quality factor, absorption limited
$Q_{o,ex}$	loaded optical quality factor
$Q_{o,i}$	intrinsic optical quality factor
$Q_{o,rad}$	optical quality factor, radiation limited
$Q_{o,sc}$	optical quality factor, scattering limited
Q_o	total optical quality factor
Q_m	total mechanical quality factor
r	radial mode number
r_d	disk radius
r_r	ring external radius
th_d	disk thickness
th_r	ring thickness
w_r	ring width
z	vertical mode number
Γ	mechanical dissipation
Γ_{opt}	optomechanical damping/antidamping
κ	optical cavity loss rate
κ_{ex}	external optical cavity loss rate
κ_i	intrinsic optical cavity loss rate
λ_0	vacuum wavelength
λ_c	central cavity wavelength
$\delta\lambda$	optical linewidth, wavelength space
λ_n	wavelength in the material
Ω	mechanical oscillation angular frequency
ω	optical angular frequency
ω_c	central cavity angular frequency
$\delta\omega$	optical linewidth, frequency space

1 Introduction and motivation

The work described in this thesis is focused on the fabrication and characterization of single crystal diamond microresonators, more specifically Whispering Gallery Mode structures, i. e. microdisks and microrings. Compared to other geometries, these structures have the advantage to support optical resonances over the transparency window of the material and to sustain high frequency, low dissipation mechanical modes. The fabrication procedure is also simpler due to the simple geometry and small sensitivity to size variation.

Single crystal diamond is the choice of substrate for these devices. The intrinsic properties of the material make it a great candidate for cavity optomechanics applications due to the large transparency window, spanning from near-UV to far-IR, the wide bandgap and low optical absorption, the ability to host optically active defects, as well as the high stiffness, high thermal conductivity and low intrinsic mechanical damping. The mechanical qualities highlight the potential application as a high frequency, low phase noise (opto)mechanical oscillator, with potential application as a chip scale atomic clock optical frequency reference. The possibility to create high optical quality factor cavity in single crystal diamond allow to have a low threshold power optomechanical cavity, therefore the device offers a low power consumption alternative to low(er) frequency crystalline RF oscillator, which rely on power hungry frequency dividers to be locked to the atomic transitions of chip scales atomic clock.

Initially the geometry of the devices was designed, identifying the optimal and critical dimensions of the microresonators. While the single crystal diamond properties are impressive for a number of applications, the microfabrication technology and the substrate availability is not as advanced as other substrates, like single crystal silicon. An important part of this work has been developing a reliable fabrication strategy to allow the exploitation of the diamond qualities. Finally, testing methodologies were developed to asses the quality of the fabricated devices, and to offer insight into further improvement of the fabrication strategy or the design of the microresonators.

Part of the work also followed microresonators in single crystal silicon. While there are already plenty of demonstrations of optomechanical resonators in this material, the structures

presented here are designed to be included in a commercial platform, as part of the Mems-based zerO-power Reconfigurable PHotonic ICs project (https://h2020morphic.eu/). The aim of the project is to create a general-use platform for programmable photonic integrated circuits, harnessing MEMS to enable the reconfigurability of the circuits, similarly to what it is done in electronics by a field-programmable gate array. An important focus of the project is to integrate new MEMS devices into IMEC iSiPP50G silicon photonics platform. The optomechanical resonators included in the platform are a small subset of the micromechanical devices proposed.

The manuscript is articulated over seven chapters, other than this introduction.

Chapter 2 will give an overview of the field. A mathematical description of the physics ruling an optomechanical oscillator will be given. The mathematical derivations are based on a very comprehensive book reviewing the field [1], as well as many doctoral theses [2–9]. These resources have been extremely helpful not only to understand the physics, but also to get insights into fabrication and characterization.

In chapter 3 I will introduce diamond, its properties, highlighting the ones of importance for the chosen application, and its growth. A review of diamond mechanical and optomechanical oscillators demonstrations, the fabrication strategies employed and their application will follow, comparing the results with what was achieved in other material platforms. Finally some examples of suspended diamond optical cavities will be given.

Chapter 4 will present the design of the microresonators, and the results of the numerical simulations. Then the characterization procedures will be described.

Chapter 5 and 6 present the fabrication and characterization results of the diamond microresonators. The fabrication of the diamond resonators followed two different approaches. In both cases the structures were fabricated starting from CVD-grown SCD substrates, commercially available from multiple suppliers, and both used selective etching to suspend the diamond resonators in air to achieve optical confinement in the vertical axis and to sustain mechanical oscillations. Chapter 5 is centered on the fabrication based on the Focused Ion Beam fabrication, while chapter 6 on the crystallographic etch. The fabrication was performed in the EPFL Center of Micronanotechnology (CMi) and the EPFL IPhys III/V clean room.

Chapter 7 presents the characterization results of the silicon resonators implemented in the MORPHIC platform.

In chapter 8 I will summarize the fabrication and characterization results from the previous chapters, and compare them with the current state of the art.

Finally, chapter 9 is the conclusion, outlook, and potential improvements.

2 Introduction to cavity optomechanics

The field of cavity optomechanics can be seen as the point of contact between high finesse optical cavities and low damping microelectromechanical systems (MEMS). Progress in microfabrication paved the way to increasingly smaller and higher quality resonators, where interesting interactions could be observed between the mechanical oscillator and the light confined within the optical cavity mediated by the radiation pressure. Analysis of the interaction between light and a macroscopic oscillators are reported as early as the 1970s [10–12].

The typical system used to describe an optomechanical resonator is a Fabry-Perot cavity with one mirror free to oscillate. A simple description of what is happening inside the system is the following: light from a monocromatic source (e. g. a laser) is coupled inside the optical cavity because its length at rest is a multiple of the light wavelength; one of the mirror is allowed to move, either excited by an external force (Brownian motion) or by the radiation pressure of the light inside the cavity; the mechanical oscillation causes a change in the length of the cavity, changing the allowed wavelength, thus preventing coupling from the external light source. The resulting optical signal transmitted through the cavity carries the information of this interaction under the guise of a modulation of the signal at the mechanical oscillation frequency. When the optical power is small enough, and the effect of the radiation pressure is negligible, the frequency spectrum of the optical signal can be used to measure the Brownian motion of the oscillator. Gravitational wave detection is based on the same principle: the change in the length of the very long optical cavities will modify the transmitted optical signal, the "ruler" to measure the gravitational waves [13–15]. It is evident that any noise on the position of the mirrors can be very detrimental on the detection of very weak effects like gravitational waves. An important trend in the field of cavity optomechanics is indeed the reduction of mechanical damping and the effect of the "thermal bath" that can dominate over the observation of very small effects. When the power is high enough, the light pressure interaction will start to dominate over the thermal component. Optical read-out of the interaction is still possible, with the same high power signal or an additional lower power "probe". The analysis of the optical signal thus becomes a very sensitive detection of mechanical modification of the optical cavity.
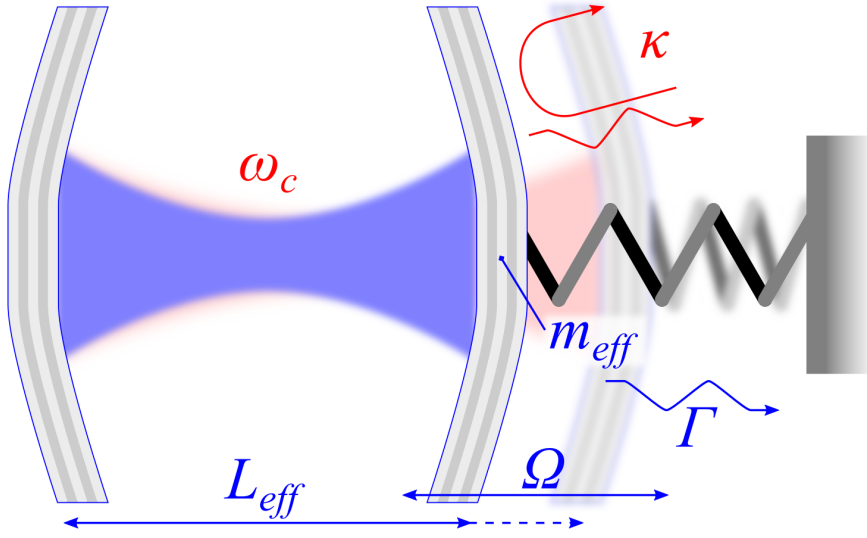
Figure 2.1 – Model of an optomechanical resonator. The system can be defined by the quantities reported here: ω_c optical cavity frequency, κ cavity loss rate, L_{eff} effective cavity length, Ω mechanical oscillation frequency, Γ mechanical damping, m_{eff} effective mass of the mechanical oscillator.

The scheme of the model optomechanical cavity is shown in figure 2.1. Other than the model Fabry-Perot cavity, optomechanical devices have several different shapes. Demonstrations have been shown using suspended mirrors, micromirrors, trampoline resonators, and membranes, in configurations similar to a Fabry-Perot Cavity [16–19]; suspended whispering gallery mode resonators: microthoroids, microdisks, and microspheres [20–23]; suspended waveguides [24, 25]; 1- and 2D photonic crystals [26–29] ; and nanorods and cold atoms in an optical cavity [30, 31]. In this thesis, the structures that will be designed, fabricated and characterized are suspended whispering gallery mode resonators. These structures allow to achieve high oscillation frequencies and high optical quality factors with a relatively relaxed fabrication requirements compared to other geometries.

2.1 Whispering Gallery Mode cavities

Optical cavities may have very different geometries, but they all follow some common physics. Like all resonators, the allowed frequency supported by the cavity depends the effective length, L_{eff}. In particular it should follow the famous equation $\lambda_c = L_{eff}/m$, where λ_c is the cavity central frequency and m is an integer. For a Fabry-Perot cavity it is rather evident the comparison with a guitar string. Looking at other cavity shapes it becomes more complex, especially to identify the correct L_{eff}. Whispering Gallery Mode (WGM) cavities can be described with the same model as first approximation, with $L_{eff} = 2\pi r_{eff}$, where r_{eff} is the effective radius of the WGM cavity. While it is close to the actual cavity radius, r_{eff} will depend
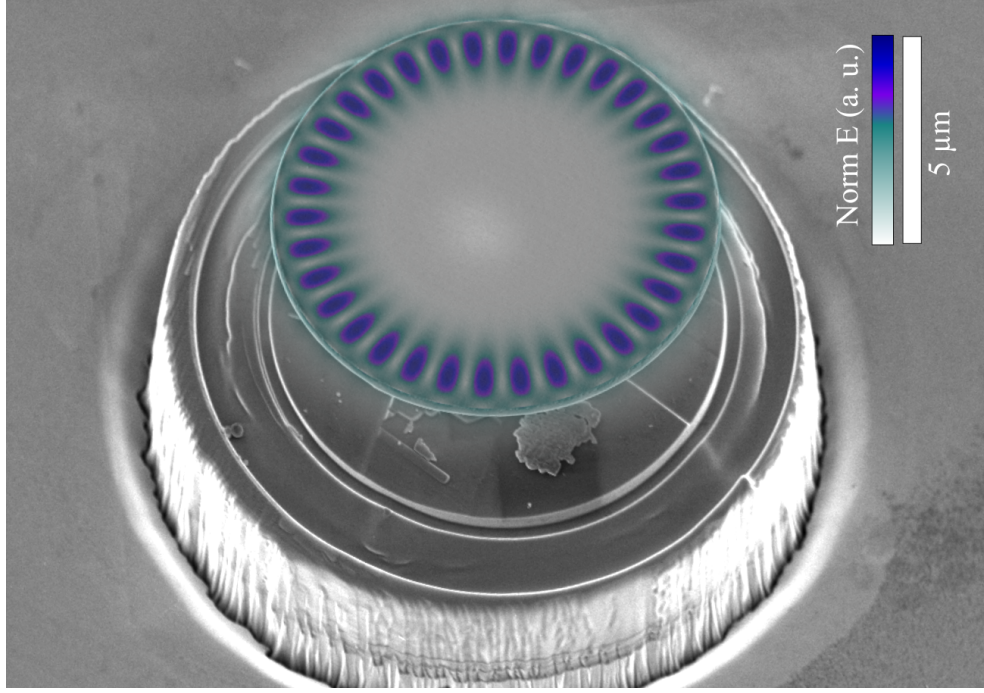
Figure 2.2 – Scanning Electron Microscope image of a diamond microdisk cavity. The overlay is the result from a finite element simulation showing the electric field norm of a cavity mode. It is confined at the edge of the disk like the sound wave travelling in a whispering gallery.

on the mode shape. From this we can define the free spectral range (FSR), respectively in wavelength space and angular frequency space, as

$$\Delta \lambda_{FSR} = \frac{\lambda_0^2}{2\pi r_{eff} n}; \tag{2.1}$$

$$\Delta \omega_{FSR} = \frac{c}{r_{eff} n}; \tag{2.2}$$

with λ_0 the vacuum wavelength and c the speed of light.

Another quantity that is often used to characterize an optical cavity is the quality factor Q. In general, Q describes the energy stored in a system. In the case of the optical cavity, the most common definition is

$$Q_o = \frac{\omega_0}{\delta \omega} \approx \frac{\lambda_0}{\delta \lambda}; \tag{2.3}$$

where $\delta \omega$ and $\delta \lambda$ are the full width at half maximum of the optical resonance in frequency and

wavelength space respectively. It is possible to define this quantity in terms of energy stored and energy dissipated, but the "spectral" definition is arguably of more practical use. Since many energy loss mechanism may contribute to the overall optical quality factor, it is possible to separate these contribution as

$$Q_o^{-1} = Q_{o,rad}^{-1} + Q_{o,sc}^{-1} + Q_{o,abs}^{-1} + Q_{o,ex}^{-1}; \tag{2.4}$$

$$Q_o^{-1} = Q_{o,i}^{-1} + Q_{o,ex}^{-1}; \tag{2.5}$$

$$\kappa = \kappa_i + \kappa_{ex}. \tag{2.6}$$

The first term, $Q_{o,rad}$, includes the contribution of radiative losses. For a WGM cavity, this is caused by the curvature of the resonator, and thus it is often referred as bending losses. $Q_{o,sc}$ takes into account the scattering at the air-cavity interface caused by the surface roughness. It may also be caused by impurities and inclusions within the cavity, but often this is negligible, especially for high quality single crystal materials. The scattering is strongly influenced by the fabrication. $Q_{o,abs}$ is the losses due to absorption of the material. It may be induced by intrinsic properties like the electronic band gap and by defect hosted within the material, or by the surface state after fabrication. These terms are included in the "intrinsic" Q, since they depend on the cavity itself. Finally, $Q_{o,ex}$ describes the losses induced by the coupling mechanism, commonly a tapered fiber or a coplanar waveguide. It is referred as the "loaded" Q. The equation can be also be expressed in terms of total cavity loss rate, κ, distinguishing the intrinsic contribution, κ_i, and the external coupling contribution, κ_{ex}.

The radiative component of Q_o is set by the design and it is one of the parameter being optimized. A way of estimating this is by integrating the energy lost at the boundary of the air cladding surrounding the resonator. In a finite element methods or finite difference time domain simulation, it is possible to use a scattering boundary condition or a perfectly matched layer (PML) to absorb the radiative field. While more computationally intensive, the PML deals better with reflection of the wave at the interface and it is generally preferable. It is composed by an artificial material with high attenuation. When either of the boundary conditions is used with an eigenfrequency solver, the results returned have an imaginary part representing the energy absorbed by the PML or scattered by the scattering boundary condition.

After defining the FSR and the Q-factor, it is interesting to define the finesse, $\mathcal{F}$. This quantity correspond to the average number of round-trips of a phonon inside the cavity, thus giving the optical power circulating inside the cavity for a given input power. It is defined as

$$\mathcal{F} = \frac{\Delta\omega_{FSR}}{\delta\omega} = 2\pi\frac{\tau}{\tau_{rt}}, \tag{2.7}$$

with $\tau = \kappa^{-1}$ being the photon lifetime inside the cavity and τ_{rt} the round trip time. For a WGM cavity, $\mathcal{F} = Q/m$, with m the azimuthal mode number. $\mathcal{F}$ is an common metric to characterize optical cavities, it gives an idea both on the linewidth and on the line spacing which can be useful for spectrum analysis, where both resolution and spectral range is relevant. In this thesis I will not use this quantity, since the operation of the optomechanical resonator is often centered around a single optical resonance. $\mathcal{F}$ and Q are closely related, and I will prefer the use of Q.

If the optical cavity contains an emitter, like a color center in the single crystal diamond matrix, the emission rate of the emitter can be amplified by a factor known as the Purcell Factor [32]

$$F_P = \frac{3Q}{4\pi^2 V}\left(\frac{\lambda_0}{n}\right)^3,$$

$$(2.8)$$

where V is the mode volume. Decreasing the mode volume is therefore desirable to enhance the light-matter interaction. The mode volume can be defined as volume integral of the electric field normalized over the maximum or average of the electric field.

Maxwell's equations in a microdisk cavity

It is possible to describe further the optical cavity by developing master equations starting from Maxwell's equations. It is possible to derive a description of the optical modes in a WGM cavity, specifically a microdisk, making few assumptions. For instance, the device should have an azimuthal symmetry, so that the refractive index does not change in the ϕ and z cylindrical directions. Secondly, the vertical confinement should restrict the propagation only in the plane of the microdisk. The main solutions are TE-like, with the electric field parallel to the disk plane, and TM-like modes, with the electric field normal to the disk plane. The solutions are not precisely TE (transverse electric) and TM (transverse magnetic) because the electric field component is not zero in the ϕ direction. However, for simplicity I will often refer to them as TE and TM in this text. The electric field distribution inside the cavity is described by Bessel functions of order m (J_m), while in the cladding outside the disk it is decaying exponentially

$$\Psi(\rho) = \begin{cases} J_m(k_0 n_{eff}\rho) & \rho \leq r_d \\ J_m(k_0 n_{eff}r)e^{-\alpha(\rho-r)} & \rho > r_d \end{cases}.$$

$$(2.9)$$

r_d is the microdisk radius, k_0 is the free space wavenumber, $\alpha = k_0\sqrt{n_{eff}^2 - n_{clad}^2}$ is the decay constant, which depend on the refractive index contrast. Given the strong vertical confinement, the effective refractive index n_{eff} is used instead of the refractive index. n_{eff} depends on the mode family (TE or TM) and on the radial order. For the first radial order,
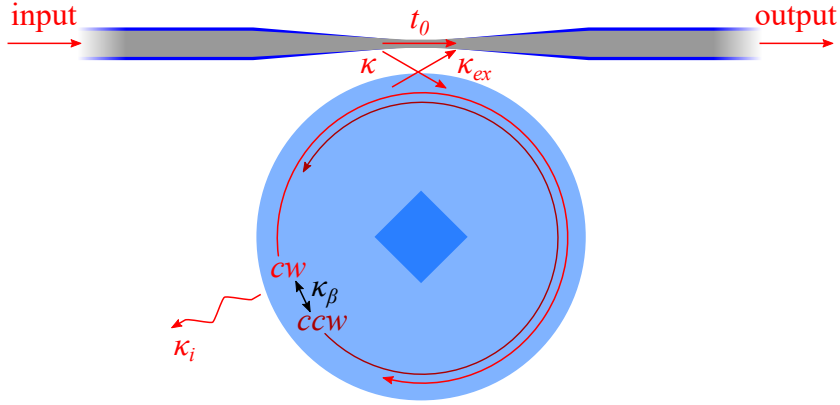
Figure 2.3 – Model of the coupling between the external waveguide and a microdisk cavity. κ_i and κ_{ex} are the intrinsic and coupling optical damping, t_0 is the portion of the input signal not coupling to the resonator, cw and ccw designate the clockwise and counterclockwise cavity modes, coupled by κ_β.

the n_{eff} can be approximated by using the value calculated in a dielectric slab with the same thickness as the microdisk, which can be determined analytically. The full derivation of this expression of the cavity modes in a microdisk can be found in the thesis of Matthew Borselli [3].

It is certainly easier to rely on numerical methods like finite element methods (FEM) or Finite difference time domain methods (FDTD) to find the mode solutions inside the optical cavity. However, full 3D FEM models require a lot of memory to compute. The formalism reported previously allows to treat the problem in a 2-dimensional geometry. A 2D-axysimmetric solution can be calculated for a certain range of azimuthal mode numbers, and the full solution can be retrieved by multiplying the 2D field by $e^{im\phi}$.

Even though the azimuthal symmetry of the refractive index is broken in the case of freestanding microring cavities, due to the supporting spokes, the derivation is still valid provided that the volume occupied by the mode is sufficiently far away from the supports. A comparison between a 3D and a 2D FEM simulation of the problem will be given in section 4.1.

Given the cylindrical symmetry, degenerate solutions to the governing equation exists, propagating azimuthally in opposite directions ($\Psi(\rho)e^{i(\pm m)\phi}$). For an ideal resonator, the two modes have the same central frequency, however, the degeneracy is lost in real devices due to the not perfect cylindrical symmetry caused by fabrication imperfection [33, 34]. This can be observed in the transmission spectrum as a "doublet" at the cavity resonance, yielding two dips at $\omega = \omega_c \pm \kappa_\beta/2$, with κ_β the separation between the two dips.

Coupling to an external waveguide

Coupling light in and out of the cavity is an important problem, and for WGM cavities it is also rather difficult. Illuminating the cavity with a microscope objective (or other free space optics)

tends to have quite low coupling efficiencies. The emission radiation of these cavities is mostly in plane [35, 36], therefore directional phase-matching schemes are preferable, especially if high coupling efficiency is desirable like in the case of optomechanical resonators. A rather simple coupling scheme is to use waveguides evanescently coupled to the WGM cavity, directly fabricated in the same layer of the device, with the ability to couple out of the substrate with fiber arrays aligned to grating couplers. This coupling scheme is common on thin films devices and it is used for our silicon on insulator (SOI) devices (chapter 7). The spacing between the resonator and the waveguide can be controlled lithographically. In other material platforms, it may not be feasible to fabricate waveguides and grating couplers, therefore an external waveguide must be used, generally a tapered fiber is used. It is an optical fiber whose diameter has been adiabatically reduced to expose part of the guided mode in the surrounding air, allowing to achieve mode overlap with an optical structure placed in proximity. To achieve single mode guidance and to expose the evanescent field the diameter has to be reduced till the order of the wavelength, $\sim 1\,\mu$m for telecom wavelengths. The system is very versatile and it is routinely employed to couple light to different resonator geometries [20, 37–43],

Both the coplanar waveguide and the tapered fiber coupling follow the same principles. Overlap of the electric fields on the resonance mode in the cavity and the guided mode in the waveguide should exist and it is possible to calculate the coupling rate by computing the overlap integral. In cylindrical coordinates, the modes of the cavity and of the waveguide are respectively $\Psi(\rho)e^{im\phi}$ and $\Psi_{wg}(\rho)e^{-i\beta_{wg}\rho\sin(\phi)}$, where $\Psi_{wg}(\rho)$ is the function describing the fundamental mode of the waveguide in the transverse direction, and β_{wg} is the propagation constant of the waveguide. Maximum overlap of the radial components, $\Psi(\rho)$ and $\Psi_{wg}(\rho)$, would occur when the waveguide and the outer edge of the resonator coincide, which is clearly not possible. However, if the quality factor of the resonance is high enough, it is sufficient that the overlap exists between the evanescent fields of the two modes. Looking at the radial components, maximum coupling will occur when $m \simeq \beta_{wg}r_d$. These therms describe the phase of the mode, therefore this coupling is phase-matched.

Depending on the resonator waveguide separation, the coupling can be in three different regimes: *under-coupled*, *over-coupled*, and *critically-coupled*. Considering the amplitude of the mode inside the cavity in relationship with the intrinsic losses and the coupling with the external waveguide, it is possible to express the transmitted power through a waveguide coupled to the cavity as [2, 44]

$$t_0 = \left(\frac{1 - \kappa_{ex}^2/\kappa_i^2}{1 + \kappa_{ex}^2/\kappa_i^2} \right)^2 . \tag{2.10}$$

When $\kappa_{ex} < \kappa_i$ the transmission starts to decrease as the optical power start to circulate in the cavity, and it correspond to the under-coupled regime as most of the power is transmitted through the waveguide. At $\kappa_{ex} = \kappa_i$, the power coupled from the waveguide completely

balances the losses, and reached the critical coupling. In this position the maximum possible power circulates in the cavity. At $\kappa_{ex} > \kappa_i$, the output coupling dominates the cavity loss and it corresponds to the over-coupled regime. In the transmission spectrum the transmission increases and the quality factor of the resonance decreases. As the linewidth increases, it may mask the doublet splitting when $\kappa > \kappa_\beta$. In fact, the splitting is generally observed in the under-coupled regime. The equation does not take into account polarization or phase-matching. If the phase-matching or polarization are not optimized, the depth of the Lorentzian peak associated with the optical resonance will decrease (i. e. less light will be coupled into the cavity).

Another option that is used to couple to WGM cavities is the use of a prism. Phase matching is ensured by changing the incidence angle of the laser [45]. However, it is generally easier to align a tapered fiber compared to a prism, especially when the size of the devices approaches the μm dimensions and multiple resonators are closely packed on the substrate.

2.2 Microdisks and microrings as mechanical oscillators

Suspended microdisks and microrings resonators naturally support mechanical oscillations. Compared to cantilevers of similar size, microdisks and microrings are much stiffer, capable of oscillating in the 100 MHz - 1 GHz range. Moreover, given the small size and mass, these structures are sensitive to very weak forces. The mechanical modes are generally calculated with finite element simulations, given the complexity of the geometry. A detailed description will be given in section 4.2. However, some mode families are commonly found in these type of structures. The most important is the radial breathing mode (RBM), where the structure expands radially. It is evident the interest for optomechanics given that this type of oscillation mode produces a large change of the optical cavity effective length.

We can define a mechanical quality factor as $Q_m = \Omega/\Gamma$, and as for the optical resonance, we can differentiate several contribution to the overall quality factor

$$Q_m^{-1} = Q_{m,clamp}^{-1} + Q_{m,mat}^{-1} + Q_{m,vis}^{-1} + Q_{m,TED}^{-1} + Q_{m,stress}^{-1} + Q_{m,surf}^{-1}. \tag{2.11}$$

$Q_{m,clamp}$ describes the losses caused by the clamping to the substrate. In the case of a microdisk, it can be expressed as [22]

$$Q_{m,clamp} = \left(\frac{c_s d}{E_{mech}} \int_{A_p} \left| \Delta z(\rho) \right|^2 dA_p \right)^{-1}, \tag{2.12}$$

where c_s is the speed of sound in the material, d density, E_{mech} is the total energy stored in

the mechanical oscillation, $\Delta z(\rho)$ is the vertical displacement amplitude, A_p is the area of the clamping. Several ways to engineer the clamping losses exists. For instance a small sized pedestal made with a more compliant material does reduce the damping [22, 46]. Commonly an inverse dependance between the quality factor and the pedestal size is found. Alternatively, it is possible to design a "phonon shield" that creates a bandgap at the desired oscillation frequency. This technique is commonly employed in optomechanical crystals [26, 47], but it is however possible to engineer the same behavior in the pedestal of a microdisk [48], although with more fabrication challenges. Finally, it is possible to select the thickness and dimension of the microdisk to obtain an oscillation node at the center where the pedestal is attached, since the displacement amplitude at the pedestal strongly influences the mechanical quality factor [22, 49]. Suspended microrings trade part of the stiffness compared to microdisk, but gain the ability to engineer the support in the device layer, which is technologically easier compared to pedestal engineering [22, 50]. This contribution is one of the dominating sources of loss for high frequency devices, especially if the connection to the substrate is not optimized [46]. Similar to the radiation losses of an optical cavity, the clamping losses can be estimated by simulating the structure with a PML.

$Q_{m,mat}$ is the contribution of the intrinsic material damping. For crystalline materials like low defect single crystal silicon or diamond, this contribution is generally negligible compared to other loss mechanisms. Internal friction and two-level thermally activated tunneling are included in this contribution, but they start to be relevant at low temperature [51].

$Q_{m,vis}$ is the viscous damping and it is influenced by the interaction of the resonator with the fluid surrounding it [52, 53]. The RBM is generally less sensitive compared to the flexural modes due typical direction and the amplitude of the oscillations: the resonator will oscillates mostly in plane, therefore not producing any squeeze film damping; when oscillating in a Brownian regime, oscillation amplitudes are of the order of few pm. Nevertheless, it is of course possible to perform experiments in vacuum and eliminate this damping mechanism.

$Q_{m,TED}$ is the contribution due to thermoelastic damping. It is caused by heat flow withing the resonator as it oscillates. Region under compression are warmed, and the opposite for tension, causing a thermal gradient and a consequent energy loss [54–56]. The Zener expression of TED is [54, 57]

$$Q_{m,TED}^{-1} = \frac{E\alpha^2 T}{dC_p} \frac{\omega\tau_Z}{1+(\omega\tau_Z)^2}; \tag{2.13}$$

$$\tau_Z \propto \frac{1}{\pi^2 D_{th}}; \tag{2.14}$$

with E Young's modulus of the material, α thermal expansion coefficient, C_p specific heat, τ_Z the thermoelastic relaxation time, and D_{th} the thermal diffusivity. The expression of τ_Z does change depending on the shape of the resonator, and the multiplication factor is related to the

thickness or the cross section. It is evident that a material with good thermal conduction, like single crystal diamond, would make this contribution small.

$Q_{m,stress}$ takes into account residual stress in the device layer. For microdisks and microrings, this term is negligible due to the fact that the structure releases any internal stress after the pedestal is formed. For other structures it is rather important and can be dominant over other forms of losses. A famous example of the expoitation of interal stress to enhance the mechanical quality is silicon nitride with residual tensile stress [18, 58]

Finally, $Q_{m,surf}$ takes into account the surface effects. Surfaces may have a large number of defects, and are sensitive to fabrication imperfections. The term starts to be relevant when the surface to volume ratio increases [59].

The Qf-product

An important figure of merit of a mechanical oscillator is the product between the mechanical quality factor and the oscillation frequency. It is directly related to the phase noise of an oscillator, which is a metric commonly used to characterize RF oscillators [60]. The mechanical quality factor can give an indication on the degree of decoupling from the thermal environment. The product of the quality factor and the mechanical frequency is a direct measure of this effect. In particular, the condition necessary to neglect thermal decoherence over one single mechanical period is $Q_m f_m = k_B T / \hbar$, where $f_m = 2\pi\Omega$; therefore to observe optomechanical effects at room themperature, the lower limit of the product is $Q_m f_m \simeq 6 \times 10^{12}$ [61].

Effective mass and thermomechanical noise

An important quantity to define is the effective mass, m_{eff}, of the mechanical oscillator, as it allows to approximate a complex oscillator to a simpler harmonic oscillator. We can think of the effective mass as the portion of the device that participates to the mechanical oscillation, and can be calculated as the volume integral of the displacement field, $\mathbf{u}(x, y, z)$ normalized to the maximum displacement and oscillator volume, V, multiplied by the real mass of the oscillator, M, [62]

$$m_{eff} = \frac{M}{V} \iiint \frac{\left|\mathbf{u}(x, y, z)\right|}{\max\left|\mathbf{u}(x, y, z)\right|} \, \mathrm{d}x \, \mathrm{d}y \, \mathrm{d}z. \tag{2.15}$$

Using the harmonic oscillator model, we can calculate the thermomechanical noise amplitude as

$$< x(\omega) > = \sqrt{\frac{4\Omega k_B T}{Q_m m_{eff}} \frac{1}{\left(\Omega^2 - \omega^2\right)^2 + (\Omega\omega/Q_m)^2}}; \tag{2.16}$$

$$\simeq \sqrt{\frac{4 k_B T Q_m}{\Omega^3 m_{eff}}}, \text{ at } \omega = \Omega; \tag{2.17}$$

where k_B is the Boltzmann constant, T the thermal bath temperature. Given the Brownian nature of this oscillation, the undriven mechanical oscillator will have random amplitudes and phase. In the frequency spectrum, the mechanical oscillations are identified by Lorentzians, whose area is proportional to the temperature.

2.3 Optomechanical resonators

When the optical cavities and the mechanical oscillator are coupled, cavity photons can exchange momentum with the mechanical oscillator. Going back to the model optomechanical system of figure 2.1, the momentum exchange gives rise to a change of the cavity lengths, which in turn changes the cavity resonance frequency. The cavity frequency as function of the moving mirror position can be written as $\omega_c(x) \approx +x \, \partial\omega_c/\partial x + \dots$. The second term of the expansion represents the frequency shift per displacement, and it is generally called optomechanical coupling rate $g_{om} = \partial\omega_c/\partial x = \omega_c/L_{eff}$.

Following [61], the optomechanical sistem can be described with an Hamiltonian. It has three terms. The first two describe the optical and mechanical mode of the system as harmonic oscillators. It assumes that only one mechanical mode and only one optical mode contribute to the interaction. The third term describes the interaction between the optical and mechanical modes.

$$\hat{H} = \hbar\omega_c \hat{a}^\dagger \hat{a} + \hbar\Omega \hat{b}^\dagger \hat{b} + \hbar g_0 \hat{a}^\dagger \hat{a}(\hat{b} + \hat{b}^\dagger); \tag{2.18}$$

where $\hat{a}^\dagger$ and $\hat{a}$ are the creation and annihilation operator of the cavity photons, $\hat{b}^\dagger$ and $\hat{b}$ the operators of the mechanical oscillation phonons, g_0 is the vacuum optomechanical coupling strength. g_0 describes the interaction of a single photon and a single phonon, and it is related to the optomechanical coupling rate as

$$g_0 = g_{om} x_{ZPF}; \tag{2.19}$$

$$x_{ZPF} = \sqrt{\frac{\hbar}{2m_{eff}\Omega}}; \tag{2.20}$$

with x_{ZPF} the zero-point fluctuation amplitude of a harmonic mechanical oscillator.

The Hamiltonian described above assumes that the effect of the optomechanical interaction is the shift of the cavity resonance with the mechanical oscillation. This system can be also called "dispersive" optomechanics. On the other hand, the effect of the mechanical oscillation can be also the change of κ_{ex}, and it is referred as "dissipative" optomechanics.

Moving boundaries and photoelastic effect

In analogy to the Fabry-perot model, g_{om} of a WGM resonator can be expressed as the ratio between the central cavity frequency and the radius, $g_{om} \simeq \omega_c / r$ [63]. In general, g_{om} can be expressed as a sum of different contributions [64]. The first is analogous to the effect of the moving mirror in the model system and it is called moving boundary contribution, g_{mb}. This term includes the effect of the physical change of the cavity length. It can be calculated as [65]

$$
\begin{aligned}
g_{mb} &= -\frac{\omega_c}{2} \iint_{A_b} (\mathbf{q} \cdot \mathbf{n}) \left[\Delta\epsilon |\mathbf{e}_\parallel|^2 - \Delta(\epsilon^{-1}) |\mathbf{d}_\perp|^2 \right] \mathrm{d}A; \\
&\simeq -\frac{\omega_c}{2} \iint_{A_{out}} \left[\Delta\epsilon |e_z|^2 - \Delta(\epsilon^{-1}) |\epsilon e_\rho|^2 \right] \mathrm{d}z \, \mathrm{d}\phi;
\end{aligned} \tag{2.21}
$$

where A_b is the resonator boundary, $\mathbf{q}$ is the normalized displacement field of the mechanical mode, $\mathbf{n}$ is the boundary normal, $\Delta\epsilon$ is the dielectric constant contrast between the resonator and the surrounding medium, $\mathbf{e}_\parallel$ is the normalized electric field component parallel to the boundary and $\mathbf{d}_\perp$ is the normalized electric displacement field component perpendicular to the boundary. Considering the microdisks and microrings RBM, $\mathbf{q} \cdot \mathbf{n} \simeq 1$ at the outer boundary, A_{out}, and $\mathbf{q} \cdot \mathbf{n} \simeq 0$ at the top and bottom boundary, therefore the moving boundary contribution will be the strongest for the first order radial optical modes, and in particular the TE$_{1,m}$ modes, since the electric field will be predominantly at the outer boundary of the cavity. In the simplified equation, e_z and e_ρ are the vertical and radial normalized electric field components in cylindrical coordinates. If we rewrite the equation of the electric field in cylindrical coordinates as $e_z(\rho, \phi, z) = e_z(\rho, z) e^{im\phi}$ and $e_\rho(\rho, \phi, z) = e_\rho(\rho, z) e^{im\phi}$, the equation

can be further simplified since $\int_0^{2\pi} \left| e^{-im\phi} \right|^2 \mathrm{d}\phi = 2\pi$:

$$g_{mb} \simeq -\frac{\omega_c}{2} \left[\frac{\Delta\epsilon \int_{L_{out}} \left| E_z(\rho, z) \right|^2 \mathrm{d}z - \Delta(\epsilon^{-1}) \int_{L_{out}} \left| \epsilon E_\rho(\rho, z) \right|^2 \mathrm{d}z}{\epsilon \iint_{section} \left| \mathbf{E}(\rho, z) \right|^2 \mathrm{d}\rho \, \mathrm{d}z} \right]; \tag{2.22}$$

with L_{out} representing the outer edge of the cavity vertical cross section. The contribution can be estimated from the results of a 2D axysimmetric FEM simulation.

A second effect that may contribute to the change of the effective cavity length is the photoelastic effect, when a strain field causes a change in the material refractive index [27].

$$
\begin{aligned}
g_{pe} \simeq \frac{\omega_c \epsilon_0 n^4}{2} \iiint_V \{ & 2\Re(e_x^* e_y) p_{44} S_{xy} \\
& + |e_x|^2 [p_{11} S_{xx} + p_{12}(S_{yy})] \\
& + |e_y|^2 [p_{11} S_{yy} + p_{12}(S_{xx})] \\
& + |e_z|^2 [p_{12}(S_{xx} + S_{yy})] \} \, \mathrm{d}x \, \mathrm{d}y \, \mathrm{d}z,
\end{aligned}
\tag{2.23}
$$

where $\mathbf{S}$ is the strain tensor, $\mathbf{p}$ is the photoelastic tensor [66]. For a general geometry, also the strain z components (S_{zz}, S_{xz}, S_{yz}) should be taken into account, but for a RMB the strain in these direction is mostly zero.

Amplification and Cooling of the mechanical motion

By driving the optical cavity with an external laser field, the mechanical motion can be controlled [61]. The optical cavity field can be expressed as an average field, $\bar{a}$, and a fluctuating field $\delta\hat{a}$. Depending on the pump laser detuning Δ, the third term of the Hamiltonian becomes

$$\hat{H}_{int} = \hbar g_0 \bar{a} \left(\delta\hat{a}^\dagger \hat{b}^\dagger + \delta\hat{a}\hat{b} \right), \text{ for } \Delta > 0; \tag{2.24}$$

$$= \hbar g_0 \bar{a} \left(\delta\hat{a}^\dagger \hat{b} + \delta\hat{a}\hat{b}^\dagger \right), \text{ for } \Delta < 0. \tag{2.25}$$

Deriving the equations of motion from the Hamiltonian, it is possible to define a backaction rate of the optomechanical system as [4]

$$\Gamma_{opt} = A_- - A_+ = g_0^2 \bar{a}^2 \left(\frac{\kappa}{\kappa^2/4 + (\Delta + \Omega)^2} - \frac{\kappa}{\kappa^2/4 + (\Delta - \Omega)^2} \right). \tag{2.26}$$

The two terms of the equation describe the phonon annihilation, A_-, and creation, A_+, rates.

The backaction rate can modify the mechanical damping, and we can define an effective mechanical damping rate as $\Gamma_{eff} = \Gamma + \Gamma_{opt}$. Depending on the sign of the detuning Δ, Γ_{opt} can be negative or positive, effectively amplifying or damping the mechanical oscillation. We can distinguish two different regimes by the ratio between the optical linewidth and the mechanical oscillation frequency. In the unresolved sideband regime, $\kappa > \Omega$, the maximum and minimum of Γ_{opt} are approximately at $\Delta \approx \kappa/2$, while in the sideband resolved regime, $\kappa < \Omega$, at $\Delta \approx \Omega$. With negative (blue) detuning, it is possible to reach a condition where $\Gamma_{eff} = 0$ if sufficient power is circulating in the cavity. The optomechanical system enters a regime of regenerative self sustained oscillations, often referred as "phonon lasing" or parametric amplification [67]. When the threshold power is reached, the Lorentzian peak associated with the mechanical oscillation increases in amplitude dramatically, while its linewidth decreases, approaching the optical cavity linewidth [21, 68, 69]. An alternative way to express the regime is indicated by the optomechanical cooperativity, C, reaching unity when the parametric amplification is reached,

$$C = C_0 \bar{a}^2 = \frac{4g_0}{\kappa\Gamma} \bar{n}_{cav} = 1 \tag{2.27}$$

where $\bar{n}_{cav} = \bar{a}^2$ is the average number of photons in the cavity, and C_0 is the single photon cooperativity.

By detuning the laser in the other direction, Γ_{opt} is always positive. In this regime the opposite effect occurs, as the backaction increase the damping of the system. In this regime optomechanical cooling of the oscillator can occur as the laser field will extract phonons from the cavity [70, 71]. However, since the laser needs to be red detuned from the cavity, additional experimental requirements should be considered. In fact, an optical cavity at sufficiently high power experiences a shift of ω_c as the pump frequency approaches the center of the resonance. As more power circulates in the cavity, absorption induced heating changes the refractive index of the material and a typical instability at the central frequency can be observed [72]. To counteract this effect, stabilization techniques can be used [73]. For our experiments we are interested in the blue side of the optical resonance for the amplification, and active stabilization of the cavity may not be required.

With the same optomechanical system more interaction types have been demonstrated, including optomechanically induced transparency (OMIT) [73–75], optical wavelength conversion [76], and squeezed light generation [77]. The requirements are more stringent, since resolved sideband regime, $\kappa \ll \Omega$, and strong coupling regime, $g > k$, may be necessary.

2.4 Applications

Due to the very small linewidth in the parametric amplification regime, optomechanical cavities can be used as very sensitive detectors. Due to strong optical confinement, especially in photonic crystal structures, detection of mechanical displacement is possible with high sensitivity by analyzing the optical signal coming from the cavity. By amplifying the signal via radiation pressure, the sensitivity of displacement measurements can be drastically reduced to reach a noise equivalent to the standard quantum limit (SQL) and beyond [78, 79], below the thermal noise level. High sensitivity and high bandwidth accelerometry was demonstrated as well [80]. The high intrinsic mechanical quality factor achievable in these structures paired to a small test mass ensures measurements bandwidth higher than commercial MEMS accelerometers, with the added benefit of the ability to cool the thermal motion of the test mass. The mechanical resonance frequency is very sensitive to small perturbations, and optomechanical oscillators have been used to detect small masses, down to the sub-pg level [81, 82]. Of course, if used in an unperturbed environment, optomechanical oscillators benefit from the small oscillation linewidth if used as a frequency reference [21, 83, 84].

Other applications include on-chip optical processing exploiting OMIT and optomechanically mediated wavelength conversion. A more complete description of applications of cavity optomechanics can be found in the review by Michael Metcalfe [85].

3 Diamond mechanical and optome-chanical resonators

For nanomechanics and photonics applications, diamond is a strong material platform thanks to its excellent properties. The large bandgap makes the material transparent in a wide range of wavelength, from ultraviolet to far-infrared. Multiphoton absorption is also very low for most of the transparency range. This large bandgap also allows to host a large number of quantum emitters, the diamond color centers, which will be presented briefly in the next paragraph. It is also a high (~2.4) refractive index material, allowing to fabricate photonic structures with very small mode volumes. Mechanically it is known to be very stiff and hard, with Young's and Hardness moduli one order of magnitude higher than silicon. It has also very low intrinsic damping, and, together with the high thermal conductivity, it allowed to fabricate high frequency, low dissipation mechanical oscillators, which examples will be presented in section 3.2. The optical and mechanical qualities make diamond a particularly attractive platform for optomechanics, where high cooperativity regimes can be reached. Other than optomechanics and photonics, diamond is interesting also for micro-optical components and non-linear optics. The formers benefit from the high refractive index and the large laser-induced damage threshold, allowing to be used for lenses, grating and windows in high power applications [86–92]. The latter from the large Raman shift and Raman gain, with a number of demonstrations of diamond Raman lasers presented over the years [93–96]. Table 3.1 lists few of these material parameters of single crystal diamond compared to nanocrystalline diamond and single crystal silicon. While the grain boundaries of NCD degrade the quality of the single crystal material, in many cases they are still better than single crystal silicon.

To fabricate high quality factor devices, high quality substrates are critical. One important technological limitation is the availability of high quality substrates. In recent years, high quality single crystal plates started to be commercially available, allowing researchers to focus on the development of diamond devices. Two technologies are used to grow synthetic single crystal diamond plates, High Pressure High Temperature (HPHT) [104] and Chemical Vapor Deposition (CVD), in particular microwave plasma CVD [105]. While both technologies can offer sufficiently pure substrates, CVD grown diamonds can be obtained with less defects, and are generally preferred in photonics applications. CVD growth can produce different

Parameter	Single Crystal Diamond	Nanocrystalline Diamond	Single Crystal Silicon
Young's Modulus (GPa)	1080 - 1155 [97]	500 - 1120 [98]	165 [99]
Hardness (GPa)	50 - 110 [97]	35 - 98 [98]	13 [100]
Density (kg/m^3)	3520 [101]	3300 - 3510 [98]	2330 [101]
Thermal Conductivity (Wm^{-1}K^{-1})	2200 [101]	12 - 1370 [98]	140 [101]
Thermal Expansion Coefficient (K^{-1})	0.8 - 0.9 $\times$ 10^{-6} [97]		2.6 $\times$ 10^{-6} [102]
Sound Velocity (m/s)	18000 - 19000 [97]	15700 - 17980 [98]	8300 [101]
Raman Shift (cm^{-1})	1332 [97]		520 [103]
Bandgap (eV)	5.47 [101]		1.12 [101]
Transparency Range (μm)	0.22 - 20 [101]		1.1 - 6.5 [101]
Refractive Index	2.4 [101]		3.5 [101]

Table 3.1 – Material Properties of single crystal diamond and nanocrystalline/ultrananocrystalline diamond compared to single crystal silicon. For each value the reference is reported in the square parenthesis.

types of diamond substrates. Single crystal plates can be grown starting from a single crystal diamond seed (usually an HPHT crystal, {100} orientation) [106–108]. This process is called homoepitaxy. Commercially available CVD single crystal substrates are usually grown with this technique. The CVD gem is then laser cut into smaller plates and polished. Given that the starting seeds are generally small and the low growth speed in on the lateral directions, plates larger than few mm are very expensive. Initial polishing is perfomed using a scaife-polishing technique [109, 110]. This polishing however does not produce a surface suitable for integrated photonics due to the presence of subsurface damage and pits and lines left in the surface [111, 112]. Additional polishing, including non contact techniques, are required to prepare the surface before photonic devices can be structured. Using the same deposition method on a different substrate (heteroepitaxy) usually produces a polycrystalline film. Nevertheless, single

crystal diamond can be grown heteroepitaxially on an iridium substrate, since the nucleation density is high and the nuclei orientation has a narrower distribution. When a sufficiently thick CVD layer is deposited, a large single crystal with low defect density can be achieved [113]. However, depositing directly a thin single crystal layer over a low index or sacrificial layer is not yet demonstrated, therefore a "single crystal diamond on insulator" wafer could be fabricated using bonding techniques, as of the knowledge and technology available currently. Poly and nanocristalline diamond can be a possible alternative to create large scale diamond on insulator substrates, with the trade-off of lower material quality.

3.1 Color centers

Excellent books [114] and review articles[115] compiled a great overview of many defect based sources in diamond and their applications, therefore a complete and detailed review of diamond color centers goes beyond the scope of this review. However, a small description of the structure and working principle of the main color centers will be beneficial, since a mechanical stress field can substantially modify the emission characteristics and many examples listed in the following diamond (opto)mechanics review aim to achieve coupling between color centers and mechanical motion.

Reliable observation of color center luminescence occurs only in single crystal diamond or nanodiamonds, while photoluminescence in poly an nanocrystalline films is strongly influenced by the grain boundaries [116]. Thanks to the wide bandgap, diamond can host a large number of optically active defects that can emit from ultraviolet to far infrared. These defects are responsible for the coloration in natural diamond, and the one emitting in the visible have been extensively studied over the years due to the most famous application of diamond, jewelry. Moreover, since a lot of these defects, or color centers, are particularly bright and can be observed isolated inside the diamond matrix, they are studied also as quantum system [117]. Of particular interest is the application of color centers as single photon sources.

Two of the most commonly studied defects are the nitrogen vacancy and the silicon vacancy centers. Figure 3.1 shows the lattice and the electronic structure of these defects. The NV center is formed by a nitrogen in a lattice position and an adjacent carbon vacancy, and it can exist in multiple states depending on the charge distribution. These defects are rather common both in natural diamond and in synthetic diamond, and they can be included in a controlled manner in the diamond with ion implantation. The negatively charged state (NV$^-$) is potentially the most interesting. It has a long electron-spin lifetime and it maintains good properties at room temperature [119, 120], and it exhibits coherent optical effects [121, 122]. The center has triplet states in the ground ($^3A_2$) and the excited (^3E) states, which can be manipulated by magnetic or electric field or by a stress field [123]. This enables the NV$^-$ to read single spins and it opens the way for new technologies in the field of nanomagnetometry, neuroscience, biology, and sensing [124–128].

Other than electric or magnetic field manipulation, it has been shown that color centers can
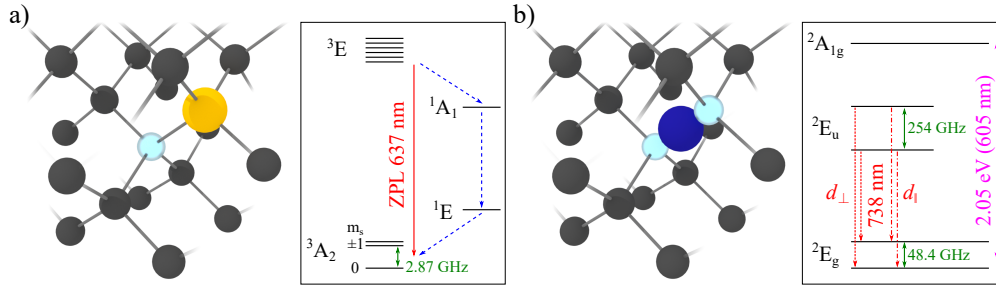
Figure 3.1 – Strucuture of two common diamond color center defects. a) Nitrogen vacancy lattice structure. Carbon atoms are colored in dark grey, nitrogen atoms in yellow, and the vacancy is represented by the cyan sphere. The electronic structure of the negatively charged nitrogen vacancy (NV⁻) is shown in the box on the right. The solid red line indicates the allowed optical transition, the dashed blue line the non-radiatiative transition, the solid green the magnetic transition [115]. b) Silicon vacancy lattice structure. The silicon atom is colored blue, and it occupies an interstitial site of the diamond lattice. The electronic structure of the negatively charged silicon vacancy (SiV⁻) is shown in the box on the right. The red lines indicates the allowed optical transition, the dashed blue line the non-radiatiative transition, the solid green the magnetic transition. There are 4 optical transitions allowed, yielding a typical quadruplet photoluminescence emission at 738 nm [118].

be coupled to a stress field, for example in a micro or nano-mechanical resonator. Similar interactions between mechanical motion and a quantum system have been demonstrated previously with quantum dots embedded in a mechanical oscillator. The strain induces a shift of the electronic levels of the quantum system, and it is particularly interesting when electronic states can be degenerate in certain conditions like spin states [129–131]. In the case of the NV⁻ center, a GHz stress wave can split the $|+1\rangle$ and $|-1\rangle$ spin states [132]. However the stress coupling coefficient is found to be smaller compared to other coupling mechanism like a magnetic field, therefore large stress is required. Embedding a single center inside the mechanical oscillator enables operation within the sideband resolved regime [133], which allows to observe effects like phonon cooling and lasing [134], similarly to what has been demonstrated with optomechanical oscillators.

The exploitation of color centers has been a strong motivation to develop nanofabrication of single crystal diamond. One of the main challenges is related to the collection of the emitted photons. Given the high refractive index of diamond, most of the light emitted from the color center is reflected at the interface. Substantial work was done to create solid immersion lenses at the color center location [135–139] or create nanowires [140] to enhance the emission outside the diamond and increase the collection efficiency. As for other quantum emitters, color centers also benefit from the inclusion in an optical cavity, in order to have a Purcell enhancement of the emission [141].

While microfabrication allowed to enhance the collection rate of photons from NV centers and coupling to mechanical oscillators, it can induce modification of the fluorescence. For

instance, the lifetime of NV⁻ is dependent on the host material, displaying shorter lifetimes in bulk single crystals compared to nanodiamond [120, 142, 143]. By bringing the center close to the surface, spectral broadening start to be observed, indicating that the electronic states are modified by the presence of surface impurities [144]. Sensitivity of the color center to the magnetic environment can be enhanced when it is closer to the surface, and it can enable truly nanoscale sensing due to the intrinsic size of the defect. Moreover, embedding the color center within a nanoscale resonator may be required to access the GHz range of mechanical oscillation to couple efficiently the strain to the spin states. Of course, the modification of the center fluorescence has to be taken into account. It should be noted that significant broadening is found for very shallow defects (<2 nm), and the surface stability of NV in diamond is unmatched by other solid-state spin systems [144]. However, the charge state of the NV center (NV^0 or NV⁻) is influenced by the distance to the surface. Changing the surface terminations may convert stable NV⁻ to NV^0 [145, 146]. This behavior may be a limitation for applications where the fluorescence from the negatively charged state is desired.

A large part of the work on diamond color centers has been performed on NV defect, however, the silicon vacancy defect also can emit single photons and it has a narrow ZPL with weak phonon sidebands [147]. Moreover, the symmetry of the defect (see figure 3.1) makes it more robust to the environment [148]. The emission at ∼ 740 nm could also be exploited for gas sensing (in particular NO_2 [149]). In the last years more attention has been given to this defect, with encouraging reports of techniques to deterministically place the emitter inside an optical cavity [150–153]. Strain tuning of this color center is possible as well. The diagram in figure 3.1(b) shows the electronic structure of a SiV⁻ when no magnetic or strain field is applied. The spin-orbit coupling separates the ground and upper states by several GHz, producing 4 allowed optical transition. When a magnetic field is applied, the degeneracy is further broken and each level is separated in two different spin states. A strain field can significantly impact the coherence and relaxation time of the spin states [154, 155].

3.2 Diamond (opto)mechanical oscillators

Initial studies using poly- and nano-crystalline diamond (PCD and NCD) film showed encouraging results with regards to the mechanical quality of diamond resonators. One of the main motivations to move from polycrystalline silicon to polycrystalline diamond is the higher Young's modulus allowing for higher oscillation frequency RF oscillators, with the aim to extend the operating range in the higher frequency bands [46, 156]. CVD deposited polycrystalline diamond can be easily integrated on different substrates, and can be processed in a CMOS compatible process. High Qf-products of the order of 10^{13} Hz, both in air and in vacuum [46], were achieved. Further analysis of the loss mechanisms in poly- and nano-crystalline diamond based devices showed a lower thermoelastic damping compared to polysilicon. Analyzing the damping of NCD cantilevers, Hutchinson et al. [157], found the thermoelastic damping contribution to Q_m to be negligible. The behavior can be explained by comparing the thermal constant of the cantilevers to the mechanical oscillation periods. The
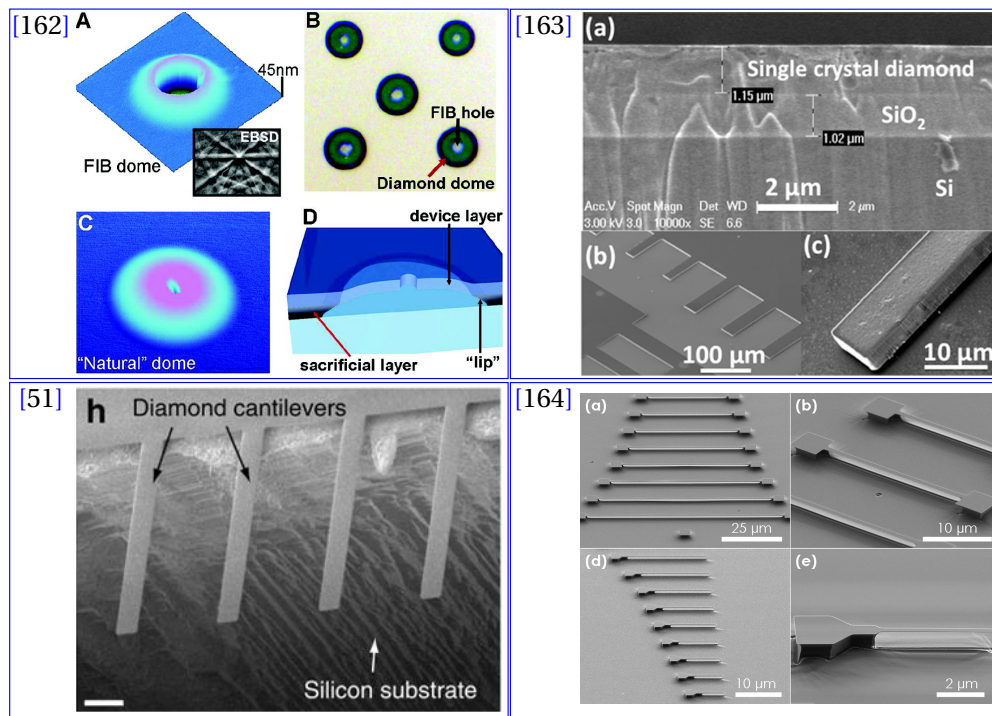
Figure 3.2 – Examples of mechanical oscillators in single crystal diamond. [162] Dome shaped resonators fabricated with the "smart-cut" method. [51, 163] Cantilevers fabricated by bonding and thinning a thich diamond plate. The absence of the amorphous carbon layer yields high mechanical quality factors. [164] Cantilevers fabricated with the "angled etching" technique starting from a bulk substrate. In subfigure (c) the typical triangular cross section is shown.

high thermal conductivity of the diamond contributed making the thermal constant much shorter than the period. Other studies in the same direction [57, 158–160] confirmed the behavior by breaking down the different contributions to the mechanical damping.

Temperature gradients in oscillators causing local volume changes are the root cause of the thermoelastic damping. This contribution (Zener damping) is inversely proportional to the specific heat and the thermal diffusivity of the material [54, 57]. Compared to polysilicon, PCD and NCD have of course an advantage, however, the grain boundaries degrade the heat transport properties, especially at high oscillation frequency (GHz) when the inter- and intracrystalline damping starts to be dominating [161]. From this point of view, single crystal diamond devices should have significantly lower thermoelastic damping at all frequencies.

Overall, SCD should be better suited to many applications in micro- and nano-mechanics compared to PCD and NCD. As discussed previously, it is very challenging to grow single crystals on a sacrifical substrates like for the poly- and nano-crystalline variant. Nevertheless, several examples are available of mechanical oscillators in single crystal diamond. The main fabrication challenge is the availability of high quality single crystal substrates only in bulk form. To create suspended micro- and nanometer sized devices it is necessary to remove part

of the diamond below the device. This is of course challenging because no strong chemical selectivity can be exploited. One technique is to create a sacrificial layer by ion irradiation. High energy (~100 keV) light ions (He, C, ...) can selectively damage a layer below the diamond surface, creating an amorphous layer that can then be selectively removed with plasma or electrochemical etching [165–168]. With this technique, Zalalutdinov et al. [162] realized 70 nm thin dome resonators in SCD. A strong dependence of the mechanical quality factor on the temperature and the oscillation frequency was found, suggesting that the technique chosen for the etching of the sacrificial layer did not reliably remove the amorphous carbon. In particular, the internal friction in the MHz frequency range and thermal dissipation of amorphous carbon are the dominant source of losses in the fabricated structures. Indeed, Wu et al. [169] demonstrate high mechanical quality factor (1 000 000 at ~400 kHz) after thorough etching of the amorphous carbon layer. Their etching step consisted of thermal annealing at 500 °C in air. The quality factor was measured after different time intervals, finally observing a strong increase after 380 h.

To avoid amorphous carbon damping, and the potential ion-induced degradation of the properties of the device layer, Ovartchaiyapong et al. used a diamond on insulator substrate to fabricate single crystal cantilever resonators [163]. Thin (~20 μm) diamond plate were bonded to a oxidized wafer with oxide-oxide bonding, and the diamond layer was then thinned down to few micrometers with Ar/Cl$_2$ based RIE/ICP. More conventional lithography and wet etching were employed to pattern and release the diamond cantilevers. Mechanical quality factors of 338 000 at room temperature were recorded for cantilevers oscillating at ~1 MHz. Analysis of the dissipation mechanisms shows quality factors limited by the clamping losses and surface dissipation, as well as viscous damping at higher pressures. The authors report a minimum of Q_m at 50 K, potentially related to surface imperfection or internal friction peaks.

A similar method was employed by Tao et al. for the fabrication of single crystal cantilevers. Here two approaches are proposed: HSQ bonding of the diamond plate to a silicon substrate (similarly to the previous example), and embedding the diamond plate in a quartz "sandwich" [170]. The diamond plate is then thinned down to ~100 nm before patterning the cantilevers. Compared to single crystal silicon and PCD control cantilevers, the SCD devices offer 1-2 order of magnitude better Q_m, measuring up to 1 510 000 at 3 K (~400 000 at room temperature) [51]. Material quality is as well important, since devices fabricated in electronic grade SCD show Q_m of 1 order of magnitude higher. The authors highlight the potential of SCD cantilevers for applications in ultasensitive force measurements. Further developments [171] show force noise level of 0.19 aN at 100 mK. Such high sensitivity was achieved thanks to the small mechanical dissipation of the "nanoladder" cantilever design. The noise level is small enough to enable the detection of the weak signals produced by single nuclear or electronic spins in magnetic resonance force microscopy.

In both cases [163, 170], RIE/ICP based thinning produced non-uniform thickness of the resulting diamond layer, evident by looking at the color gradient of the diamond film on the microscope images. This non-uniformity can be caused both by the starting (non-uniform)

plate thickness or by the plasma dynamics within the RIE/ICP chamber. For mechanical oscillators the thickness variation may not be a problem, but of course it will broaden the frequency spread of the devices. Moreover, most of the diamond substrate is etched during fabrication, making this approach not entirely economically sound. It must be noted that, depending on the fabrication process and the starting SCD plate, the cost of the diamond material "lost" during thinning may not be a limiting factor.

Another fabrication strategy is based on the modification of the plasma direction to obtain an "angled-etching", either with a Faraday cage [172, 173], or by tilting and rotating the sample [174], to create freestanding structures in bulk substrates. SCD cantilever with quality factors up to ~94 000 are achieved [164]. Burek et al. report compressive stress in clamped-clamped cantilevers, which is surprising given that the structure are fabricated in a bulk substrate. The authors presume that it originates from the mask during etching. For applications with color centers, it is important to know precisely the strain environment since it will modify the emission characteristics. Dynamical actuation of these diamond resonators is of course possible by including some form of actuator. Following up on previous work, Sohn et al. included dielectrophoretic actuation on the angled-cut SCD cantilever beams [175]. Metal electrodes are deposited on the side of the cantilevers, and actuation occurs when a RF signal sent trough the metal is resonant with the diamond structure. Compared to other forms of actuation, like electrostatic or piezo-electric, this method does not require the deposition of a thin film on the diamond resonator, therefore it does not modify the mechanical damping characteristic of the device. The main trade-off of this actuation method is the very weak resulting effect for the same actuation voltage compared to the other methods.

3.2.1 Diamond optomechanics

Given the broad transparency range, suspended optical cavities can be fabricated in diamond. Several examples have been reported in literature using several fabrication techniques including focused ion beam milling [176, 177], angled-etching [173], "quasi-isotropic" etching [178–180], as well as more "traditional" techniques using NCD [181, 182]. Of course, the ability to suspend optical cavities paves the way to diamond cavity optomechanics.

Including an appropriately designed "optomechanical crystal" in a angled-etched diamond cantilever, Burek et al. [29] demonstrated phonon lasing and OMIT. The devices present high optical quality factors Q_o (1.7×10^5 and 2.7×10^5) and high $\Omega/2\pi$ (5.5 GHz and 9.5 GHz), making the optomechanical cavity operate in the sideband resolved regime. Measured mechanical quality factors (at room conditions) are of the order of ~5000. Q_m of diamond resonators tend to increase at lower temperatures [51], and a following work [185] shows that it is the case for these diamond optomechanical crystals, recoding an increase of 30× at 5 K, measuring Q_m up to 238 000. Thanks also to the high oscillating frequency, the devices have Qf-products in the order of 10^{15} Hz at 5 K (10^{13} Hz at 300 K; see figure 3.4 for a comparison).

Other demonstrations of optomechanical interaction in diamond structures were reported by
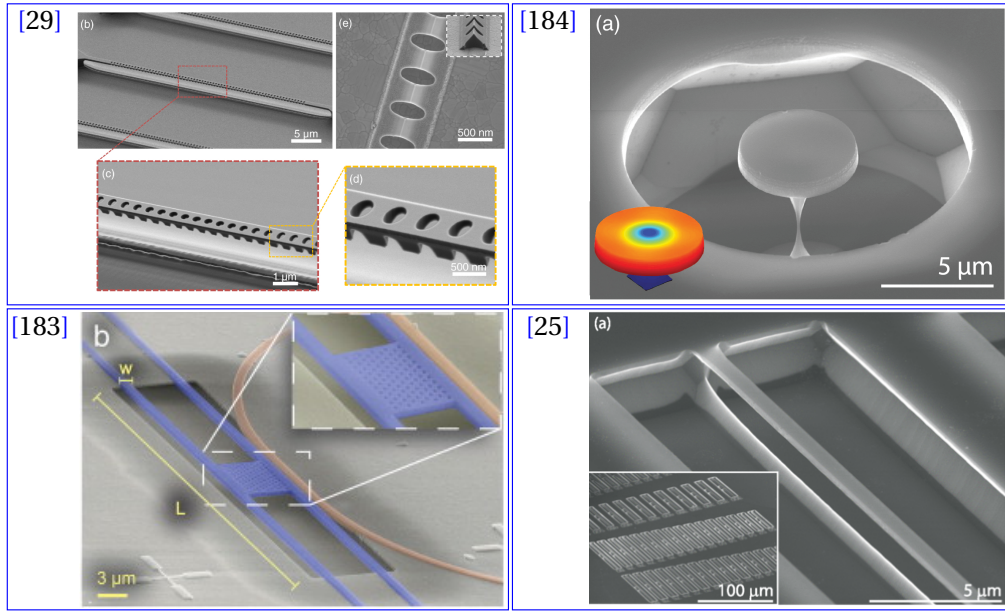
Figure 3.3 – Examples of optomechanical resonators in single crystal and polycrystal diamond. [29] Photonic crystal beam fabricated with the "angled etching" technique. [183] Polycrystalline H shaped resonator. [25, 184] Single crystal nanobeam and single crystal microdisk fabricated in a bulk substrate using a "quasi-isotropic" undercut.

the group of Wolfram H. P. Pernice using a polycrystalline diamond film. Although mechanical, thermal and optical properties are inferior to SCD, PCD offers the great advantage of deposition on different substrate and the ability to process it with more "conventional" fabrication techniques, as previously mentioned. Raith et al. [186] reported optomechanical excitation of PCD nanobeams. Suspended slot waveguides with gaps between 150 nm and 300 nm are fabricated in the diamond film. Mechanically, the waveguide will act as two coupled nanobeams, and the in plane expansion mode will modify the propagation of the optical mode. In this configuration, a strong interaction between the mechanical mode and the optical field is possible because most of the power propagating through a slot waveguide is situated in between the two nanobeams, creating a strong field gradient. Propagation losses are rather high, and they are dominated by scattering losses due to the rough surface of the polycrystalline film ($\sim$15 nm RMS). The authors state that losses can be improved using a polishing step, but they are not critical in the current structures due to the short length of the waveguides. To readout the modulation of the propagation due to the mechanical oscillation, the slot waveguides are included in a Mach-Zehnder interferometer. Light is coupled in and out of the chip via grating couplers. Q_m of 11 200 are measured at 3.8 MHz in vacuum. As expected, the diamond film had residual internal stress depending on the growth condition. At high pump modulation amplitudes, both sings of the Duffing nonlinearity are reported, depending on the device location on the chip, indicating that the internal stress is not uniform. By changing the design of the mechanical resonator, higher Q_m of 28 000 was achieved [183]. The slot waveguide was replaced by an "H" shaped mechanical resonator coupled to a bus

waveguide. The center of the mechanical resonator was patterned with a photonic crystal with a band gap at the operating wavelength (~1550 nm) to confine the light next to the waveguide and enhance the optomechanical interaction. The authors report a displacement sensitivity of 14 fm/$\sqrt{\text{Hz}}$. A set of gold electrodes deposited on the H resonator arm opposite to the bus waveguide can be used to drive the mechanical oscillation [187]. This allows the optomechanical detection of higher order modes, up to 115 MHz. The electrodes operate as an electrostatic actuators: a DC signal generates an attractive force that will increase the separation between the H resonator and the bus waveguide, while a RF signal can be used to excite the mechanical oscillation. Q_m is reported to decrease with the increase of the oscillation frequency, measuring ~1300 at 115 MHz. Compared to previous work [183], the mechanical dissipation increases due to the additional damping caused by the deposited gold electrodes. As for the optomechanically driven oscillation, higher amplitude of the RF signal highlights Duffing nonlinearity of the resonator.

Similarly to [183, 186], Khanaliloo et al. [25] demonstrated a single crystal diamond optome-chanical system that allowed to excite the self-oscillation of diamond nanobeam waveguides. The structures are etched in bulk CVD optical grade diamond exploiting the etch rate de-pendence of diamond crystal planes to release rectangular beams. The technique will be described in detail in section 6.1, since it is the same that will be used to create our micro-disk and micro-rings. The system presented by Khanaliloo et al. is based on the modulation of the optical supermode guided by a tapered waveguide positioned in proximity of the oscillating diamond nanobeam. Stress-enhanced photothermal force and optomechanical coupling are responsible for the self modulation. The high Q_m of 7.2×10^5 measured at 5 K (~1.5×10^5 in high vacuum at room temperature), contributes to a low self-oscillation threshold of ~100 nW. Contrary to an optomechanical crystal or a wispering gallery mode resonator, the system presented here is inherently broadband given the absence of an optical cavity. Moreover the cantilever design allows for large self-oscillation amplitudes (>200 nm), although the low oscillation frequency (~1 MHz) put the system in the unresolved sideband regime. Nonlinear mechanical behavior is highlighted by the large oscillation amplitudes. The authors show that nonlinear dynamical softening is present and it can be tuned by the separation taper-nanobeam, and it is influenced by internal stress of the diamond structure. The dynamical oscillation of the device and the ability to tune the internal stress with optomechanical back-action, make this structures an intresting system for optomechanical controls of spins, like the nitrogen vacancy center. Further work [188], explored another way of inducing optome-chanical back-action to the diamond nanobeam. The tapered fiber is used as a displacement sensor by keeping the input fiber sufficiently low to prevent any modification of the nanobeam motion. The tuning of the optomechanical back-action occurs by focusing a fixed wavelength pump at different positions compared to the nanobeam via a microscope objective, somewhat similar to optical tweezers. The sign of the back-action, i. e. amplification or cooling, depends on the microscope focal spot position, in contrast to cavity optomechanics, where the sign of the back-action does not depend on the pump coupling. When the focal spot is above the nanobeam plane, the self-oscillation is amplified, and vice versa when the focal spot is below

the nanobeam plane. Since the back-action is dominated by the photothermal effect, a thin layer of titanium is used to enhance the effect. Self-oscillation amplitudes achieved in this configuration are comparable to the one previously reported [25], confirming the potential to drive spin transition in nitrogen vacancies using the microscope controlled photothermal optomechanics.

The group of Paul E. Barclay at the University of Calgary demonstrated several optomechanical effects not only with the nanobeam waveguides, but also using SCD microdisks for cavity optomechanics experiments. The fabrication strategy used is based on the same quasi isotropic etch [178], here yielding microdisks supported by an hourglass shaped pedestal with octagonal cross section. Self-oscillation amplification was demonstrated in SCD microdisks with sufficiently thin pedestal diameters. Mechanical resonances corresponding to the fundamental radial breathing mode are reported with $\Omega/2\pi$ ~2 GHz and Q_m ~ 9000 (at room temperature and pressure), yielding an Qf-product of 1.9×10^{13} Hz. The pedestal geometry appears to be of particular importance for the RBM dissipation, and only the thinnest pedestals (~100 nm) present small mechanical dissipation, Γ, indicating that the RBM is limited by clamping losses. The microdisks show high ambient condition optomechanical cooperativity $C = Ng_0^2/\kappa\Gamma \simeq 2.7$. The measured self-oscillation amplitudes are of the order of ~30 pm. Compared to the nanobeams, the amplitude is significantly smaller, however, given the nature of the oscillation mode, the induced internal stress is high enough to produce comparable coupling between the mechanical field and the spin of a nitrogen vacancy center. The threshold power of the self-oscillation is in the order of few mW, and it is related to the optical quality factor of the cavity. Further work by the authors investigated fabrication strategy to improve the sidewall surface roughness, improving the optical quality factor to ~300 000, as well a way of reducing the mechanical dissipation by engineering the pedestal shape [189].

With the engineered pedestal, demonstration of optomechanical cooling and OMIT was possible [192]. These effects are achievable by red detuning the laser pump compared to the optical cavity, and it would not be possible when a thermo-optic instability occurs without employing cavity stabilization techniques [184]. Given the small pedestal dimensions, the thermal conductivity of diamond is reduced due to surface and size effects. By including an additional step in the fabrication, the authors modified the pedestal shape to achieve better thermal conductivity while maintaining the same mechanical dissipation. Compared to previous work, this yielded a thermal time constant (τ_{th}) of one order of magnitude faster, enabling access to the red side of the optical resonance. Excellent OMIT performance was reported even with Q_o ~ 10^5. OMIT can be further exploited using a second control laser signal to achieve all optical switching [193], optical control of pulse time storage storage[194], and optomechanically mediated wavelength conversion [195, 196]. By introducing a second control field, it is possible to transfer information between two optical modes coherently using the optomechanical interaction. The authors propose these diamond microdisk as a platform to convert red light emitted from diamond color centers to telecom wavelengths for long range transmission.
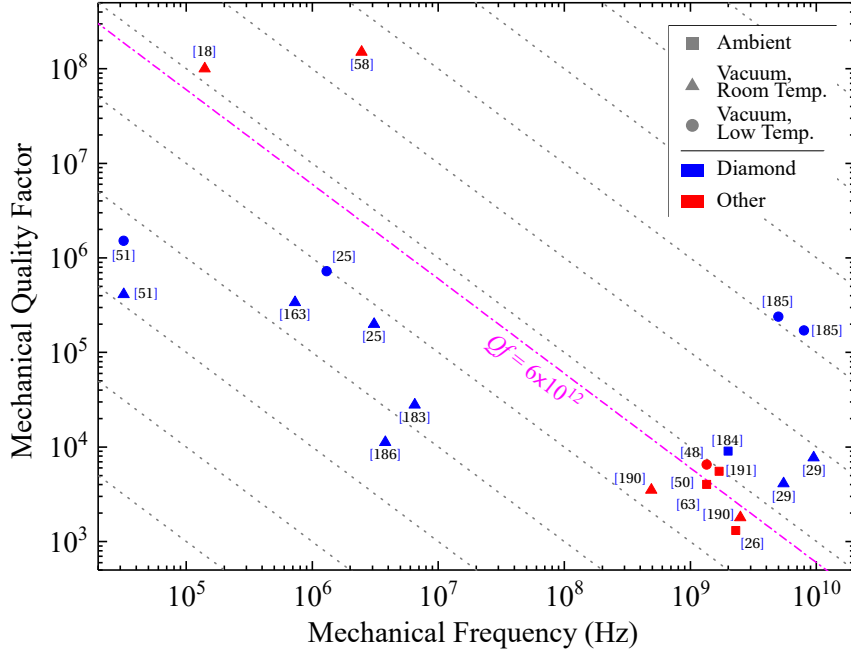
Figure 3.4 – *Qf*-product plot of the reported examples of diamond mechanical and op-
tomechanical resonators (blue) compared to other high *Qf* systems (red). The squares in-
dicate experimental values obtained at room temperature and pressure, the triangles in
vacuum at room temperature, and the circles in vacuum at cryogenic temperature. The ma-
genta dot-dash line shows the *Qf*-product required for room temperature optomechanics
$Q_m f_m = k_B T / \hbar \simeq 6 \times 10^{12}$, and the gray dot-dot lines indicate constant *Qf*-product products
every order of magnitude.

Figure 3.4 shows the *Qf*-product of the examples of the diamond mechanical and optome-
chanical oscillators presented previously, compared to some high *Qf* demonstrations in other
material platform. Diamond resonators can offer high mechanical quality factors, well in the
>100 000 range, and appropriate geometries that yield high oscillation frequencies allow for
high *Qf* above the 6×10^{12} Hz threshold for room temperature operation. The high *Qf* values
indicate that diamond mechanical and optomechanical resonators are a great platform to
realize an optomechanical frequency references. Among the different techniques presented
in this chapter, the "angled-etching" and the "quasi-isotropic undercut" are the fabrication
strategies that offer the highest *Qf* values and are better suited to realize a mechanical or
optomechanical resonator to date. Both have different strengths and drawbacks, however
the latter can be more flexible with regards to resonator geometries that can be realized. In
fact, other than the cantilever and microdisk presented previously, 1D [197] and 2D [180]
photonic crystal structures have been demonstrated. Although no optomechanical interaction
was reported, with appropriate cavity design it would be possible to excite the interaction.
Alternatively, the creation of a thin diamond layer with implantation is also a valid approach,
provided that the amorphous layer is appropriately removed to prevent mechanical losses.

This can be achieved with extensive annealing, as mentioned previously, or by etching the layer after bonding to a scaffold [198] or to a sacrificial layer.

Extensive work has been done to integrate color centers into mechanical and optomechanical oscillators. Given the atomic nature of the color centers, they act as a localized sensors, therefore are well suited to investigate particular phenomena[199]. Ovartchaiyapong et al. [200], for example, proposed to use NV centers to analyze clamping losses in mechanical resonators to develop low dissipation designs. Color centers integrated in a mechanical resonators can have similar interactions as the optical and mechanical field in an optomechanical resonator, allowing for cooling and amplification of the mechanical motion [134]. As for the optomechanical system, a cooperativity and a coupling strength can be defined, which benefit from low mechanical damping and small size [201]. High cooperativity spin-mechanical system are a fundamental building block of quantum networks. The mechanical field can be used both to manipulate [155, 202, 203] and to propagate the quantum information encoded in the color center [154]. The benefit of using a mechanical oscillation compared to a magnetic field is that the former can be easily confined and guided by realizing nanostructured devices. Furthermore, optomechanical systems can be used to drive the mechanical oscillation at the characteristic GHz frequencies, and can be more efficient than other actuation schemes.

To conclude, diamond is an attractive platform for multiple applications. Here I highlighted the capacity of realizing low dissipation mechanical and optomechanical resonators, which paves the way to applications demonstrated in other material system such as sensing, timing, and accelerometry, and to others more inherent to diamond, thanks to the ability to host well localized quantum systems, which makes the diamond platform a great candidate to realize quantum communication and quantum processing.

4 Simulations and methods

In this section I will describe how the simulations were performed, analyze the results, and present the final designs that were implemented in micro-fabrication. Most of the simulations were based on a finite element method (FEM) software, COMSOL Multiphysics. The method works by dividing the geometry in elements and by solving the relevant partial differential equations, expressed in the weak form, only at the nodes of the elements. The method is very powerful because it allows to solve the problem for complex arbitrary geometries when an analytic solution may not be available. In the previous chapter I gave some analytic expression for the solutions of a WGM cavity (equation 2.9 in section 2.1), and in this chapter I will compare it to the results of numerical simulations, analyzing the case where azimuthal symmetry is broken. FEM simulations, moreover, allow to obtain an estimate of the radiative losses of the optical modes. Similar analysis will be performed for the mechanical resonances. In analogy to the optical simulations, it is possible to estimate some of the mechanical losses contributions.

For each model, optimization of the element discretization (meshing) and of the boundary condition will be performed. The results in numerical simulations is strongly influenced by meshing and boundary conditions. However, ultimate precision is not required given the uncertainty of the real geometric dimensions achievable with fabrication and the uncertainty on the material properties used to define the material in the simulation. An error below 10% should be a reasonable expectation.

To understand the effect of some fabrication steps, ion implantation in the single crystal diamond substrate will be simulated. Stopping and Range of Ions in Matter is the software package used for the Monte Carlo simulations [204]. Finally, the last section of this chapter will describe the characterization setups.
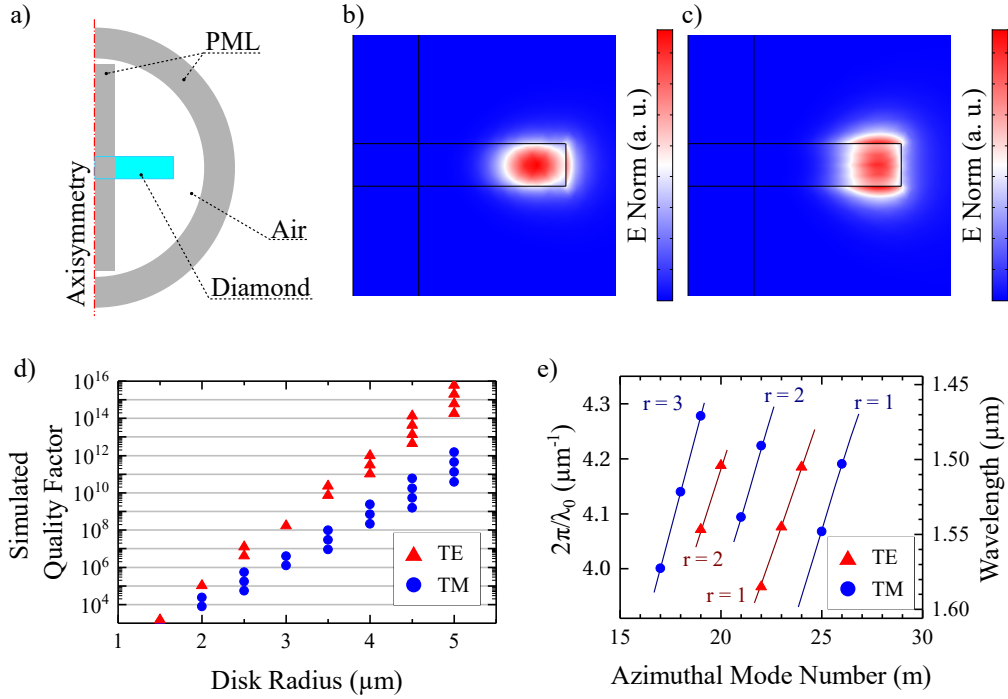
Figure 4.1 – a) Scheme of the geometry implemented in COMSOL to simulate the optical resonances of a diamond micro-disk. The simulation uses a 2D axisymmetric geometry to reduce the computation time. To at the edge of the air sphere a perfectly matched layer is used. Similarly, a cylindrical PML is used to remove some numerical results that do not correspond to real modes. b) Electric field norm plot of a TE mode ($TE_{1,17}$) of a micro-disk with radius 2.5 μm, thickness 500 nm. c) Electric field norm plot of a TM mode ($TM_{1,15}$) of the same micro-disk. d) $Q_{o,rad}^{sim}$ of first order radial TM and TE modes for different micro-disk diameters. Only the resonances within the tuning range of the tunable laser (1460-1580 nm) are reported. As expected, $Q_{o,rad}^{sim}$ is decreasing with the disk radius. e) Dispersion of resonances in a disk with radius 5 μm, thickness 500 nm. The lines group the points with the same radial mode number.

4.1 Optical simulations of Whispering Gallery Mode resonators

The initial simulation of the whispering gallery optical modes was done using a 2D axisymmetric geometry, and a scheme of the simulation geometry is shown in figure 4.1.a. The *Electromagnetic Waves - Frequency Domain* physics module was used to calculate the optical eigenmodes of the WGM cavities. Compared to solid mechanics physics, optical simulations generally require much higher computational resources, and since we can exploit the azimuthal symmetry of such devices, the axial symmetry allows to greatly reduce the computing requirements. This is mainly due to the small element required to resolve the optical wavelength in the infrared (~1 μm).

The simulation geometry is composed of different domains, representing the microdisk/microring and the air cladding. The cladding is necessary because part of the mode is guided

outside the cavity. The dimensions of this cladding is important since it needs to be sufficiently large to include the evanescent tail of the optical mode. Figure 4.1(a) shows the 2D axisymmetric simulation geometry. The air cladding is modelled as a semicircle (corresponding to a sphere due to the symmetry used) around the resonator. At the air sphere boundaries a perfectly matched layer is used to asses the radiative losses. A PML is an artificial material that does not reflect any incoming radiation and it attenuates the propagation within the material. A scattering boundary condition can be used instead of the PML. While it is less computationally intensive since it is modelled as a boundary and not a 3D domain, it reflects part of the radiation that is not normal to the surface. A first order scattering boundary condition is can be expressed as $\mathbf{n} \cdot \nabla E_\perp + i k_0 E_\perp = 0$, where $E_\perp$ is the electric field normal to the propagation direction. It is evident that efficient scattering ($E_\perp = 0$) only occurs for normal incidence. It is possible to use higher orders of the scattering boundary conditions to extend the range of incidence angles, however it still performs worse than a PML. In any case, it is appropriate to design the cladding so that the radiation is mostly normal to the boundary as reflections occur even for the PML at grazing incidence angles. Spheres or cylinders are the most appropriate shapes for microdisks and microrings. Using the scattering boundary conditions yields a difference of $< 5\%$ compared to the results with PML. For the 2D simulation we can afford to use a PML and keep the simulation size under control, while the scattering boundary condition will be used for the 3D simulations. The optical modes are the calculated using an *Eigenfrequency* study step. The solutions are restricted to the range of the tunable laser that will be used for the characterization (1460-1580 nm) and only the solutions with radiation limited quality factor, $Q_{o,rad}^{sim}$, above 1000 are accepted. The solver can return a number of numerical solutions that are guided in the air cladding that clearly do not represents real modes. These solutions have a large imaginary part (low $Q_{o,rad}^{sim}$), and it is easy to filter them out. Including a cylindrical PML around the symmetry axis of the model help removing a large number of numerical solutions corresponding to non real modes. These solutions have electric field concentrated around the axis and may have $Q_{o,rad}^{sim}$ above the selected 1000 lower limit. The geometry shown in figure 4.1(a) includes this PML as well.

Figure 4.1(b) and (c) shows the mode profile of the fundamental TE and TM cavity modes. The cavity modes are identified as TE or TM and three indices corresponding to the radial, vertical, and azimuthal mode numbers (r, z, and m). For a thickness of ~ 500 nm only one vertical mode is supported ($z = 1$), therefore often only the two remaining indices are used to classify the optical mode. At around 700 nm multiple vertical modes are supported. Looking at the electric field norm, the $TE_{1,m}$ is guided mostly at the outer surface of the microdisk/microring. It will be very sensitive to sidewall roughness, which is created by the lithography and vertical etch steps in the fabrication. $TM_{1,m}$ is guided at the top and bottom surfaces, therefore it will be sensitive to imperfections caused by the surface polishing and the release step. The simulations do no take into account the scattering caused by roughness and imperfections on the cavity surface. Figure 4.1(d) shows the $Q_{o,rad}^{sim}$ dependence on the cavity radius. larger cavities confine better the optical mode, indicated by the exponential increase of the quality factor. For a thickness of 500 nm, radii bigger than 2.5 µm yield $Q_{o,rad}^{sim} > 10^6$.
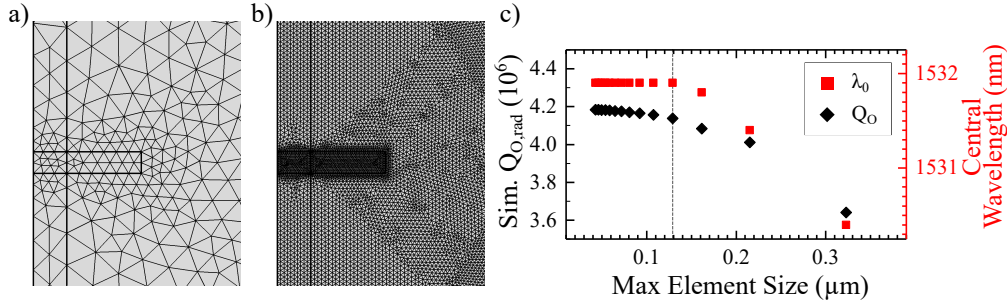
Figure 4.2 – Meshing using $\lambda_n/2$ (a) and $\lambda_n/15$ (b). c) Variation of the simulated central frequency and optical quality factor of the $TE_{1,17}$ mode of a micro-disk (2.5 μm radius, 500 nm thickness). When the mesh elements are smaller than $\lambda_n/5$, the change of the simulated value becomes negligible, approaching a mesh convergence regime.

Figure 4.1(e) shows the mode dispersion. As described in section 2.1, good mode matching occurs when $m \simeq \beta_{wg} r_d$. For the diamond cavities, the external waveguide is a tapered fiber. The propagation of the fiber β_{wg} can be estimated with a 2D *Mode Analysis* simulation of the fiber cross section, since $\beta_f = 2\pi n_{eff,f}/\lambda_0$. Using the refractive index of a SMF-28e tele-com fiber, the effective index of the guided fundamental mode in the tapered fiber is around 1.2 when the diameter is below 1 μm, corresponding to $\beta_f \simeq 4.8 \, \mu m^{-1}$ at $\lambda_0 =$ 1550 nm, and $m_{opt} \simeq 24$. Optimal phase matching occurs for microdisks with $r_d \simeq$ 3.5 μm and $th_d \simeq$ 500 nm. Smaller disks will be better matched to thinner fibers (as $n_{eff,f}$ will approach 1 when the diameter decreases) while bigger disks require thicker fibers (however the tapered fiber becomes multimode at ~1.2 μm diameter).

Meshing and boundary conditions can have a large influence on the accuracy of the results. The simulation results presented above are calculated with the optimized mesh and boundary condition. A mesh convergence study was performed: the (maximum) element dimension was swept from $\lambda_n/2$ to $\lambda_n/15$, where λ_n is the wavelength in the material, and the change in central wavelength, λ_c, and $Q_{o,rad}^{sim}$ were monitored. Since we are interested in optical resonances at ~1550 nm, the latter will be used as the reference vacuum wavelength. In figure 4.2(c) the mesh convergence results are shown. After reaching an element dimension of $\lambda_n/5$, the simulation starts to enter a mesh convergence regime, meaning that the variation of the results starts to be small enough (<1%) that the error caused by the mesh is negligible compared to errors coming from other sources, such as discrepancy between the simulated geometry and the actual fabricated devices, and the material model used for the simulation. For the final simulation, $\lambda_n/5$ was used.

Similarly, the dimension of the air sphere and of the PML was also swept. Ideally, the boundaries of the simulation volume should be sufficiently far from the optical resonance to avoid reflections and other numerical artifacts. Of course, the size should still be kept as small as possible to keep the simulation time and size under control. The radius of the air sphere was swept from r_d + 5 μm to r_d + 15 μm, where r_d is the disk radius. The PML thickness was swept
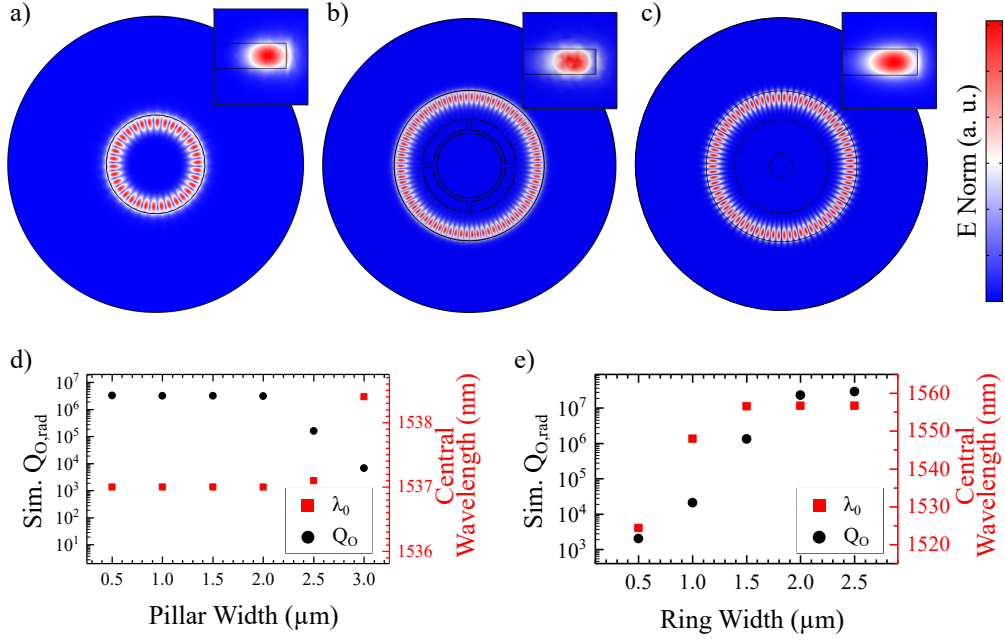
Figure 4.3 – 3D COMSOL eigenmode simulation of a diamond micro-disk (radius 2.5 μm, thickness 500 nm) showing the $TE_{1,17}$ mode (a), and of a micro-ring (radius 5.25 μm, thickness 500 nm , ring width 25 μm) showing the $TE_{1,39}$ mode. c) 2D axisymmetric simulation of a micro-ring, with the same dimensions of (b), showing the same $TE_{1,39}$ mode. The 3D solution was extracted by multiplying the 2D results by $e^{-im\phi}$. The insets show the mode cross section for the respective simulations. For all images, color gradient represents the electric field norm. Change of λ_0 and $Q_{o,rad}^{sim}$ for a disk with different square section pillar width (d) and for a ring with different ring width (e).

from 0.5 μm to 5 μm. The results show that there is little variation (<5% for Q-factor, <1% for central wavelength) with regards to the air sphere radius within the range chosen. A similar behavior is found for the PML thickness sweep, where the variation is negligible (<1% for the Q-factor, <0.1% for the central wavelength) for layer thickness bigger than 0.8 μm, i. e. when it becomes of the same order of the optical wavelength. For the optimized geometry, an air sphere of radius r_d+10 μm with a 1.5 μm PML was used.

For microdisks and microrings oscillating in the RBM, g_{mb} depends only on the optical field (equation 2.22). Typical values are estimated in the range of 10 to 100 GHz/nm, which are comparable to what is reported in literature.

In comparison, a 3D optical eigenfrequency simulation is much more computationally intensive. For comparable simulation volumes and meshing, the required memory is well beyond 100 GB for a 3D simulation, compared to the ~2 GB required by the axisymmetric model. However, a fully 3D simulation is required when the azimuthal symmetry is broken. In fact, both fabrication method described in chapters 5 and 6 would yield non cylindrical support pillars that may reduce $Q_{o,rad}^{sim}$. Therefore it is useful to put effort (and patience) into

simulating a realistic geometry, including the fabrication constraints, to better understand the source of losses. For the 3D simulations, similar geometry was used: the air cladding is a cylinder with radius r_d+5 µm and thickness th_d+5 µm, where th_d is the device thickness. A scattering boundary condition is used at the air cylinder boundaries instead of a PML to reduce the memory requirement. To fit the simulation within the available memory, the maximum element size was set at $\lambda_n/3.5$. In figure 4.3 the results of the 3D simulation are reported. For micro-disks, the results seem to be in good agreement between the 3D and the 2D axisymmetric models, with both λ_c and $Q_{o,rad}^{sim}$ within 1% of difference.

When a square section support pillar is included in the simulation, $Q_{o,rad}^{sim}$ starts to degrade (figure 4.3(d)). Breaking the cylindrical symmetry has a significant influence on the simulation results when the pillar starts to be big compared to the disk radius. To ensure that no degradation occurs, the difference between the disk radius and half the pillar section diagonal should be bigger than ~1.25 µm, assuming a disk thickness of 500 nm (for thinner disks, the requirement should increase since the optical mode would be more elongated along the radial direction). For thin support pillars, the simulated values approach the results of the 2D axysimmetric simulation. Same requirement on the pillar diagonal apply for other polygonal sections, such as octagonal sections that may be the result of a crystallographic etch (section 6.1). Similarly for micro-rings, quality factors are significantly different beween the 2D and 3D models due to the inclusion of the supports in the 3D models. In figure 4.3(e), $Q_{o,rad}^{sim}$ is plotted versus the ring width, w_r. When the latter increases, the quality factor approaches the results of the 2D ring model. The doublet splitting is visible in the 3D simulations of the microrings (and the microdisk with large square pillar) due to the breaking of the azimuthal symmetry.

Silicon resonators

The silicon resonators in the MORPHIC platform behave similarly to the diamond cavities. Since the external coupling waveguide is fabricated in the silicon layer, phase matching and coupling in general is easier. The gap between the resonator and the waveguide is defined by the lithography, therefore several iterations with increasing separations from 130 nm to 300 nm are included in the mask. Given the thickness of the silicon layer (214 nm) and the geometry of the grating couplers used to couple light in and out of the silicon chip, the microresonators support only TE modes.

4.2   Mechanical simulations

Mechanical simulations follow a similar structure. It is possible to use a 2D axisymmetric geometry, however, it is not necessary because it is possible to easily fit a full 3D simulations within the memory of a modern personal computer. Moreover, since one of the main purpose of these simulations is to minimize the clamping losses, it is important to model accurately the resonator support, which will not have cylindrical symmetry with the fabrication methods chosen. The *Solid Mechanics* physics module with the *Eigenfrequency* study step were used.

A perfectly matched layer is included at the boundary of the substrate to estimate the clamping losses. As for the optical simulations, the thickness of the PML and the portion of substrate including in the simulations influence the accuracy of the results. Ideally, the substrate and the PML should be at least of the same dimension of the acoustic wavelength, which can be estimated from the acoustic velocity and the resonance frequency of the structure. If we assume that the oscillation propagates into the substrate from a single point corresponding to the support pillar, the substrate and the PML should have spherical symmetry to optimize the accuracy of the boundary condition with regards to unwanted reflections. Given the typical resonance frequencies of µm-sized microdisks and microrings and the high acoustic velocity in diamond, typical acoustic wavelenghts are of the order of few tens of µm. Looking at the acoustic velocity, v_s, in table 3.1, we can estimate the acoustic wavelength to be $\lambda_{mech} = 2\pi v_s/\Omega \simeq 20\,\mu m$ in single crystal diamond and $\lambda_{mech} \simeq 10\,\mu m$ in single crystal silicon, for a resonance frequency of 1 GHz. The optimization procedure of substrate and PML size, and mesh size is the same as the optical simulations case. The solution converge to the same value when the substrate size and PML approaches the size of λ_{mech}. In the final simulations, the size was chosen accordingly to the resonance of interest, achieving good accuracy and avoiding excessive memory use. On the other hand, the approximation of $\lambda/5$ used for the mesh size in the optical simulations is not applicable here due to the large acoustic wavelength. Instead, the mesh was defined in a way to have at least two elements in the narrow sections of the geometry. Refining the mesh further did not produce significant error reduction.

The material model used does influence greatly the results. It is important to assign the correct stiffness matrix and use an anisotropic model both for single crystal diamond [97] and single crystal silicon [99]. Using an isotropic model can induce substantial error in the central frequency, since it would overestimate the overall stiffness of the structure, as the stiffness in the ⟨100⟩ directions can be significantly smaller than the one in the other directions. Finally, it is necessary to decide whether or not to include geometric nonlinearities in the calculations. When large deformation occurs, the small strain approximation used in the finite element solver is not accurate anymore. Including nonlinear response does increase the accuracy of the simulation, but it increases the computation time as well.

Diamond microdisk oscillators

Microdisks with radii of few µm are capable of supporting radial breathing mode (RBM) oscillations at GHz frequencies [48, 50, 184, 191]. Figure 4.4(c) shows the dependency of the RBM frequency versus the radius of a diamond microdisk. When the radius is smaller than $\sim 5\,\mu m$ the structure oscillates in the GHz regime. Given the exponential dependency, $\Omega/2\pi$ increases rapidly for smaller disks. A lower limit is however imposed by the optical radiative losses, since the simulated quality factor starts dropping below 1×10^6 for radii smaller than $2\,\mu m$. This gives a limit on the maximum frequency exploitable in single crystal diamond microdisks. For some applications [83], it may be necessary to operate at higher frequency; in that case, the higher orders oscillation modes (or another geometries like a photonic crystal
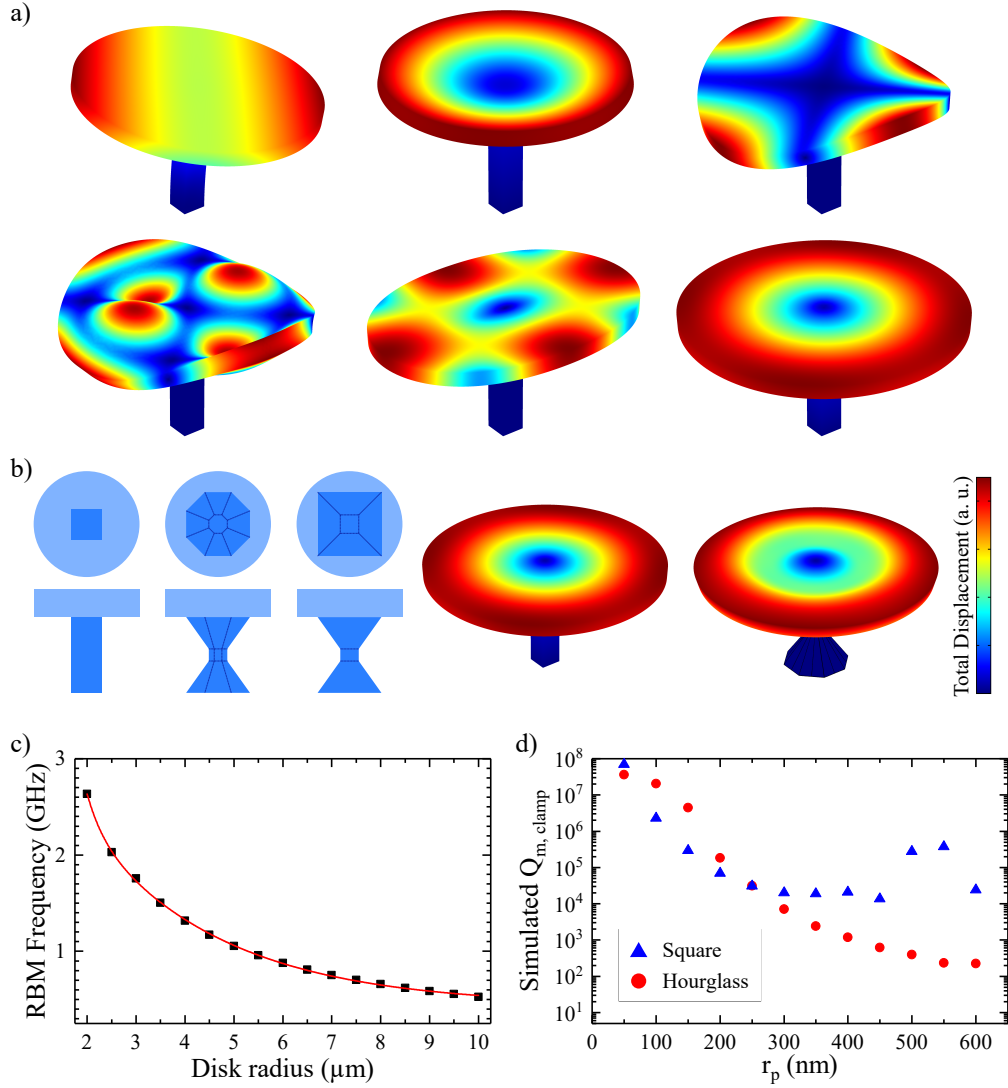
Figure 4.4 – a) Mechanical oscillation modes of a diamond microdisk. The modes are arranged left to right following the mechanical oscillation frequency. Different shapes of pedestal may modify the order. The mode with the highest optomechanical interaction is the radial breathing mode (RBM); its shape for non cylindrical support pillar is shown in sub-figure (b). c) Change of the RBM frequency versus the microdisk radius (with cylindrical pillar of radius 250 nm). The black squares represent the results taken from a COMSOL simulation, while the red curve is a decaying exponential fit. d) $Q_{m,clamp}^{sim}$ versus pedestal size both for a square section pillar (blue triangles) and octagonal section hourglass pillar (red circles). The pedestal size (r_p) is the incircle radius of the (narrowest) pillar section. The size of the disk is fixed (radius 2.5 μm, thickness 300 nm)
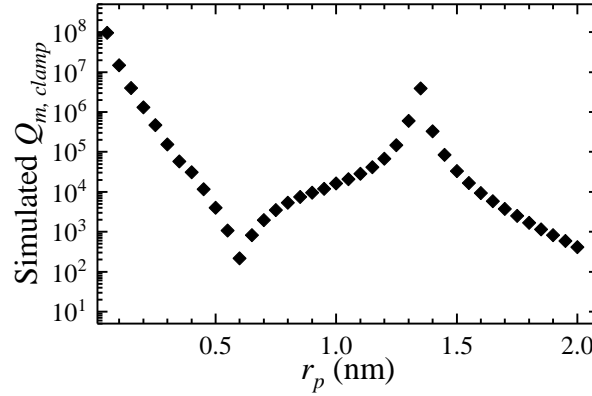
Figure 4.5 – Change of the simulated clamping loss limited quality factor of a $10\,\mu$m silicon disk with the radius of the support.

beam [29]) can be used. The thickness does not influence much the oscillation frequency of the RBM ($\sim 1\%$ from $100\,$nm to $500\,$nm).

Changing the pedestal size does influence the oscillation frequency. A structure with a bigger pedestal will be stiffer than a structure with a smaller pedestal. However, it is better to control the oscillation frequency with the radius of the disk, since the pedestal should be as small as possible to minimize the clamping losses (equation 2.12). Using the fabrication method described in chapters 5 and 6 may yield a pedestal with different shapes (figure 4.4(b))[1]. A square section pillar does not change substantially the mechanical modes shape or central frequency compared to a cylindrical pillar of comparable size. It does however influence the splitting of some modes due to the anisotropy both in the material model and on the structure: the splitting is measurable in the out of plane contour modes also in structures with cylindrical pillar, and the relative frequency difference can be influenced by the orientation of the square pillar. The RBM is not split by anisotropy unless the square pillar is particularly big. The hourglass pillar shape does modify the mechanical spectrum, pushing the out of plane contour modes at higher frequency. RBM is still supported, but tends to be at higher frequency compared to the cylindrical and square pillar. Including a PML to calculate the the clamping losses, shows that the size of the pedestal is critical (figure 4.4(d)). The clamping losses of the hourglass design appear to increase substantially more than the square pillar design when the pillar becomes wider. In the graph, there is a local Q_m maximum at around $550\,$nm. The position of this maximum depends on the microdisk dimensions. Similar simulation results can be found in literature [205], and are consistent with the prediction of equation 2.12.

Figure 4.6 – a) Lithography mask design of a microring with concentric support. b) RBM shape extracted from COMSOL relative to the 400 MHz design. c) RBM shape extracted from COMSOL relative to the 1 GHz design.
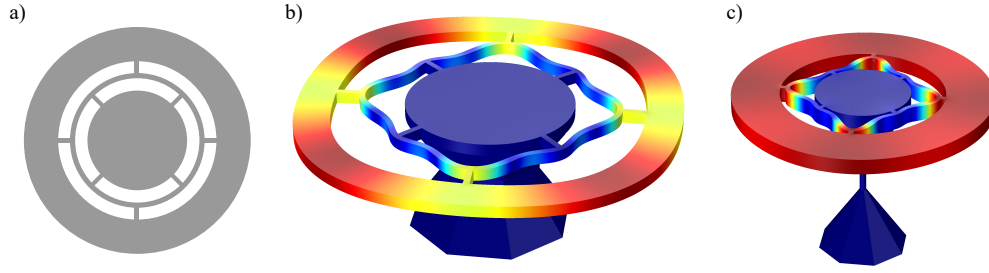
Silicon oscillators

The silicon oscillators included in the first fabrication run were two microdisks with radius 10 μm and 20 μm and two microrings with the same external radius. Due to the undercut process and the geometry of the rings central support, only the 10 μm disks were supported with a sufficiently small pillar (see chapter 7). The modes shape is similar to the diamond disks shown in figure 4.4(a), with the first order RMB oscillating at 254 MHz. The pillar shape that can be achieved with the fabrication process has cylindrical symmetry, thus the clamping losses behave similarly to the diamond disks with square section support pillar, with the losses rapidly increasing with the support pillar dimension and a local maximum for supports with radius of ~1.35 μm. Figure 4.5 shows the change in simulated quality factor relative to the clamping losses with the pillar size.

4.2.1 Concentric microring design

The advantage of a microring desing is to engineer the clamping to the substrate in the same lithography layer, instead or relying on a precisely timed release or more complex pedestal engineering [48] to minimize the clamping losses. The tradeoff is that the structure is overall more compliant, therefore the first order RBM will be at lower frequency.

The microrings were integrated in the lithography mask for the crystallographic undercut process (chapter 6). The process places some restriction on the parameter space available. In particular, the central support needs to be much wider than the ring width to have a suspended structure with a smooth bottom surface. For the particular case of the crystallographic undercut producing the hourglass shaped pillar, the central support diameter needs to be around 7 μm to suspend correctly a 1.5 μm wide ring. Therefore the common design of the ring supported by linear tethers would need to be particularly large, yielding a low frequency

---

[1]A precise description of the shape of the support pillar can be found in the respective chapters, where the fabrication process will be described.

RBM, or would require long etching times if paired with a second lithographically defined protection layer [22]. The first order RBM frequency depends inversely with the external radius of the microring. To keep the frequency in close to the GHz regime, a microring design with concentric supports was developed (figure 4.6(a)). The design allows to compact the radial dimension of the support tethers and to have a large central support, while maintaining the RMB frequency high. Several designs were implemented in the single crystal diamond microfabrication, with expected RMB frequency ranging from 400 MHz to 1 GHz. In figure 4.6(b-c) the mode shape for the two extreme design is shown.

The design is very robust with regards to fabrication imperfections. Oscillation frequency and clamping losses are not influenced by the width of the tethers, length of the undercut, or uneven undercut of the tethers. The width of the ring was chosen to be 1.5 µm to avoid scattering of the optical mode due to the tethers attachment, following the optical simulations. The width of the tethers was set at 250 nm to have a comfortable lithography requirements, but variation of several hundreds of nm do not affect the mechanical mode. The gap between the concentric tethers, the support, and the ring was changed to select the target RBM frequency. For the smallest design (higher frequency), the gap was designed at 150 nm in order to get filled completely during the sidewall protection step (see section 6.1.4) in order to have a smaller central support, and to enforce the undercut from the outer edge of the microring. The designs implemented show simulated $Q_{m,clamp}$ above 10^7 reliably, even with tethers with uneven thickness and for a any width of the central support pillar. A similar design was included in the next fabrication run of the MORPHIC platform, with a target frequency of 250 MHz.

4.3 Monte Carlo simulations of ion implantations and damage

The fabrication described in the next chapters use accelerated ions in some of the fabrication steps. In particular, the focused ion beam undercut uses 30 kV Ga^+ ions to mill the diamond (chapter 5 and the polishing step is performed with low acceleration (<1 kV) Ar ions (chapter 6). To assess the implantation of these ions in the diamond lattice we used Stopping and Range of Ions in Matter (SRIM) [204], a free software package designed to calculate the statistics of ion implantation in solids. To obtain a reliable simulation results, the diamond is defined with three parameter indicating the lattice displacement energy, the lattice binding energy, and the surfave binding energy. We defined the first two energy as 52 eV and 6 eV respectively [167], the latter was left at the default 7.41 eV.

Figure 4.7(a) shows the implantation and damage of 30 kV Ga^+ ions in a single crystal diamond substrate. Gallium is a common ion source used in focused ion beam. The simulations estimate the depth of the damage layer caused by the ion beam. In the figure, two configuration are shown: normal and grazing incidence. From the depth profile, we can expect the damage to extend up to 25 nm when the ion beam is normal to the top surface (e. g. at the bottom of a FIB milled trench) and up to 10 nm when the ion beam is grazing the diamond surface (e. g. on
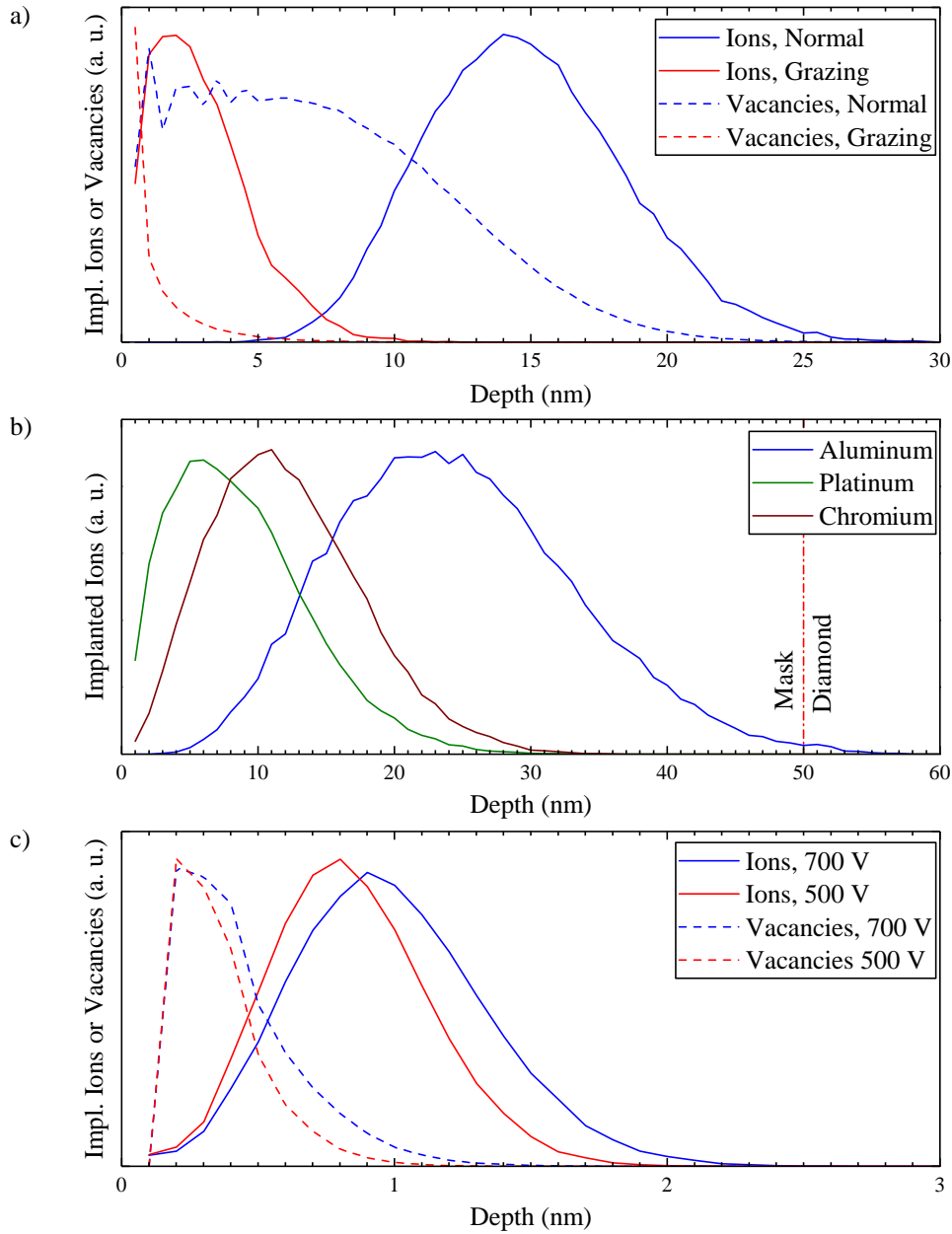
Figure 4.7 – SRIM simulations of ion implantation. The top 2 graphs (a, b) are related to the fabrication method based on focused ion beam milling described in chapter 5. a) Implantation of 30 kV Ga$^+$ ions in single crystal diamond at normal incidence (0 °) and grazing incidence (89.9 °), and density of lattice vacancies created by the two configurations. b) Implantation of 30 kV Ga$^+$ ions in a single crystal diamond substrate protected by different 50 nm thick masking metal layers. c) Implantation and density of vacancies in single crystal diamond for Ar$^+$ ions at different acceleration voltages and 50 ° incidence. This graph is relevant for the ion beam etching based surface polishing described in section 6.1.1, where low acceleration Ar$^+$ ions are used to remove the polishing defects of the as-received single crystal diamond plates.

the sidewalls of a FIB milled trench). To prevent excessive damage to the substrate, a masking layer can be used during FIB milling. Commonly, FIB tools are equipped for in situ deposition of platinum. Alternatively, metal layers can be deposited with sputtering or evaporation before milling. Figure 4.7(b) shows the implantation profile of $30\,kV$ Ga^+ ions at normal incidence in a diamond substrate protected by $50\,nm$ thick masking metal layers. Heavier elements, such as platinum and chromium, perform better than lighter ones at stopping the incoming ions, requiring only $\sim 30\,nm$ to stop the implantation successfully. Finally, a fabrication technique that will be employed for smoothing the diamond surface is ion beam etching (IBE). Figure 4.7(c) reports the implantation and damage of the low acceleration Ar ions. The profile reveals that only the top $2\,nm$ of the single crystal diamond substrate is affected by the ion damage.

4.4 Characterization methods

In this section the characterization methods will be described. The fabricated structures were tested to observe the optical and mechanical behavior of the optomechanical cavity, as well as the photoluminescence from color centers in the diamond structures.

4.4.1 Optical transmission spectra

The first measurement that was performed was the characterization of the optical cavity. Figure 4.8 shows a scheme of the setup. For the diamond resonators, no waveguide was integrated on the chip, therefore an extenal waveguide was aligned to the proximity of the device. A tunable laser (Agilent 81682A) is coupled to a single mode optical fiber (SMF28). The light polarization is controlled by a fiber polarization controller. The FPC (Thorlabs FPC562) is composed by three plates containing coiled optical fibers and it utilizes stress-induced birifrangence to change the polarization in of the guided optical mode. The signal is coupled to a tapered fiber which is evanescently coupled to the optical cavity. A 6-axis stage (Thorlabs MAX603D/M) is used to control the separation and the orientation of the tapered fiber compared to the device. The alignment is monitored with a microscope equipped with a $20\times$ long working distance objective. The transmitted signal is collected by a power meter (Agilent 81536A).

The tapered fibers were fabricated with the setup of the Laboratory of Photonics and Quantum Measurements, EPFL. Their setup uses two step motors to tension the optical fiber and a hydrogen flame to heat to the glass temperature. The plastic buffer surrounding the fiber is removed to reveal the glass cladding. The flame position and the draw speed of the motors are adjusted to obtain a smooth and slow variation of the fiber diameter, until the central part is about $1\,\mu m$ wide. During the pulling, the transmission through the fiber is monitored. The starting fiber is single mode at telecom wavelengths (1550 nm), and it transitions first to multimode and then again to single mode as the diameter decreases. In the transmission spectrum, the guiding conditions are represented by the presesnce of oscillation of the transmitted power vs time (or draw length). When the oscillations stop, the fiber reached again single
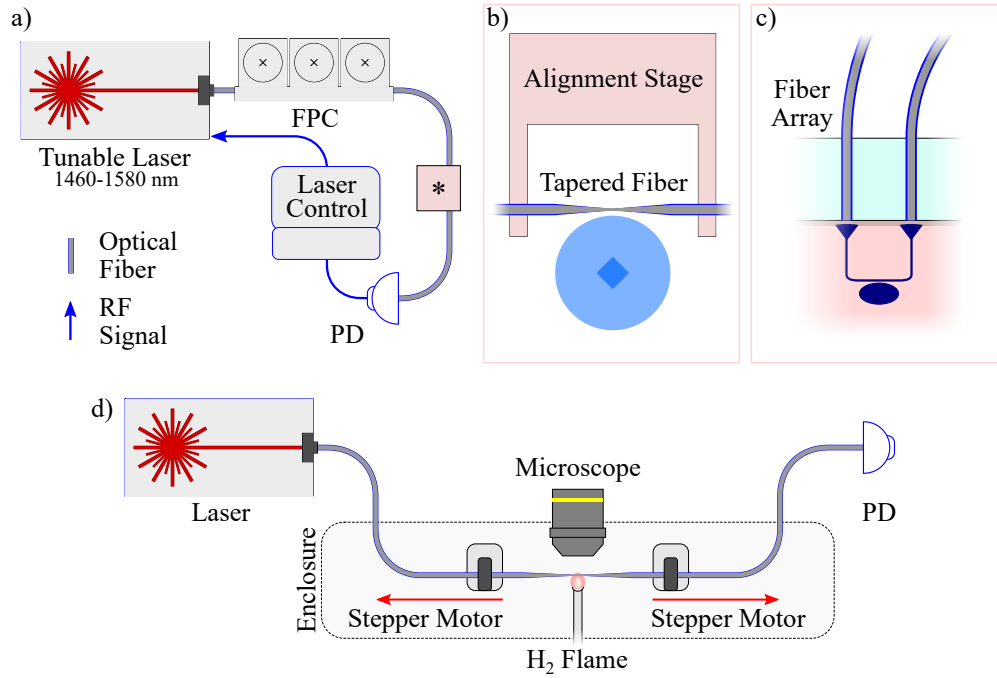
Figure 4.8 – a) Optical transmission measurement setup. A tunable laser (Agilent 81682A) is coupled to an optical fiber. A fiber polarization controller (FPC, Thorlabs FPC562) is used to set the polarization of the laser signal. The transmission from the device under test (DUT, *) is collected by a photodetector (PD, Agilent 81536A power meter). The DUT is either a diamond or a silicon resonator. For the former (b), a tapered fiber is used to couple the laser signal to the resonator. A 6-axis (Thorlabs Nanomax MAX603D/M) is used to position the fiber within few micrometers from the device. For the silicon resonators (c), a fiber array is aligned to grating couplers. The signal is guided to the silicon resonator via a suspended silicon waveguide. c) Scheme of the fiber tapering setup. Two stepper motors pull the fiber apart while a hydrogen flame heats it. The process is monitored by a microscope and by measuring the transmission through the fiber.

mode guiding condition and the desired diameter. The process yields a smooth variation of the fiber diameter, which allow for high transmissions through the fiber (> 90%). The tapering setup scheme is shown in figure 4.8(d). Once the fiber is tapered, it is secured to an aluminum holder using UV glue in order to be mounted to the 6-axis stage. A red laser is used during the alignment procedure to easily detect when the fiber is touching the substrate or the resonator. The laser used is rather broad and multimode, therefore it is easy to see when the fiber is in coupling range as the resonator "lights up" and it is easily visible under the microscope. The fiber is connected to the telecom tunable laser and the final alignment is performed by controlling the fiber position by the closed loop piezoelectric (1 nm theoretical resolution) drives integrated into the 6-axis stage and by monitoring the transmission spectrum to achieve critical coupling.

The silicon resonators are fabricated in a platform that allows single mode waveguides in
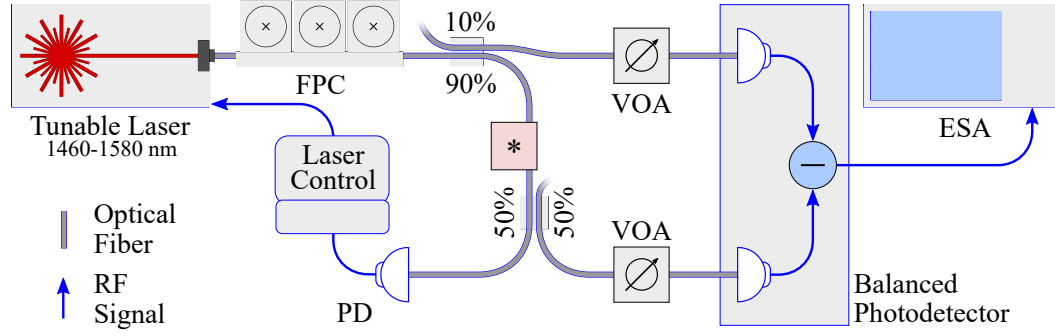
Figure 4.9 – Optomechanical characterization setup. The light from a tunable laser (Agilent 81682A) is coupled to an optical fiber, and the polarization is controlled with a fiber polarization controller (FPC). A 90 : 10 fiber coupler is used to divide the signal in two paths: the upper path will be collected in one detector of the balanced amplified photodetector (Thorlabs PDB480C-AC) after being attenuated accordingly with a variable optical attenuator (VOA); the lower path will go through the device and will get split again with a 50 : 50 fiber coupler. Part of the signal will be collected by a photodetector (left PD, Agilent 81536A power meter) to analyze the DC part of the transmission spectrum and complete the laser feedback loop. The other portion of the signal will be collected by the second port of the amplified balanced photodetector to complete the homodyne detection scheme. The signal from the balanced detector is analyzed by an electronic spectrum analyzer (ESA, Agilent N9320A).

the device layer. Grating couplers designed to operate in the C-band are patterned in the silicon device layer with a precise spacing, in order to be coupled to an array of polarization maintaining single mode fibers. Given the design of the grating, only one polarization (TE) is transmitted. The gap between the waveguide and the silicon cavity is defined by the lithography. Multiple variation of the gap are included on the chip (ranging from 150 nm to 280 nm). Since only one polarization is transmitted, only the TE-like modes will be measured in the transmission spectrum. The coupling between the fiber array and the gratings is controlled by a 6-axis stage. The angular alignment is particularly critical, since it will influence the transmission window of the couplers. In both cases the measurements are performed at ambient temperature and pressure. A Matlab script controls the laser wavelength and power and it extracts the data from the power meter. The stored transmission spectrum is then fitted by a Lorentzian (or multiple Lorentzian when doublet splitting is visible) to extract the quality factor and the central wavelength of the resonance.

4.4.2 Optical transmission in the frequency domain

The mechanical oscillation of a microresonator can be observed in the noise spectrum of the optical transmission. Since the structures analyzed here have multiple oscillation modes at distinct (high) frequencies, it is easier to visualize the transmission modulation in the frequency spectrum using a fast photodetector and an electronic spectrum analyzer. The mechanical resonance will appear as Lorentzian peaks in the ESA [61]. However, given the

typical oscillation amplitudes and the corresponding modulation depth, amplification in the optical or electrical domain is often required. To summarize, to characterize the mechanical oscillation a tunable laser is coupled to the DUT, and the transmitted signal is collected by a high speed photodetector and analyzed by an ESA. The frequency and power of the tunable laser is controlled to achieve optimal detuning and to reach the threshold power, according to equation 2.26 and **??**. The measurement setup can be further optimized by using a separate detector to monitor the DC component of the optical transmission, enabling a form of feedback loop to detune the laser frequency by the optimal amount from the central cavity frequency. Cavity stabilization techiques can be also included in the measurement setup to deal with thermooptics shifts of the cavity resonance. In our case, no stabilization technique was employed as it is not necessary to observe parametric amplification. The scheme of the setup used is shown in figure 4.9.

To filter out other noise sources, an homodyne detection scheme can be used. The transmission spectrum is collected at one port of a balanced photodetector, while part of the laser signal, unmodified by the DUT, is collected at the other port. The output signal is a difference between the two and any noise not originated by the DUT is removed from the frequency spectrum. For good balancing it is important that the two signals have the same power level and delay. To set the power, variable optical attenuators are used before the balanced photodetector. To control the delay, in our setup we used fibers with the same length in both arms of the detection schemes. The solution is not optimal but allowed for sufficient extinction of the noise. Future refinement of the setup should include other ways to control the delay, i. e. including a fiber stretcher in one arm [206], or splitting the signal after the DUT with a polarization beam splitter and setting the polarization before the DUT so that only part of the signal is coupled to the resonator [4]. Of these two techniques, the first is more suitable since it works even when only one polarization can be transmitted through the DUT, like for the case of the silicon devices.

4.4.3   Laser Doppler Vibrometry

Another way of measuring the mechanical oscillation of a microresonator is to analyze the frequency shift induced on a reflected laser field by the Doppler effect. The technique is commonly used in the analysis of MEMS behavior and reliability, and it can also be used to detect the Brownian motion of mechanical resonator. The main challenge of the latter is the sensitivity of the instrument required to detect the very small displacement amplitudes of Brownian oscillations, commonly in the picometer range [207]. The devices were analyzed with a Polytech UHF-120 laser Doppler vibrometer, using an 100× Mitutoyo long working distance objective to achieve good spacial resolution and a small laser spot size. Measurements were performed both in air and in vacuum. Due to the orientation of the setup, only the out of plane modes can be measured. The scheme of the measurement system is shown in figure 4.10.
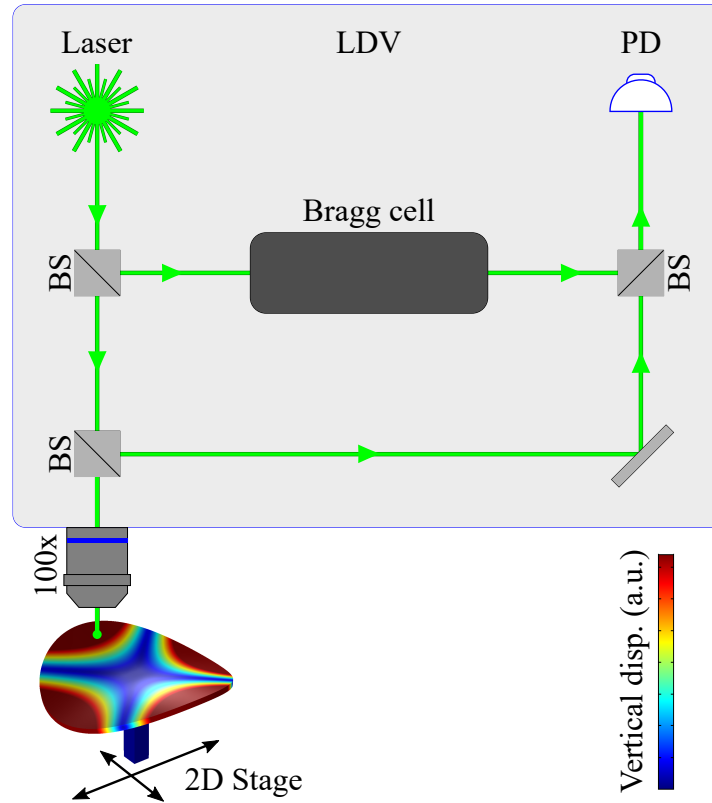
Figure 4.10 – Scheme of a laser Doppler vibrometer (LDV). A green laser is focused on the DUT and scanned across the surface thanks to a 2D stage. The mechanical oscillation of the DUT induces a Doppler shift in the laser field. The frequency shift is detected from the interference of the signal reflected by the DUT with a reference arm. The frequency of the reference arm is swept by a Bragg cell across the bandwidth of the measurement. The signal collected by the photodetector is post-processed to obtain a frequency spectrum of the velocity or of the displacement of the DUT.

4.4.4 Confocal Raman spectroscopy and photoluminescence

A μ-photoluminescence (μPL) measurement was used to characterize the emission from the diamond resonators. While we did not purposely implant defects or used substrates grown specifically for the scope, nitrogen vacancy centers are very common on CVD optical grade substrates. Moreover, other it can be used to detect the formation of defect from the microfabrication. Since the luminescence emission will be enhanced by the optical cavity, it can be a way to extract the optical quality factor at visible (red) wavelength. Using a tapered fiber start to be challenging at shorter wavelengths due to the smaller extension of the modes outside the waveguide and due to the requirement of a smaller waveguide cross section. Raman spectroscopy on the other hand, can give an indication of the quality of the crystal, since single crystal diamond has a very sharp and bright Raman peak. Any *sp2* carbon will produce a rather noticeable broad peak in the spectrum.
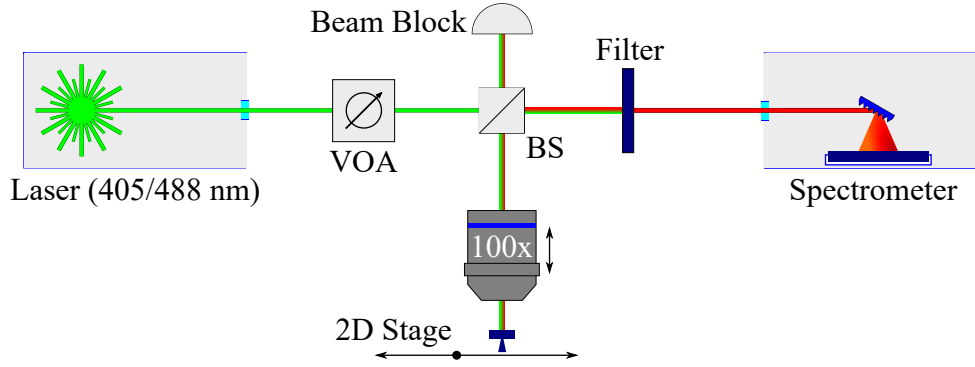
Figure 4.11 – µPL measurement scheme. A green laser (405 nm or 488 nm) is focused on the microresonator with a 100× high NA objective. The luminescence signal is collected with the same objective and it is directed towards the spectrometer with a beam splitter (BS). The fourth arm coming out of the BS is directed towards a beam block. A wavelength filter attenuates the green laser from the beam directed to the spectrometer, leaving the red luminescence unaltered. Inside the spectrometer, a diffraction grating disperse the luminescence signal on the CCD detector. Different gratings can be used to achieve different wavelength resolution and bandwidth.

For the measurement, a confocal Ramanscope (Renishaw inVia), from the EPFL IPHYS Material Characterization Platform, as well as a custom built setup, at the EPFL Advanced Semiconductors for Photonics and Electronics laboratory, were used. Both equipment can be schematized in figure 4.11. A green laser (405 or 488 nm) was used to excite the luminescence. The laser light is coupled to a high magnification long working distance microscope objective. The objective is aligned at different points on the resonator surface and focused at different planes to better optimize the collection from the optical mode radiation. The collected light is filtered to reduce the reflected laser component and analyzed by a spectrometer. By chosing the appropriate dispersion grating and angle, we can set the resolution and wavelength range, respectively, of the CCD. While the Ramanscope offers an integrated solution with multiple grating and laser to choose from, and it can detect near-IR signal, the custom photoluminescence setup offered more flexibility to mount the sample and a better wavelength resolution, but its spectrometer was optimized to detect UV-blue light rather than red-IR. The radiation pattern of microdisk is oriented mostly in the plane of the disk, therefore the signal to noise ratio will be small, and a high NA objective is required to detect the resonance signal.

5 Single crystal diamond microdisk resonators by multi-directonal Focused Ion Beam Milling

The results reported in this chapter are based on the workreported in: Graziosi, T., Mi, S., Kiss, M. & Quack, N. "Single crystal diamond micro-disk resonators by focused ion beam milling". *APL Photonics* **3**, 126101 (2018) [208]. The fabrication method exploits the freedom offered by a Focused Ion Beam to create 3D structures. The FIB is a versatile tool capable of mask-less localized etching of any sample. Traditionally is used for metrology and the preparation of transmission electron microscope lamellas [209, 210], but it can be employed to create 3D structures [211] thanks to the ability to rotate the sample with respect to the ion beam. While it is a very versatile technique, it cannot be scaled easily as other methods. However, this may not be a limitation in a research settings, where the process is not standardized and can result in low yields. On the contrary, it can be used to locally correct mistakes coming from other sources, like a previous lithography step.

Given that SCD has a high chemical resistance, FIB pattering has been a viable fabrication approach. Photonic crystal structures fabricated with FIB milling have been demonstrated [177, 212, 213], starting from thinned diamond slabs or heteroepitaxial membranes. Full 3D patterning with FIB was as well reported, but low quality factor optical resonances or no optical resonance were detected [176, 214]. Two main issues are associated with FIB milling of diamond: the first is the roughening and the rounding of the features, the second is the implantation of the focused ions (generally gallium) in the diamond matrix.

In this chapter I will describe the process in detail, including the proposed solutions to the before-mentioned problems. Then I will report the characterization results, as well as identifying potential future improvements.
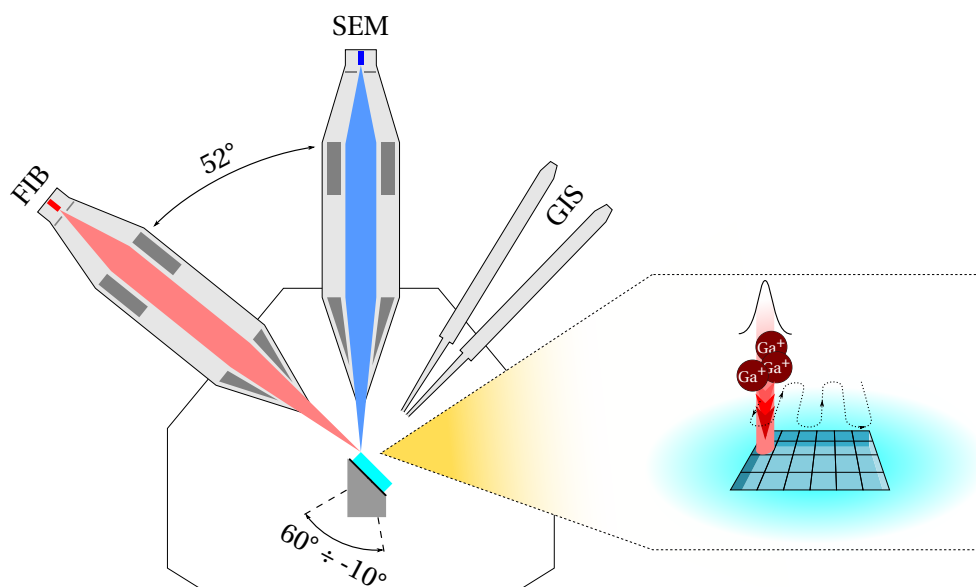
Figure 5.1 – Scheme of a dualbeam SEM/FIB. Electron and ion columns are installed at a precise angle (52°) to allow for sample imaging and milling. A Gas Insertion System (GIS) is installed in the FEI Nova 600 used, enabling selective etching and localized deposition. The sample is mounted on a 5-axis stage, and for the resonator fabrication we used a 45° sample holder. The inset shows a scheme of the patterning system. The pattern is automatically divided in pixels and the ion (or electron) beam is scanned following the desired overlap and dwell time parameters. The focused ion beam has a Gaussian profile, therefore there will be residual irradiation outside of the pattern area.

5.1   Focused Ion Beam milling

The fabrication strategy employed was based on Focused Ion Beam (FIB) milling to sculpt the resonator shape. A scheme of the tool is in figure 5.1. Liquid gallium is a common ion source, and the one installed in the FEI Nova 600 Nanolab at CMi. Other sources, such as oxygen, helium, or xenon [215–217] can be used , yielding less ion damage of the sample or adding a chemical component to the etching (compared to the physical sputtering caused by the Ga^+). Additionally, a FIB can be equipped with a gas injection system (GIS). The FEI Nova 600 has four GIS modules installed, capable of inserting different gasses in the chamber to assist with the etching (H_2O, selective carbon mill, and XeF_2, insulator selective) or to deposit (TEOS and Pt). In this configuration, the Ga^+ ions are responsible of activating the precursor molecules in gas phase.

Initially, we tested the etch characteristics of the Ga^+ ions, with and without chemical assistance (with H_2O and XeF_2). No substantial difference in diamond etch rate was found. The Ga^+ only etching produced a noticeable redeposited layer adjacent to the milling pattern area. The same happened with the chemically assisted etching, but less redeposition was detected for similar etched volume, which can be explained by the increased chemical component in

1 μm
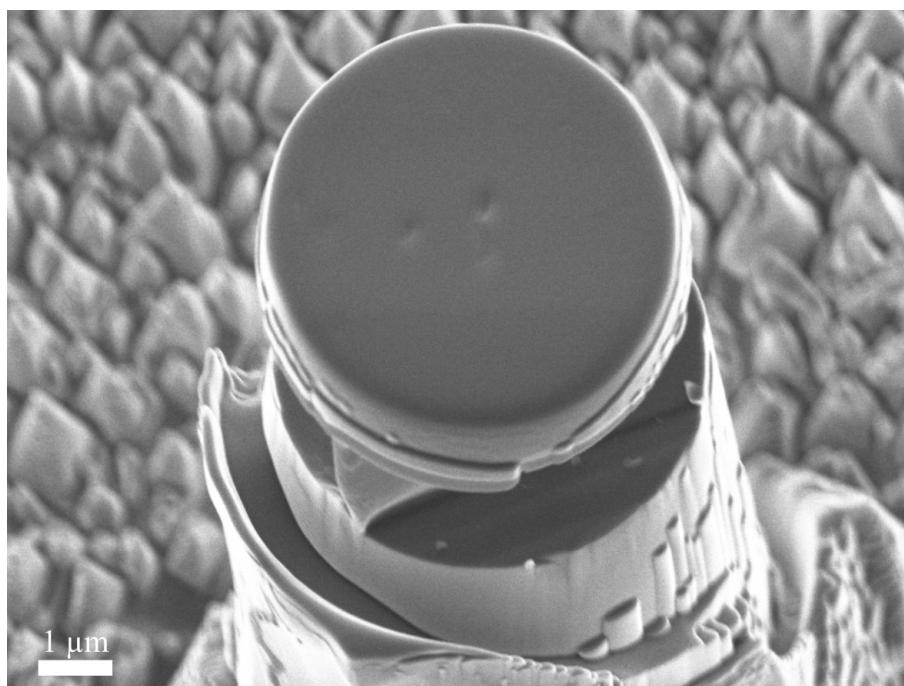
Figure 5.2 – SEM recording of a microdisk after FIB milling. Rounding induced by the Gaussian profile is evident in the top edge and steps and ripples caused by ion irratiation at shallow incidence are visible on the sidewalls. The sample was processed without depositing a protective metal layer starting from a diamond pillar etched with oxygen plasma DRIE.

the milling. However, the use of the GIS slowed down the milling time severely since it was necessary to retract and redeploy the GIS needle for every stage movement. Moreover, with the sample mounted on a 45° holder and with the ion beam aligned to the sample top surface, the needle could impact the holder or the diamond chip. For this two reasons I decided to not use any GIS assisted etching. In all configurations, the Gaussian profile of the ion beam caused a visible rounding of the features top edges [214], as shown in Figure 5.2. Depositing an additional layer is an efficient solution to achieve sharper features: in TEM lamellas preparation is recommended to deposit Pt, generally using GIS, before starting milling. The additional layer is also used to prevent excessive Ga^+ implantation. The metal layers (Pt, Al, and Cr) are effective in stopping the implantation, and the use of any of them would prevent FIB-induced damage in the structure volume that does not need to be exposed to the ion beam. While Pt can be deposited directly in-situ via GIS, it is difficult to remove after the fabrication. Cr and Al are both easily stripped with acids (Cr7 Chromium Etch and ANP Aluminum Etch) and are preferable over Pt. Cr shows better selectivity towards the Ga^+ ions, making it a better mask, but it has poor adhesion to diamond when sputtered, therefore a Cr mask layer with a Al adhesion layer will be used during FIB milling.

The ion beam can be programmed with different scanning routines, dwell times and pixel overlaps. To achieve a smooth sidewall surface, using a "progressive line scan" routine is preferable to the raster scan, in combination to the protective metal layers. The line scan

works by scanning the beam in a line until the desired etch depth is reached for that line and then moving to the next. In the FIB software it is possible to define a the desired milling as time or target depth, which is calibrated for different materials. When choosing the desired program and inputting the etch depth, the software sets time, dwell time and overlap appropriately. I routinely used the silicon program which yields $\sim$ 70% of the defined target depth when used with a diamond substrate. The raster scan instead does a single pass on one line, according to the dwell time and overlap settings, before moving to the next; it repeats the pattern until the target etch depth is reached. Dwell time and pixel overlap do not appear to influence the sidewall quality, only the milling rate. When the diamond is not protected by the metal layer or a raster scan is used, steps and ripples can be formed on the sidewall. This phenomena is well documented in literature [218–220], and can be observe not only with FIB milling but also during ion beam etching at high incidence angles. The theory behind ion sputtering is complex and not completely understood [221], however some techniques are routinely used and produce reliable surface qualities. The fabrication scheme employed here resembles the TEM lamella fabrications, where line scan is used during the final thinning to produce a smooth surface. In our case we found that using a masking material, low ion current and a progressive line scan pattern (instead of a standard raster scan) prevented the formation of roughness on the milled volume sidewalls.

5.2   Microfabrication

An overview of the fabrication is shown in figure 5.3. The micro-disks were fabricated starting from a CVD single crystal plate (3 mm × 3 mm × 0.15 mm, LakeDiamond), with the surface polished down to a roughness of ~1 nm RMS. We decided to etch pillars in the diamond substrate, which will be FIB milled to create the micro-disks, to reduce FIB milling time and to isolate the structures from the surrounding enough to confine the optical mode and to leave space for the tapered fiber alignment. Several masking materials were tested to be used as hard mask. We obtained good results with sputtered SiO_2, sputtered Al, and sputtered Si when tested against a high power high bias oxygen plasma. The material with the highest selectivity was Al_2O_3 deposited with Atomic Layer Deposition (ALD). Alumina however is difficult to pattern and required a thicker photoresist layer to transfer the pattern with ICP-RIE, therefore the next best material was used. We deposited a 500 nm layer of sputtered SiO_2 (Pfeiffer SPIDER 600). The substrate was positioned inside a recess of a silicon carrier wafer, to have the SiO_2 top surface aligned to the silicon wafer. We coated the sample with AZ ECI 3007 positive photoresist using a ACS200 Gen3 automatic coater/developer spinning at 5800 rpm with 100 °C soft bake for 90 s. The recess in the silicon wafer yielded a uniform and thin (~0.6 μm) with minimal edge beads. The photoresit was exposed using mask photolithography. Given the small dimensions of the diamond chip, the resist layer resulting from spin coating is generally non uniform , and thicker compared to spinning on a wafer or bigger die with the same settings. Edge beads are an increase in the PR thickness due to the presence of an edge. Automatic coaters like the one we used can remove easily the edge beads on a wafer by
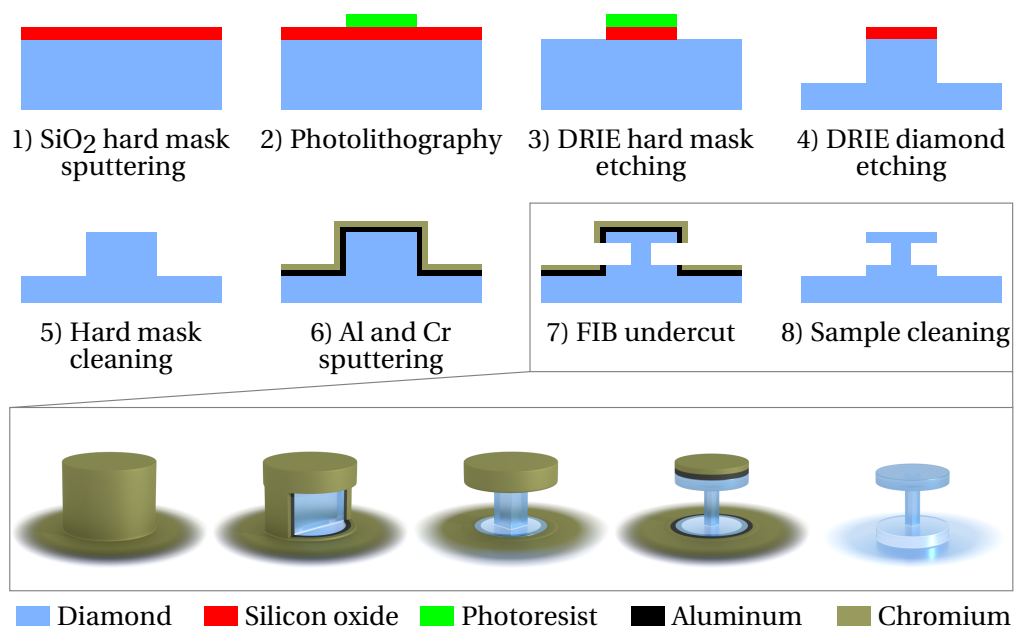
Figure 5.3 – Final process flow for the multi-directional milling approach. The diamond die is attached to a carrier wafer for processing in the CMI tools. 1) sputtering of a SiO_2 hard mask (500 nm). 2-3) photolitography and DRIE etching of the hard mask. 4) DRIE etching of the diamond with a vertical recipe (SPTS 1, see table 5.1) to transfer the design. The sample is then prepared for FIB processing, by stripping the hard mask (5) and by sputtering aluminum and chromium (6). The inset shows the milling procedure (7) in details. 8) Finally, the sample is cleaned with wet enchants and oxygen plasma to remove the metal layers and the redeposited Ga/C layer and annealed to etch the FIB-induced damage layer (8). The inset shows the details of the FIB undercut protocol.

dissolving the PR at the edges with solvent, but this is more difficult to do with a small chip. Edge beads can reduce drastically the yield and the resolution of the photolithography step when using a standard chromium mask: the layer is thicker at the edges and gets gradually thinner in the center, resulting in a non-uniform illumination dose required to correctly expose the whole chip; additionally, the thicker edges prevent the mask to be in contact with the center of the chip, decreasing the resolution. Spray coating can be an alternative approach, but we found that the resulting layer was too thick, reducing the lithography resolution as well. Spinning the AZ ECI 3007 at high speed with the diamond chip in the silicon pocket produced the best results with acceptable loss of yield and resolution due to the smaller edge beads. Unfortunately, gluing the diamond chip inside the silicon pocket is not the ultimate solution to the problem. Detaching the chip at the end of the processing is not always easy and of course it requires more fabrication steps, which include lithography and etching of the silicon wafer with precise control of the etch depth to match the diamond chip. One technique developed by the group involves two lithography exposures and two developments: first, the outer edge of the chip is exposed with higher than required exposure dose and developed to remove the edge beads; the PR film left has good uniformity and the second exposure and

Recipe	ICP	Bias	O_2 flow	Pressure	Etch rate
SPTS 1	2000 W	200 W	100 sccm	15 mTorr	500 nm/min

Table 5.1 – Diamond vertical etch recipe
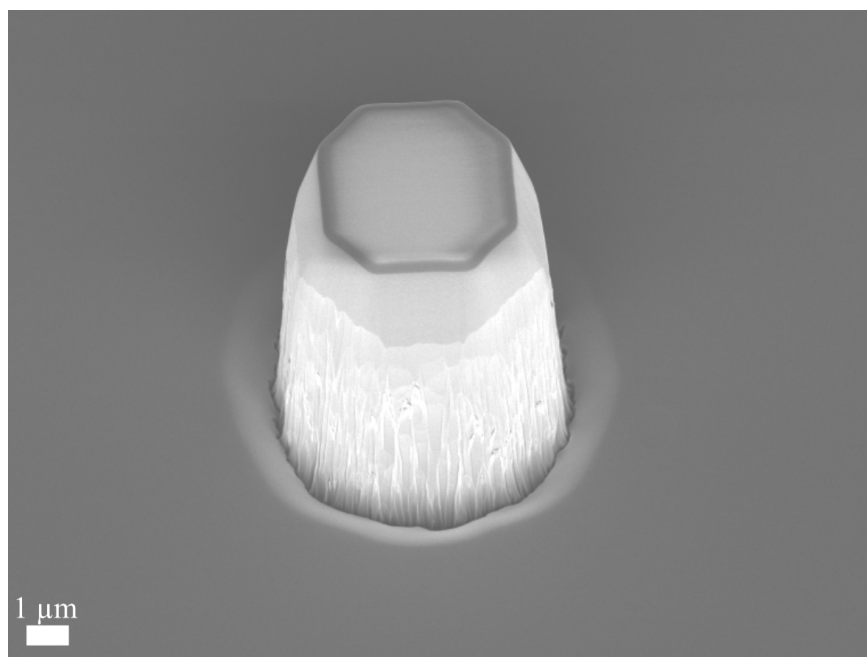
Figure 5.4 – SEM of a diamond pillar after 15 minutes of etching (SPTS 1). Two areas of the sidewalls are identifiable: a top smooth part and a bottom part. The effect is caused by the hard mask receding during etching.

development yield exceptional resolution [222].

The design was transferred into the hard mask and the diamond using DRIE (SPTS APS Dielectric etcher). For the diamond etch, a highly anisotropic and dense oxygen plasma was used (see table 5.1). We etched the diamond to form ~12 μm tall pillars. For long etches, the hard mask starts to recede and the sidewall is not vertical, but positively angled with two different slopes (figure 5.4). While the upper portion of the sidewall is smooth, the sidewall profile may not be desirable. For this fabrication flow the angle is not important, and it may be even beneficial due to the smoothing that occurs in the top part, however in other application it may be a potential failure point. Optimization of the vertical etch recipe for single crystal diamond will be discussed in the next chaper, in section 6.1.3. The used recipe (labeled SPTS 1 in the table) is better suited for etching a large volume of diamond quickly [222].

The chip is detached from the silicon carrier. We strip the SiO_2 mask in a bath of BHF. To prepare the sample for FIB milling, we sputter a 50 nm Al adhesion layer and a 75 nm Cr layer with an Alliance-Concept DP 650. We structure the pillar by milling from two directions
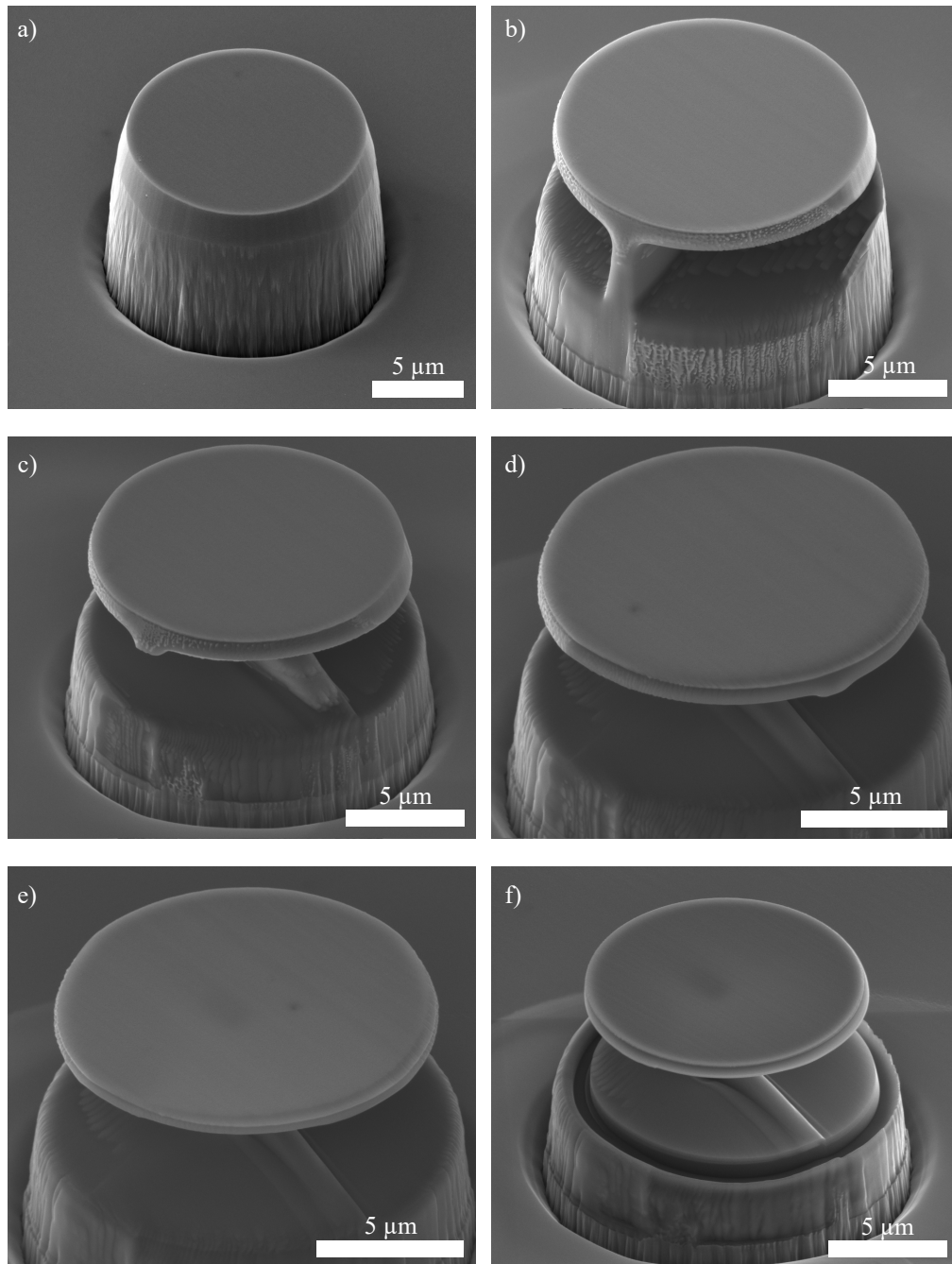
Figure 5.5 – SEM recordings at different stages of the FIB undercut process. Starting from an Al and Cr covered diamond pillar (a), the structure is etched from two (quasi)orthogonal directions (b-c). The disk is gradually thinned until the desired thickness alternating the two directions and gradually reducing the ion current (d-e). Finally the sidewall are smoothed by aligning the ion beam to the top surface and removing the outer part of the disk. The final smoothing is required to remove the rounding and roughening produced in the previous step. A layer of redeposited carbon and gallium is visible around the pillar and in the last image.

parallel to the top surface, in order to create a square section pillar. The milling procedure resembles a TEM lamella fabrication: the pillar is milled alternating the two directions, and the ion current is gradually reduced from $1\,\text{nA/cm}^2$ to $100\,\text{nA/cm}^2$, using an extraction voltage of $30\,\text{kV}$. The Gaussian profile of the ion beam generates a rounding of the micro-disk sidewall, especially visible when milling a large diameter disk due to the longer milling required. Since the etch rate of diamond is very slow, a very thick masking material would be required to have a sharp edge when milling horizontally. After creating the pillar, the sample is oriented so that the ion bean is normal to the top disk surface, and the outer edge of the disk is milled to improve the smoothness and to achieve a sharp sidewall. Here a thin ring pattern, scanning inwards, with small ion current is used. In this case, the thin metal layers are sufficient to resist the milling time required to etch less than $1\,\mu\text{m}$ (the disk target thickness), and it is therefore possible to obtain a micro-disk with sharp and symmetrical sidewalls. The procedure allows to mill most of the material rapidly with high current, and allows to obtain a smooth and precise bottom disk surface.

5.2.1 Cleaning and annealing

Following the FIB milling, cleaning the sample is necessary. Part of the material is redeposited in proximity of the milled area. We expect that this layer is composed of carbon, gallium, aluminum and chromium. Moreover, part of the metal mask remains on the top surface of the micro-disk. The masking metals are easily stripped using wet etchants. Gallium and amorphous carbon are more resistant to oxidizer solutions, such as piranha (H_2SO_4 96%, H_2O_2 30%, 3:1) or aquaregia (HCl 37%, HNO_3 70%, H_2O, 3:1:2). One option [223] is to use percloric acid, $HClO_4$, mixtures, since it has been reported to etch amorphous carbon. However, working with $HClO_4$ mixtures, e. g. the "tri-acid etch" is particularly complex, more than piranha, aquaregia, or hydrofluoric acid, due to the risk of explosion if the fumes are not collected adequately. We found that hydrofluoric acid followed by microwave O_2 plasma (Tepla GiGaBatch barrel plasma stripper, 200 W, 200 sccm O_2, 0.5 mbar) was efficient in etching the redeposited layer.

The removal of the Ga^+ implatation was investigated. Other works proposed to anneal the diamond at high temperature to remove the FIB-induced damage layer [177, 224], and it is generally accepted as an effective method to remove this layer. Different annealing procedures were tested, and the results were assessed by measuring the optical quality factors (see section 5.3) and by Energy Dispersive X-Ray spectroscopy (EDX). We anneal the sample at $500\,^\circ\text{C}$ in air for several hour, and we clean the sample in HF after each annealing step. After 4 hours, no Ga^+ signal is detected with EDX. Optical characterization showed an improvement of the quality factor of 5 times (figure 5.9). Further annealing with the same conditions did not improve the optical quality factor. Similarly, annealing in vacuum (6×10^{-6} mbar) at $1200\,^\circ\text{C}$ for 4 hours did not produce any change of the optical quality.
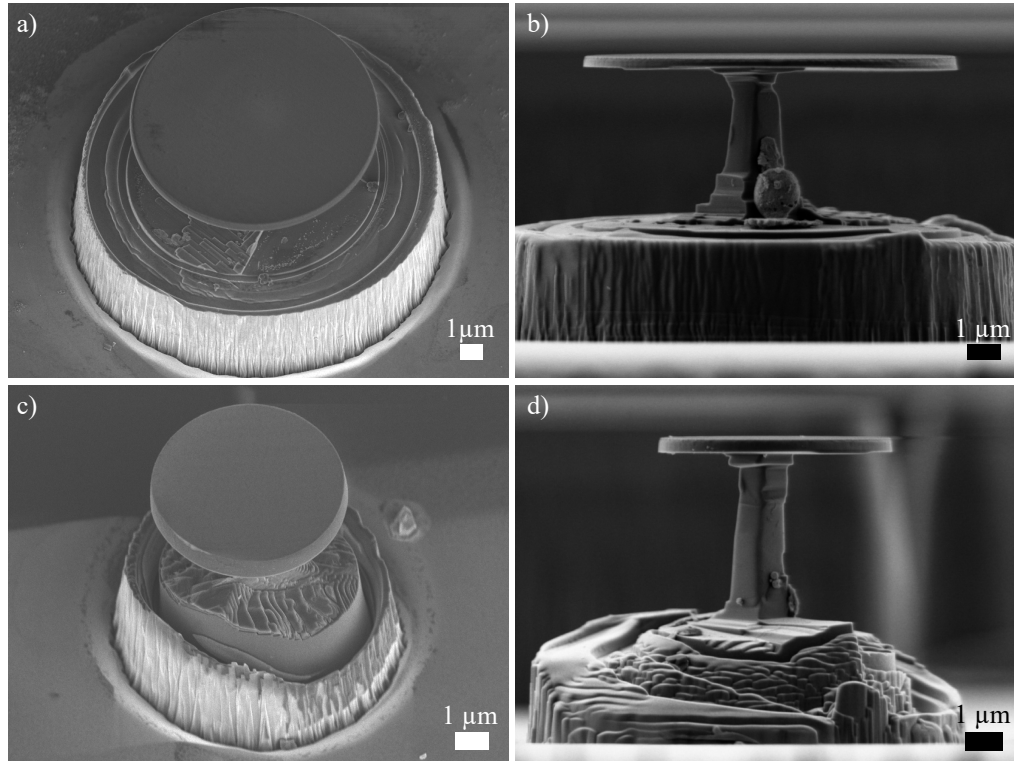
Figure 5.6 – Microdisks after annealing and cleaning. a-b) Tilted SEM recordings of a microdisk with diameter 10.5 μm and thickness 300 nm. In (b) the square section pillar is visible. A "strawberry" shaped gallium agglomeration is shown at the base of the pillar. During annealing, the implanted gallium diffuses at the edge of the structures and agglomerates into spherical shapes. When the agglomeration is particularly large, it does not etch completely in the HF bath. Tilted SEM recordings of microdisks with diameter 5.9 μm and thickness 800 nm (c), and with diameter 7.3 μm, thickness 350 nm (d).
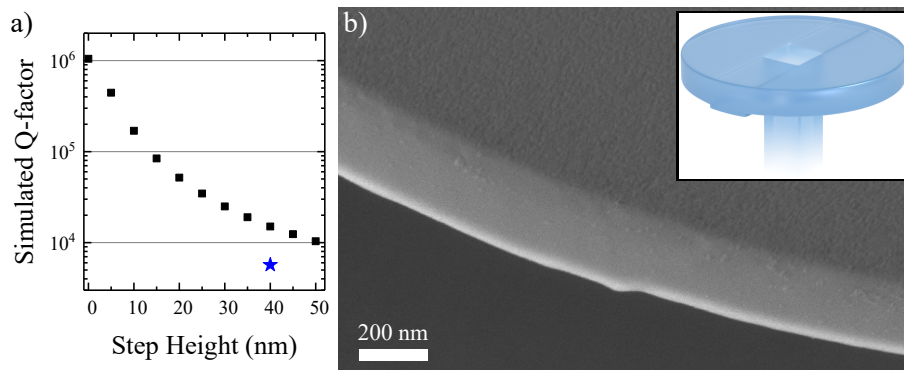
Figure 5.7 – a) $Q_{o,rad}^{sim}$ for different step height. The results are from a 3D COMSOL simulation. The blue star is the measured quality factor. b) SEM of the microdisk sidewall showing the step, the smoothness of the sidewalls achieved with FIB milling, and the roughness of the top surface. In the inset there is a 3D model rendering to visualize the step.
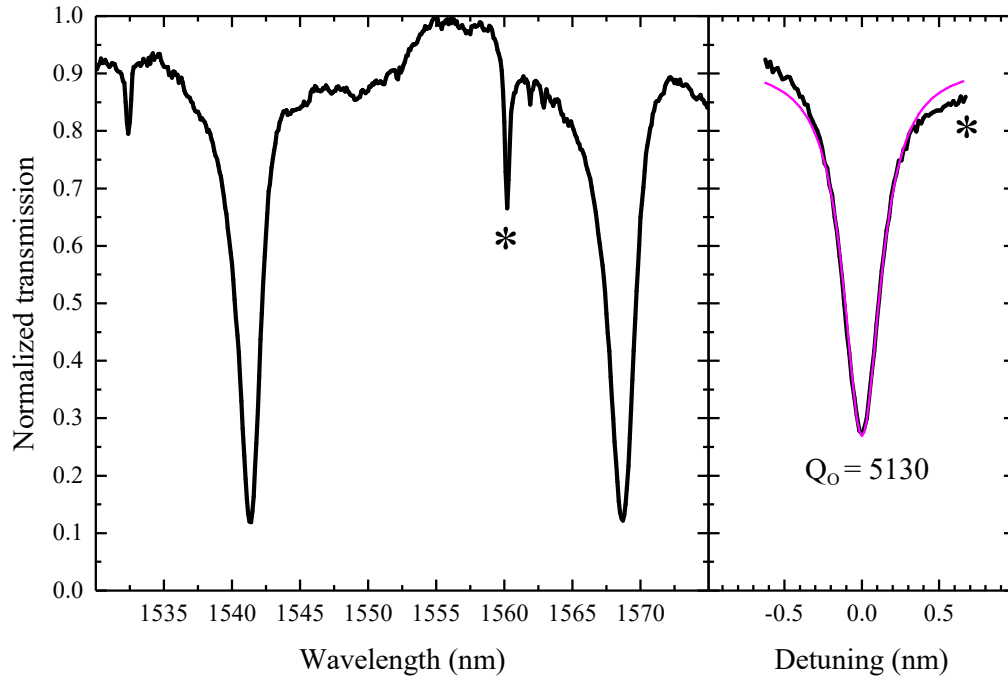
Figure 5.8 – Transmission spectrum of a tapered aligned to a diamond microdisk (diameter 10.5 µm, thickness 300 nm, figure 5.6(a)). Two mode families are identifiable, $TM_{1,m}$ and $TE_{1,m}$. The TE resonance identified with * measures a quality factor of 5130.

5.3 Optical transmission characterization

The microdisk are characterize by measuring the transmission of a tapered fiber as described in section 4.4.1. Figure 5.8 show the transmission spectrum of a a diamond microdisk (diameter 10.5 µm, thickness 300 nm). Optical quality factors are measured of the order of 5000. In the spectrum the FSR is visible and measures 25 nm. Two mode families are recorded, $TM_{1,m}$ and $TE_{1,m}$, as they appear in the spectrum with different polarizations (controlled by a polarization controller). The narrower resonances are assigned to the TE polarizations, since this polarization is less sensitive to the top and bottom surface roughness. The high resolution scan is measured at the critical coupling with optimized laser polarization. Critical coupling is reached when the maximum of the laser power is coupled to the microresonator (section 2.1), and it depends on the fiber-resonator separation. To find the correct gap, the fiber position is tuned while observing the transmission spectrum. The correct position is found when the extinction is maximized.

In figure 5.9 the effect of the annealing is shown. The red spectrum corresponds to the transmission spectrum of a diamond microdisk (diameter 5.9 µm, thickness 800 nm) before the post release treatments and the blue to the transmission spectrum of the same microdisk after the annealing for 4 hours at 500 °C in air. We can notice a blue-shift of ~7 nm and a narrowing of the linewidth of 5×. The corresponding resonances before and after the anneal-
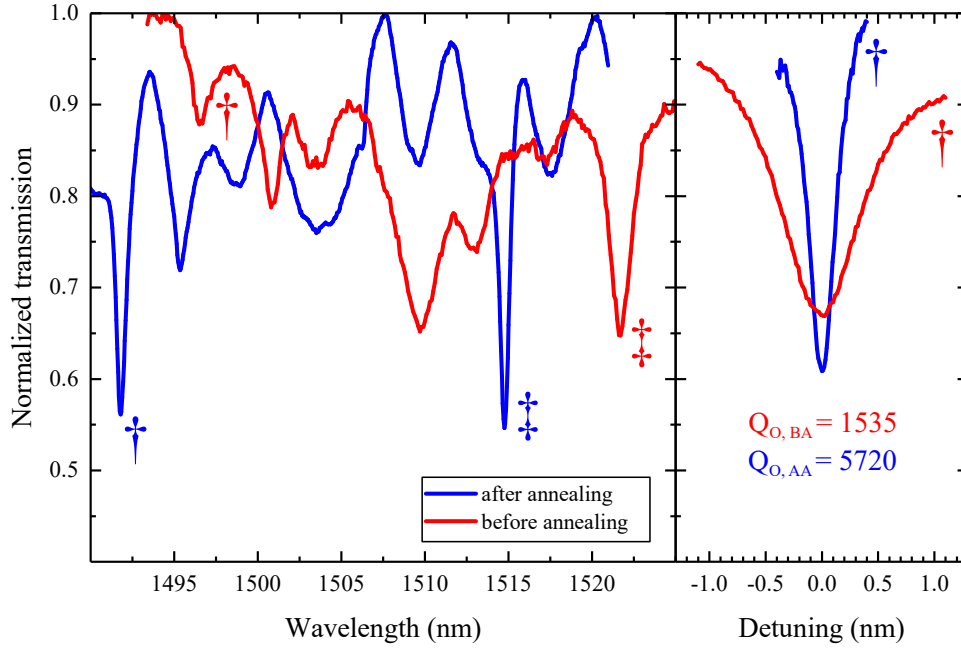
Figure 5.9 – Transmission spectrum before and after the annealing step at 500 °C. Both a blue-shift of approximately 7 nm and an increase of the optical quality factor of 5× are recorded. The measurement is relative to a thicker microdisk (diameter 5.9 μm, thickness 800 nm, figure 5.6(c)) therefore an extra mode family is present in the spectrum, corresponding to the $TE_{1,2,m}$.

ing were identified by analyzing the transmission at different polarization. If we consider the simulations of the ion implantation described in section 4.3, the gallium implantation extends for approximately 10 nm from the surface, and we can expect the damage to the crystalline material to extend further in the material of a similar length. If we consider the resonance condition in a WGM cavity as $2\pi r_{eff} = m\lambda_c/n_{eff}$, etching of the microdisk during the annealing would produce a change of the radius corresponding to

$$\Delta r_{eff} \approx \frac{m\Delta\lambda_0}{2\pi n_{eff}};$$

(5.1)

if we assume that n_{eff} does not change substantially during the annealing. For the 7 nm shift recorded in the transmission spectrum, the corresponding radius change is $\Delta r_{eff} \approx 15$ nm, which is of the same order of the simulated damage layer depth. This result is consistent with the results reported by Kawasegi et al. [224], since the irradiated area is selectively etched after thermal annealing. On the other hand, if we assume a change of n_{eff}, the blue-shift can be explained if the annealing converts the phase of the material from a high refractive index layer

to a diamond layer. We can express the effective index change as

$$\Delta n_{eff} \approx 2\pi \lambda_0 \frac{r_{eff}}{m},$$
(5.2)

which yields $\Delta n_{eff} \approx 0.002$. While it may appear negligible, COMSOL simulations can produce similar blue shift ($\Delta \lambda_0^{sim} \approx 6\,\text{nm}$) if we include a 20 nm layer at the outer edge of the microdisk with $n = 3$. Amorphous carbon, graphite, and diamond-like carbon have higer refractive index than diamond [224], therefore phase conversion is also a possibility. It is reasonable to assume that a combination of etching and of phase change occurs during the annealing. Direct measurement of the size change would be rather challenging due to the relative difference and the complex geometry.

5.4   Photoluminescence

A photoluminescence spectrum was acquired to assess the crystal quality of the resonator and to identify stimulated emission from eventual color centers. While this characterization does not give information on the quality of the device as an optomechanical cavity, we can obtain valuable information on the quality of the fabrication and its applicability to enhance the emission of photons from the crystal defects, useful to create a diamond based (single) photon source. The first order and second order Raman peaks of single crystal diamond are present in the spectrum and we do not report any broadening or additional peaks that might suggest the presence of non-diamond phase in the sample. No luminescence from NV or SiV centers is recorded. The starting substrate had no luminescence relative to these color centers and it is unlikely that any nitrogen or silicon impurities could be included in the diamond resonator during fabrication.

We observe luminescence around 740 nm (figure 5.10. This luminescence is associated with the GR1 emission [225], indicating that the damage to the crystal structure is not completely recovered. The luminescence could also be associated with a chromium-related color center [115], but limitations in the grating and laser wavelength combinations do not allow to observe the eventual chromium-related peak, that has a strong luminescence peak at 750 nm. The presence of chromium would not be surprising since it is one of the metal deposited as a protective layer and could be implanted by the ion beam during FIB milling. Regardless of the origin of this luminescence, we can observe enhancement of the emission due to the optical cavity. In the PL spectra, the cavity effect appears as narrow peaks over the luminescence, visible in figure 5.10 in the blue and red lines, which correspond to the spectrum acquired at the disk center and the disk edge. The wavelength resolution ($\sim$0.1 nm) of the prevent precise assessment of the optical quality factor of the resonances, placing an upper limit to the measurable Q_o to 7400. However, when a fit of the background luminescence is removed from the raw data, cavity resonances are recognisable with a FSR of $\sim$ 10 nm (equation 2.1), which
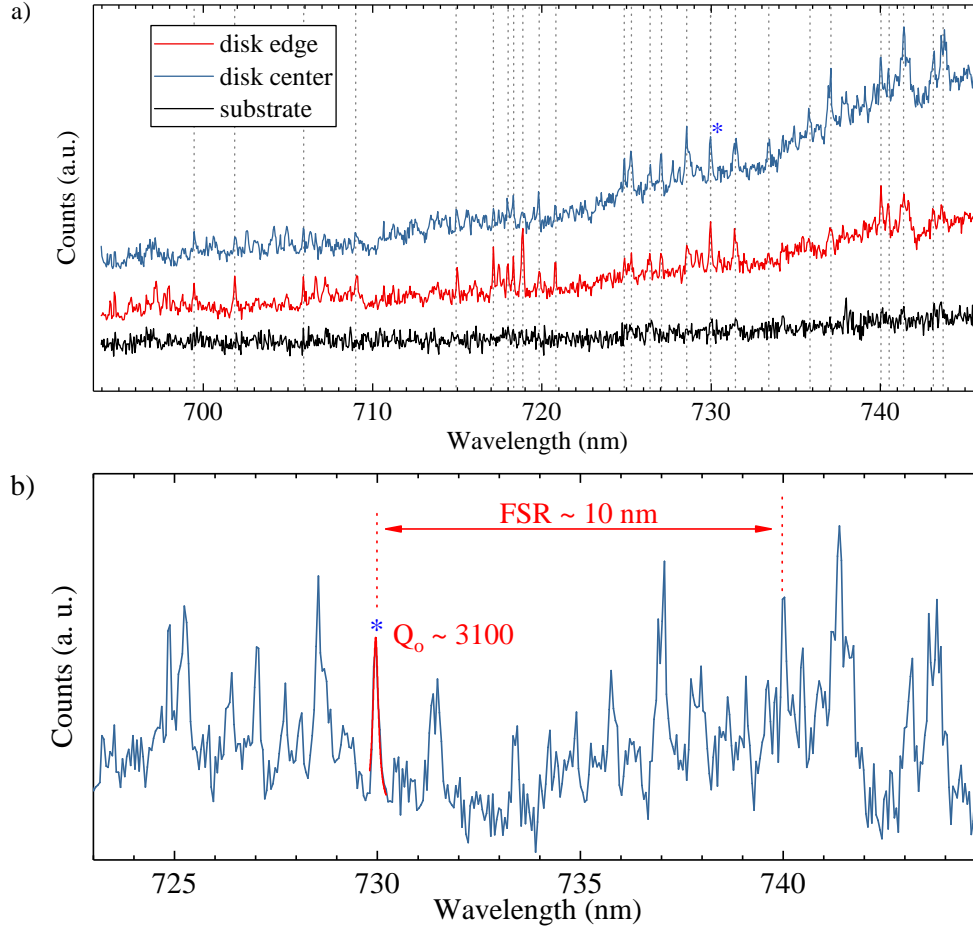
Figure 5.10 – a) Photoluminescence spectrum of the GR1 center with the laser pump spot focused at different points on the diamond microdisk. The dotted gray lines indicate resonances that are visible at the same wavelength when the laser is focused at different positions. The spectrum relative to the substrate was acquired close to the microdisk and it is above the noise floor. The spectrum was acquired with the Ramanscope using a 405 nm laser pump. b) Signal acquired with the laser focused on the disk center. The background GR1 luminescence was removed by subtracting a fit from the raw data, revealing the cavity resonances. We can identify a FSR of ~ 10 nm, consistent with the radius of the measured microdisk (3.7 µm, figure 5.6(d)). Fitting (red curve) of the resonances reveals $Q_o \sim 3100$.

matches with the expected value of a microdisk with a radius of 3.7 µm. Lorentzian fitting of the peaks reveals Q_o of the order of ~ 1000, with a maximum of 3100 measured at ~ 730 nm.

5.5 Discussion

Suspended single crystal diamond microdisk resonators were fabricated with an optical quality factor of 5720 at 1492 nm. A combination of DRIE and FIB milling were employed for the fabrication. While FIB milling is versatile for the structuring of 3D devices, it included few

problems that required post release treatments. Thermal annealing was efficient in removing (most of) the FIB-induced damage, providing an increase of the optical quality factor of 5×. However, the achieved optical quality prevents the use of the suspended microdisk as a optomechanical resonator. The required laser pump power would exceed the output power that is realistically achievable with laboratory equipment.

Q_o is strongly limited by the scattering. 3D COMSOL simulations show that bottom surface discontinuities quickly degrade the quality factor. Achieving better focus and using a smaller ion current can help reducing the "step" height down to the ~10 nm range, where the expected quality factor should increase of one order of magnitude. Reducing the top surface roughness should also help in this sense. Scattering limited Q_o is inversely proportional to the surface roughness. An alternative approach to reduce the roughness induced by the thermal annealing is is to perform a first higher temperature annealing in vacuum (>1000 °C) [177] to diffuse the gallium at the surface, followed by HF cleaning, and a final annealing in air at lower temperatures to remove the non-diamond carbon phase. Considering equation 2.4, improving the scattering limited Q_o can give a substantial improvement to the overall Q_o since the other sources of optical losses are relatively small.

Exploring other resonator geometries can be a viable route to achieve high Q_o using this fabrication method. The main limitation is represented by the alignment during FIB milling. A photonic crystal beam or membrane should not require alignment and can be good candidate. However, similar fabrication methods for this type of resonators were already discussed in literature, where limited Q_o are reported [176, 226]

6 Crystallographically etched diamond microresonators

This chapter will describe the diamond microresonators fabricated with a "quasi-isotropic" undercut or crystallographic etch. The fabrication process is based on the the process used by the group of Paul E. Barclay to create suspended diamond beams [25] and microdisk resonators [178, 184, 192]. The process has been employed by other groups to create suspended diamond cavities [180, 197].

The method allows to create suspended structures starting from a bulk substrate. It consists of an initial anisotropic vertical etch to transfer a mask pattern, followed by a quasi-isotropic etch to undercut the structure. The fabrication resembles the SCREAM process [227] for suspended silicon structures. In that case, the second etch step is an isotropic SF_6 etch, while for single crystal diamond it is an oxygen plasma with zero bias. The nature of the etch is not isotropic per se, since it has different selectivity towards the crystal planes, but it is possible to achieve a result similar to an isotropic etch by choosing the appropriate orientation of the starting crystalline substrate. The {110} plane family is etched preferentially, therefore starting from a {100} or {111} oriented substrate it is possible to fabricate a suspended slab with parallel to and bottom surface.

Compared to the FIB undercut, this method has the advantage of parallel processing of multiple resonators on a chip and it prevents the formation of the FIB-induced damage. However, it requires several processing steps that may have a small processing windows and it restricts the achievable resonator shapes. In particular, when creating more complex structures, like microdisks and microrings, the process may require several iterations to characterize properly the relative etch rates during the undercut, and the resonators must be (re)designed according to these etch rates.

6.1 Microfabrication

The detailed process flow is shown in figure 6.1. For this fabrication flow we decided to move to electron beam lithography to include other resonator structures that were designed after the
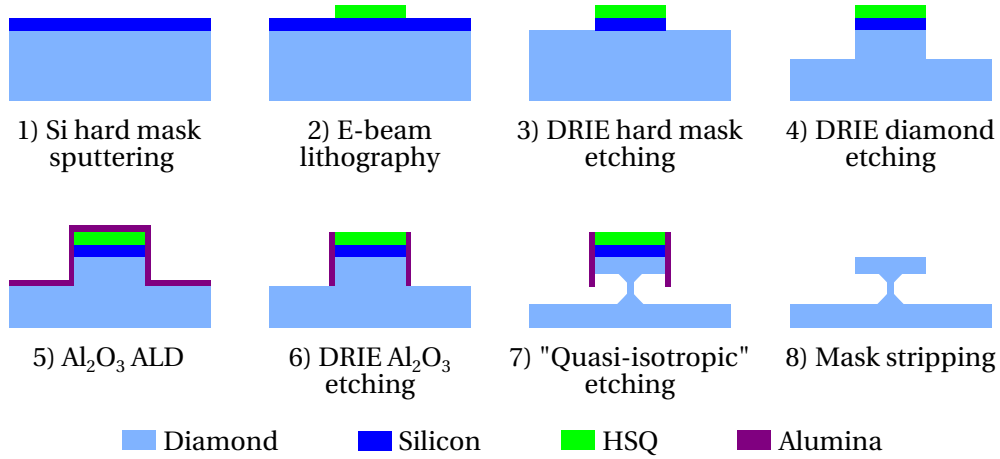
Figure 6.1 – Fabrication process using a "quasi-isotropic" etching. 1) Sputtering of a 300 nm Si layer to be used as a hard mask and grounding layer. 2) E-beam lithography using an HSQ resist. Transfer of the patterns into the Si mask (3) and diamond (4) using a vertical recipe (table 6.1). 5) Atomic Layer Deposition (ALD) of 75 nm of alumina. ALD is a conformal deposition with excellent coverage of the sidewalls. 6) Etching of the alumina layer to expose the top and bottom surface of the structures while keep the protection on the sidewalls. 7) "Quasi-isotropic" etching of the diamond structures. 8) Cleaning with HF and HNA.

initial experiments with the FIB-milled microdisk resonators. In particular microrings will be included. Given that critical dimensions of these structures are in the range of few hundreds of nanometer, e-beam is the only viable option. Moreover, following the work reported in [228], a surface preparation step was included at the beginning of the process.

6.1.1 Polishing and surface preparation

The starting substrates were single crystal diamond plates with {100} orientation from different suppliers (element6, LakeDiamond) with different surface polishing qualities. Scratches like the one shown in figure 6.2 are commonly found on commercial substrates. The density is rather high, substantially decreasing the potential fabrication yield. Therefore additional polishing, known as soft-scaife polishing, is required to obtain a smooth surface, with sub-nm RMS, without scratches. This technique is rather time consuming and expensive. In our group, we investigated an alternative approach to remove surface defects using ion beam etching (IBE), and we routinely use it before our diamond processing. Ion beam smoothing was already demonstrated [219], but the proposed strategy is to use low incidence angles to increase smoothness and prevent the formation of additional roughness. Such strategies, however, are not suitable to remove the deep scratches from polishing. By increasing the incidence angle, up to ~60°, these pits can be removed thanks to the angular etch rate dependence: the top flat surface receives ions at the most efficient angle, while the sidewall of the scratches at a lower angle, resulting in a slower etch. The technique is fast (~20 minutes) and it allows
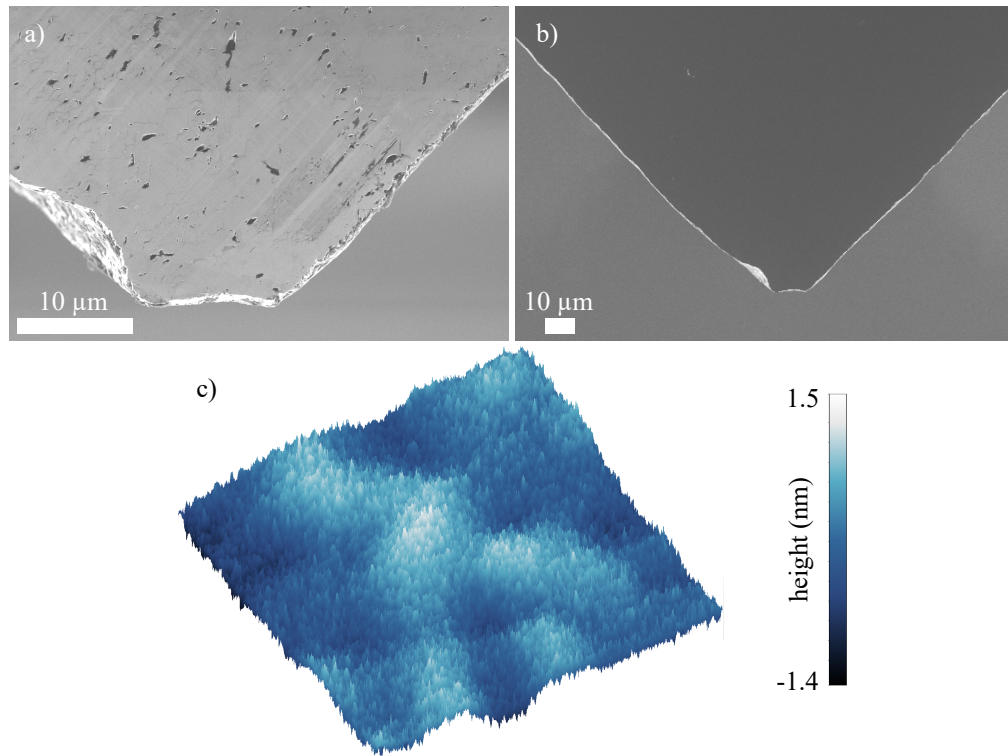
Figure 6.2 – a) Typical surface of as received single crystal diamond plate. Polishing scratches are clearly visible and very dense. b) Surface after 30 min of 700 eV Ar$^+$ ion milling at 60° incidence. c) AFM scan of a 1 μm × 1 μm area of the diamond surface after the full polishing procedure described in section 6.1.1 (courtesy of Sichen Mi). The IBE polishing produces a smooth surface (390 pm RMS), without the mechanical polishing defects.

processing of multiple diamond substrates at the same time. While the high incidence angle does increase the roughness of the top surface by developing a self-organized nanoscal pattern [229], a sub-nm surface roughness can be easily recovered by additional ion irradiation at incidence angles closer to the normal (~10°). The ion irradiation is very gentle and produces very little lattice damage due to the low acceleration voltage 4.7(c). The penetration depth is very confined and the thin damage layer can be easily removed by high temperature annealing in air. We reported a detailed analysis of the polishing technique in [228].

Moreover, given the low etch rate of diamond by the Ar ion beam, IBE can be used as a surface cleaning step to remove particles leftover from the mechanical polishing. We generally clean the diamond plates in HF and Piranha when we receive them, however not always foreign particles, especially the one trapped in the surface scratches, are removed. Therefore a low ion energy (300 eV) is used to remove the particles. At this acceleration voltage, the diamond etch rate is negligible. To summarize, the suface preparation and polishing used was perfomed in a Veeco Nexus IBE350, starting with a 10 minutes step at 10° and 300 eV, then 40 minutes at 60° and 700 eV, finally 10 minutes at 10° and 700 eV.

6.1.2 Electron Beam lithography

We employed electron beam lithography to pattern the diamond. In contrast to photolithography, either the substrate or the hard mask must be conductive to avoid charging effects due to the electrons used to expose the resist. Although the diamond substrates used are not electronic grade, the conductivity is still very low. Similarly, the silicon oxide used in the other process will not be able to ground the sample during the exposure. Metal, or conductive, layers are generally included in the layer stack for e-beam lithography. HSQ was chosen as e-beam resist because of the high resolution, negative polarity, and the resistance in dry etching. In particular, the negative polarity is highly beneficial for the type of structures we intend to fabricate. Only the area of the resonator needs to be exposed, saving e-beam time and allowing to have large openings to align the tapered fiber.

The choice of resist, restricted the use of some materials for the hard mask. Silicon oxide and nitride can't be used because of the insufficient selectivity of HSQ in the dry etch processes used. Sputtered silicon and alumina can be better suited. For the latter, an additional metal layer must be included to ground the surface. Given that HSQ is developed with TMAH based chemicals, only few metals can be used if deposited below the HSQ. It is possible to deposit a thin metal layer above the resist, however they cannot be sputtered to prevent exposure of the resist since UV radiation is emitted by the plasma during sputtering. Evaporation is an option, but it is rather time consuming compared to sputtering. Initial tests were performed with a stack of atomic layer deposited alumina and a thin layer of sputtered chromium. The stack performed well for the electron beam exposure, but the transfer of the pattern to the alumina layer was not possible due to the bad selectivity of HSQ in the $Cl/BCl_3/Ar$ plasma used to etch alumina.

Sputtered silicon demonstrated to be the best material thanks to the good selectivity compared to HSQ and diamond respectively. 300 nm of silicon were sputtered with an Alliance Concept DP650. Before coating, the samples were treated with low power oxygen plasma in a Tepla barrel stripper, and glued with Quickstick135 to larger silicon chips to facilitate the handling. FOX16, and HSQ dilution, was spun at 6000 rpm achieving a ~600 nm layer. Edge beads were present, but extended only ~100 µm, and they are not as relevant in e-beam lithography since the required dose does not change substantially with the thickness for FOX16. The patterns were exposed with a dose of ~2500 µC/cm^2, depending on the pattern, and a current of 1 nA, yielding a spot size of ~5 nm, over a 2 nm grid, using a Raith EBPG5000+. The resist was developed in 25% TMAH for 90 s. The pattern was transferred in the silicon layer using a Cl plasma (800 W ICP, 110 W bias, 50 sccm Cl_2, 5 mTorr) in a STS Multiplex ICP.

6.1.3 Vertical etch optimization

For this fabrication strategy, it is important to achieve vertical sidewalls during the first diamond etch step. Using the recipe V1 (table 6.1) sloped sidewalls due to mask erosion were produced, as described in the previous chapter. When the layer covering the sidewall is etched
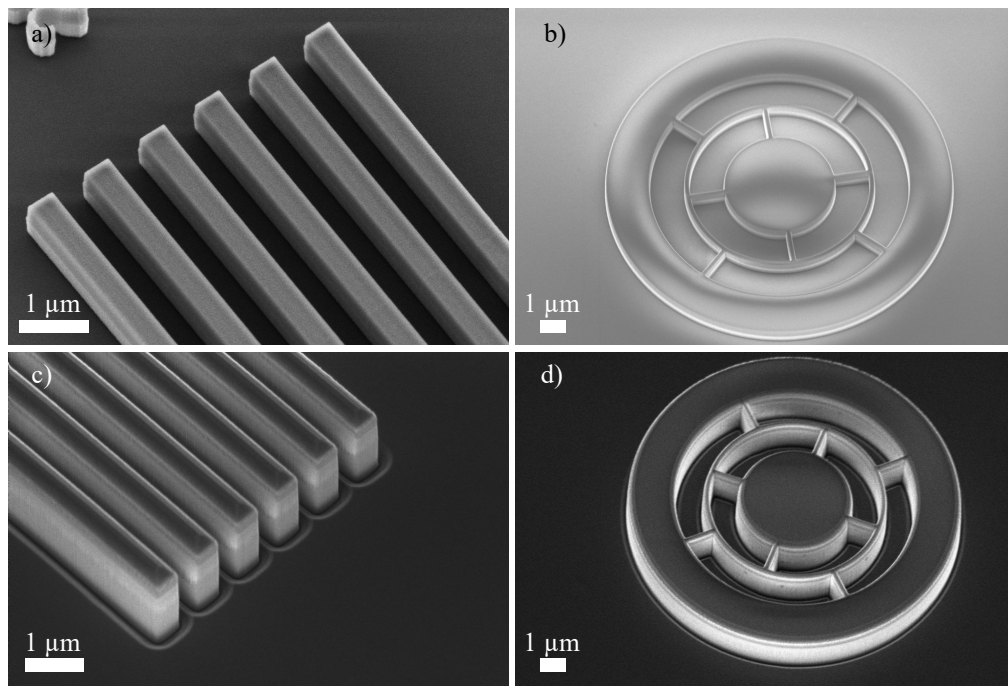
Figure 6.3 – a-b) SEM recording after e-beam lithography and silicon hard mask etching. c-d) SEM recording after diamond etching with recipe V2.

Recipe	Etcher	ICP	Bias	O_2 flow	Ar flow	Cl flow	Pressure	Etch rate
V1	SPTS	2 kW	200 W	100 sccm	-	-	15 mTorr	500 nm/min
V2	STS	400 W	200 W	30 sccm	-	-	10 mTorr	110 nm/min
V3	STS	400 W	200 W	30 sccm	6 sccm	-	10 mTorr	150 nm/min
V4	STS	400 W	200 W	30 sccm	10 sccm	-	10 mTorr	160 nm/min
V5	STS	800 W	100 W	-	-	50 sccm	5 mTorr	65 nm/min

Table 6.1 – Diamond vertical etch DRIE recipes

in step 6 (figure 6.1), the top part of the layer can be too thin or etched completely with a sloped sidewall. Using silicon instead of silicon oxide as hard mask does not change the sidewall angle. The high power can be the main culprit, but mask erosion could also be caused by chamber contamination, since the etcher is used primarily in our clean room for oxide and nitride etching with fluorine chemistry. Moving to a different etcher (STS Multiplex ICP) and reducing the ICP immediately improved the verticality of the etch. Starting from the V2 recipe, different Ar flows were tested, as well as a Cl based etch (same as the hard mask etch).

While the Cl based etch recipe (V5) produced a smooth sidewall, the chemistry is the same used for the silicon hard mask etch recipe, therefore not suitable for long etches. V2, V3, and V4 have very vertical sidewalls and good selectivity towards the hard mask, however the sidewall roughness is worse than both the V5 recipe and the original V1. Similar results happen when keeping the HSQ layer and stripping it before the etching. Increasing the argon flow does

Recipe	Etcher	ICP	Bias	O_2 flow	Temperature	Pressure
UC1	SPTS	2000 W	0 W	100 sccm	10 °C	15 mTorr
UC2	Sentech	1000 W	0 W	10 sccm	200 °C	12 mTorr
UC3	Sentech	1000 W	0 W	10 sccm	100 °C	12 mTorr
UC4	Sentech	1000 W	0 W	10 sccm	200 °C	15 mTorr
UC5	Sentech	1000 W	0 W	10 sccm	200 °C	30 mTorr
UC6	Sentech	1000 W	0 W	10 sccm	100 °C	50 mTorr
UC7	Sentech	1000 W	0 W	10 sccm	200 °C	50 mTorr

Table 6.2 – Crystallographic etch recipes

not show improvement of the sidewall smoothness. We decided to use the V2 recipe and investigate methods to improve the sidewall quality after the undercut (section 6.1.5).

6.1.4 Crystallographic etch

After the vertical etch step, the sidewall needs to be covered. An alumina layer is deposited with Atomic Layer Deposition (ALD) to ensure good conformal coverage of the sidewalls. Alumina was chosen for the great resistance to the oxygen plasma used in the crystallographic etch and for the ability to be easily stripped in HF after the release. 75 nm were deposited, corresponding to 675 ALD cycles, using a BENEQ TFS200. To keep the alumina layer only on the sidewalls, a blank etch in a $Cl/BCl_3/Ar$ directional plasma (800 W ICP, 150 W bias, 7 sccm Cl_2, 7 sccm BCl_3, 6 sccm Ar, 2 mTorr, STS Multiplex ICP) was performed until the floor was completely removed (about 90 s, 10 s after the endpoint was detected with the builtin interferometer). These steps correspond to 5 and 6 in figure 6.1.

Like anisotropic etching of silicon [230], the zero bias oxygen plasma etches the different crystal planes at different rates, in particular $\eta_{\{110\}} \gg \eta_{\{100\}} > \eta_{\{111\}}$, where η indicates the etch rate. Starting from a cylindrical pillar fabricated in a {100} oriented sample, we should expect the base to become hourglass shaped with an octagonal cross section, then evolving into an hourglass with square cross section as the etch continues. In practice is easier to measure the etch rates base on the relative direction, *up, down, lat*, and *lat**, as indicated in figure 6.4(a). For a pure crystallographic etch, we should expect that the pedestal is symmetric with respect to the plane of the diamond floor after the vertical etching step, i. e. that $\eta_{down} = \eta_{up}$, therefore narrowest point of the pedestal is aligned with the bottom of the alumina sidewall mask. However, given that commercial etchers have residual bias even when the RF source is turned off, the narrowest point should shift down.

Initially, the crystallographic etch was done using the recipe UC1 indicated in table 6.3, using the same parameters as reported in [231] for the fabrication of crystallographically etched gratings in single crystal diamond. While the nature of the etch is predominantly crystallographic, the undercut did not follow the desired profile. The vertical etch rate, η_{up}, was too
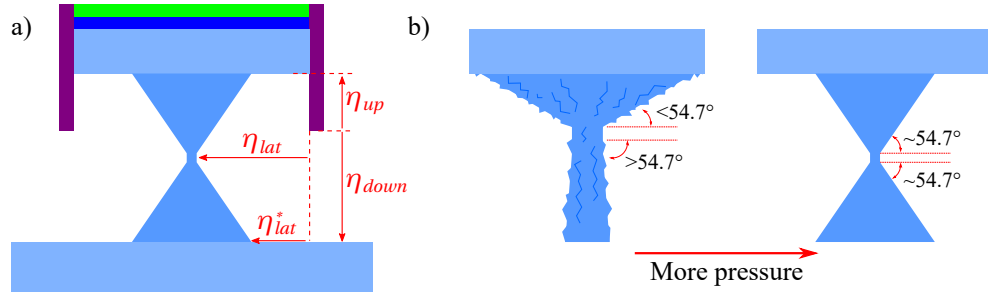
Figure 6.4 – a) Relative etch rate directions used to describe the etch profile of the crystallographic etch step. b) Illustration indicating the effect of process pressure for the undercut step. Higher pressure results in a better alignment of the etch profile to the diamond crystal planes. The value of the angle indicated in the illustration (54.7°) corresponds to the angle between the {100} and {111} crystal planes.

small to obtain a smooth {100} surface on the bottom of the devices. As analyzed in [231], we explain this behavior with residual plasma bias that causes a not negligible directional etching component. Similarly to the vertical etch (V1 recipe), the hard mask is attacked during the etch and it can fail. Again, as for the vertical etch case, this could be due to contamination of the chamber or by the high ICP power used. Using a different etcher solved the problem, and allowed to increase the temperature of the process up to 200 °C, while trading the high plasma ICP power. We developed the etch recipe using a Sentech ICP-RIE SI 500 etcher. Table 6.3 reports the etch recipes tested during optimization. The ICP power was set to the maximum that the tool could withstand for a prolonged period (1000 W), while changing pressure and temperature.

Temperature appears to influence the etch speed, while maintaing the relative ratio between the directional etch rates, η_{up}, η_{down}, η_{lat}, and η_{lat}^*. Etching at 100 °C was ~ 2.5 times slower than at 200 °C. A good thermal contact is important for a repeatable etch. Contrary to all other processing steps, it is not possible to use Quickstick during the etch step at high temperature, since the process temperature can be above the flowing point of the wax. Moreover, when the wax is heated too quickly the diamond chip is "launched" off in the chamber. Therefore Fomblin oil was used to attach the chip to the carrier wafer. The downside is a worse thermal contact compared to Quickstick. Insufficient amount of oil may cause the diamond chip to overheat, accelerating substantially the etch speed and making the process unreliable. Pressure has a strong influence on the directional etch rates ratio. Increasing the pressure makes the process more anisotropic, with the etch walls better aligned to the crystal orientation. Low pressure makes the etch profile asymmetric in the vertical direction, decreasing η_{up} and $\eta_{lat,top}^*$ relative to the etch rates in the other directions. Figure 6.4(b), shows how the profile changes with the change in pressure. We observe a variation of the final thickness of the structures depending on the lateral dimensions and the distance from other nearby structures. Narrower structures are thinner compared to larger ones and small gaps slow down the etch. In fact, 1D photonic crystal beams may be completely etched if the process is timed
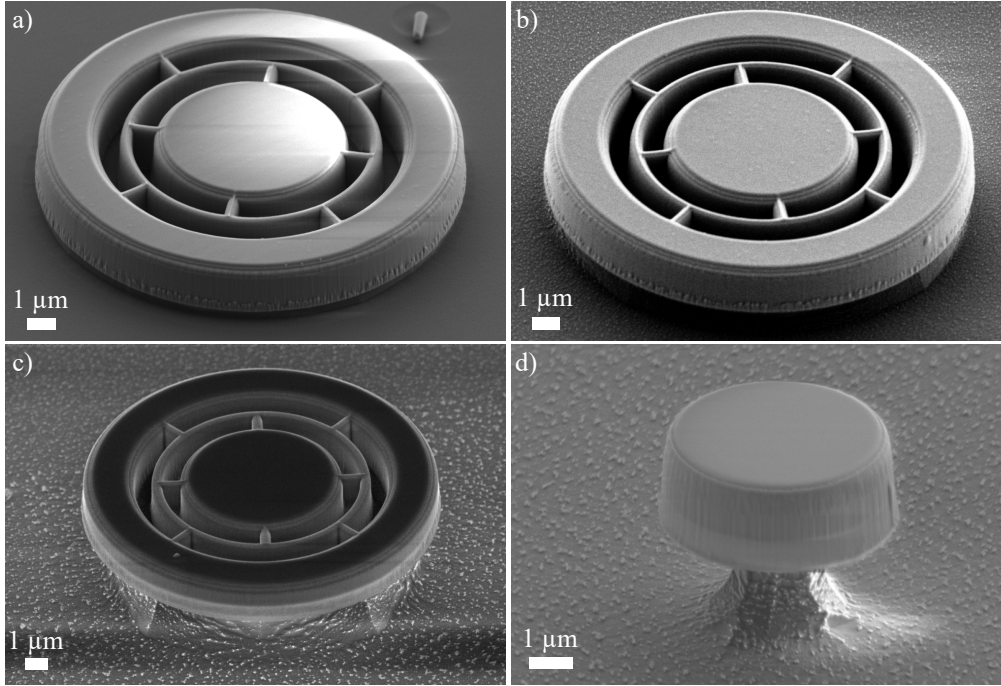
Figure 6.5 – SEM recordings of the crystallographic etch step. Structures after 2 h (a) and 5 h (b) with recipe UC6. This recipe produces the smoothest etch walls but it is particularly slow ($\eta_{down} \approx 200$ nm/h). c-d) Structures after 3 h of etching with recipe UC7. The SEM recording was acquired using a high (5 kV) acceleration voltage and it is possible to measure the upwards etch by imaging through the thin alumina layer.

to achieve microdisks and microrings of the desired thickness. We observed the influence of the gap in multiple structures with different magnitudes. On the lithography mask we included WGM resonators coupled to suspended waveguides with narrow gap, the microrings with concentric supports described in section 4.2.1, and microdisks surrounded by a guard ring. Typical gaps in these structures go from 150 nm in the waveguide coupled resonators and the microrings, to several μm for the microdisks surrounded by the guard ring. The effect is particularly evident in the waveguide coupled resonators, where the resonator thickness is not symmetric, increasing substantially on the side of the waveguide. The microdisks surrounded by a guard are up to 2 times thicker than isolated microdisks with same diameter. In the case of the concentric microrings, the undercut proceeds mostly from the outside, eventually allowing to design smaller central supports (and thus smaller rings). The influence of the gap changes depending on the process pressure, and the effect is reduced at higher pressures.

The optimized process is indicated with UC7 in table 6.3. Starting from a 2 μm tall structures, approximately 7 h are required to obtain an undercut of ~ 1.5 μm at the bottom surface of the resonator, of ~ 3 μm at the narrowest point of the pedestal, and a resonator thickness of < 500 nm. To increase control in the final part of the undercut, we can reduce the temperature in the final hour using the recipe UC6 in table 6.3, preventing overetch and collapse of the narrowest structures. The resonator thickness can be monitored easily by imaging with an
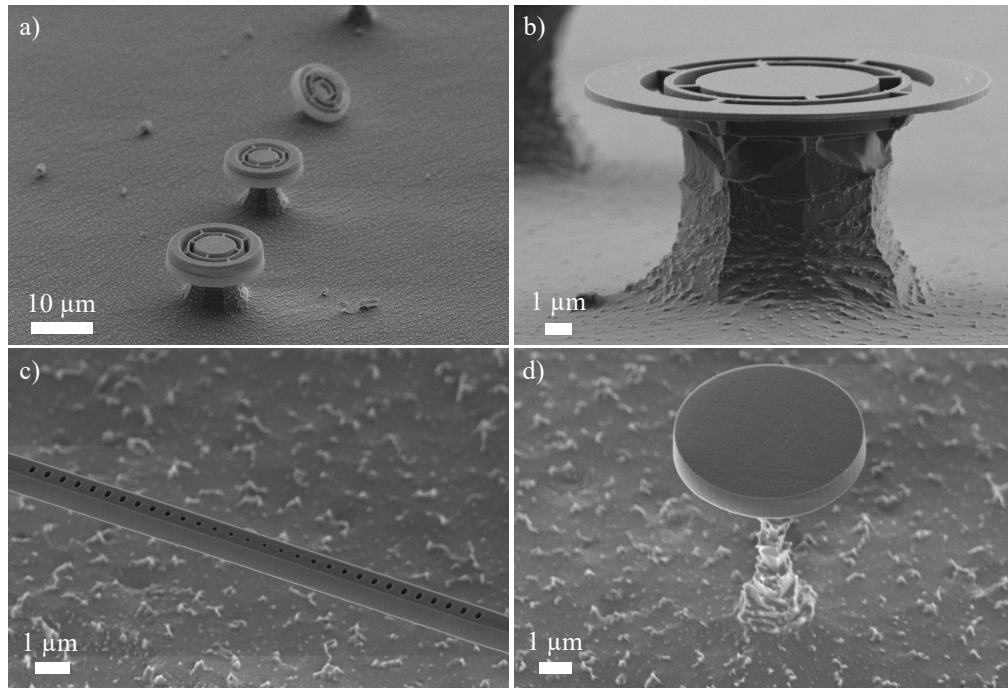
Figure 6.6 – a) SEM recording after 6 h of etching with recipe UC5. Depending on the lateral dimension of the lithography pattern, some structures collapse due to excessive undercut. b) Same sample after hard mask stripping. The image shows the side of a microring. Photonic crystal beam (c) and microdisk (d) fabricated using the UC4 process. The lower pressure makes the etch floor and the pedestal wall rougher than the higher pressure processes.

SEM at high voltage (>5 kV), thanks to the low thickness of the alumina layer covering the sidewalls. After the sufficient etch time, the hard mask is stripped with HF and HNA. Figure 6.5 shows the results of the crystallographic release after the hard mask etch. Compared to other implementation[178, 180, 197] of this crystallographic etch step to suspend single crystal diamond structures, we can achieve very similar results, however the walls can be rougher, especially the non {111} faces. Increasing the ICP power can improve the smoothness of the undercut walls, as we can obtain using the UC1 recipe (which uses 2000 W ICP power) and as reported by [178] (3000 W ICP power).

Table 6.3 indicates the etch rates measured for the recipes UC4-7. UC1, UC2 and UC3 are not included as they results on a pedestal of the wrong shape. Khanaliloo et al. reported a $time^2$ dependency for the etch depth [178], however for our etch recipes we have an error of ~ 20 nm after 5 h (for the etches at 200 °C) if we consider the etch rate constant. We measure the etch depth by SEM imaging, and the precision can be of the order of 10 nm. A more precise measurement method should be employed for a precise characterization of the etch rate, but for our application, the error magnitude is acceptable.

Recipe	η_{down}	η_{lat}	η_{down}/η_{lat}	η_{up}	η_{down}/η_{up}
UC4	1175 nm/h	375 nm/h	3.1	250 nm/h	4.7
UC5	770 nm/h	530 nm/h	1.45	275 nm/h	2.8
UC6	235 nm/h	130 nm/h	1.8	-	-
UC7	720 nm/h	520 nm/h	1.38	300 nm/h	2.4

Table 6.3 – Etch rates calculated for the recipes UC4-7.
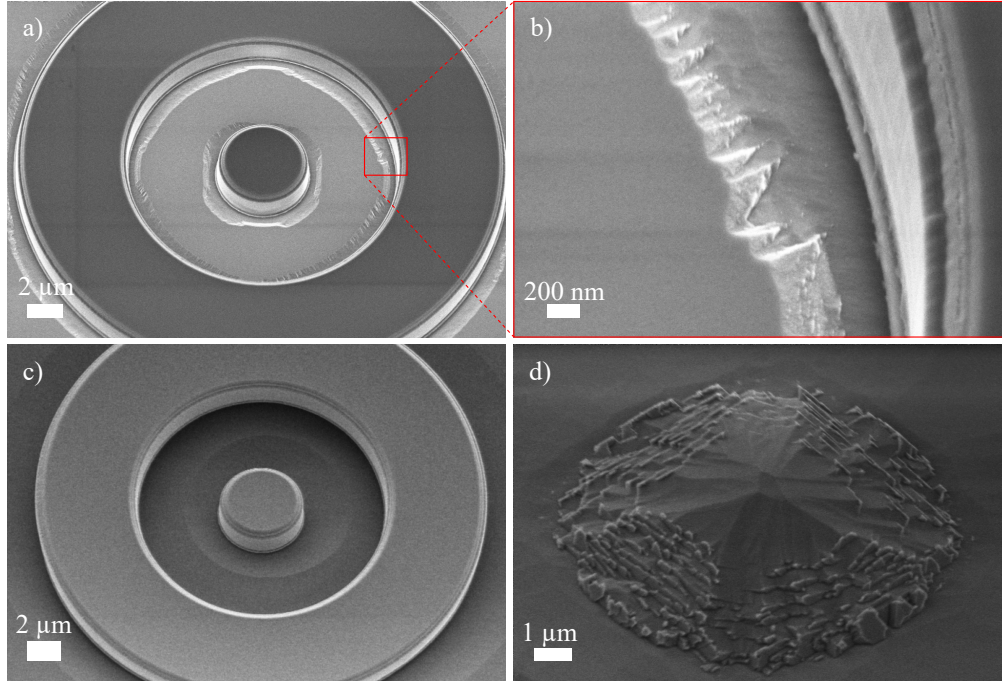
Figure 6.7 – Etching of diamond at 750 °C at ambient pressure. a-b) Etching after 30 min. The etching is proceeding in the ⟨110⟩ directions leaving smooth {100} planes. c-d) Etching after 8 h. The pillar was completely undercut, exposing {111} faces.

High temperature annealing

The crystallographic etch step is very similar to "burning" the diamond. At high temperature (>600 °C) in an oxygen environment, the diamond can be etched. The process can be anisotropic, and the selectivity of the {100} and {111} faces can be influenced by the environment [232, 233]. We explored oxidative etching of diamond in an oven at ambient pressure, annealing the diamond at 750 °C for up to 8 h. The sample was prepared following the same process flow (figure 6.1), with the step 7 ("quasi-isotropic" etching) performed in the oven. The images in figure 6.7 show the sample after different annealing times. The condition used appear to etch the {110} planes preferentially, leaving a smooth {100} floor. 8 h of etching caused the complete etching of the support pillars and of the resonators, leaving some roughness in the place of the supports, with faces that appears to be of the {111} family. From the images after 30 min, the etching proceeds along the ⟨110⟩ directions, therefore this technique

can be optimized to fabricate freestanding structures in single crystal diamond. However, the drawbacks compared to the plasma etching are significative. For instance, the process cannot be precisely timed, since the oven has a certain thermal inertia, while a plasma can be precisely ignited and turned off. Temperature fluctuations in the oven can drastically change the selectivity of the etching. Finally, the alumina mask used for the sidewall protection is deformed in at high temperature. The process, however, could be employed as an additional smoothing step of the bottom surface of the microresonators after the plasma based crystallographic etch in case a smooth surface cannot be achieved.

6.1.5 Sidewall polishing

To achieve high Q_o, the smoothness of the resonator surface is important to minimize scattering. Sidewalls are often responsible of most of the losses due to the roughness induced by the vertical etch step [189]. We can identify two main causes of sidewall roughening during etching: the first one is the erosion of the hard mask, and the second can be attributed to the interaction of the plasma with the material to be etched. The optimization of the vertical etch described previously was aimed at addressing the latter. However, no substantial improvement were found on the sidewall smoothness, and we can assume that the main source of roughness is the hard mask erosion. For this reason, a post processing smoothing step was investigated.

The procedure is based on the IBE polishing employed to prepare the diamond surface before microfabrication. Given the different incidence of the Ar^+ ions of the top surfaces and of the sidewalls, the angle must be chosen appropriately to avoid creating additional roughness. At 45° of incidence the ions tunnel through the diamond lattice, decreasing drastically the sputtering yield. However, the angle should be close to this value to avoid the roughening that occurs at high angles. Figure 6.8 shows the effect of low acceleration ion milling on the top surface and the sidewalls of freestanding diamond structures. The best results were achieved using 500 eV Ar^+ ions at 50° of incidence respect to the top surface normal, while rotating the substrate holder at 10 rpm. In this configuration, the top surface is milled by the ion beam at ∼ 50°, while the sidewalls at ∼ 40°. After 14 min of milling, the roughness is drastically reduced (figure 6.8(c)). Deviating more from this incidence induces the formation of "steps" on the top surface or on the sidewalls (figure 6.8(d)). Of course this method will reduce the thickness and the lateral dimensions of the structures. At 50° incidence, the 500 eV Ar^+ beam will etch single crystal diamond with a speed of ∼ 4 nm/min both the the vertical and in the lateral directions. It is critical to do thorough cleaning of the sample before the treatment, as particles eventually present on the structures can result in the formation of protuberances (figure 6.8(c)), that can't be removed with another IBE polishing step without roughening the sidewalls. As for the surface polishing, this sidewall polishing technique can be applied to other materials, both amorphous and crystalline. For the latter it can be particularly attractive, as can emulate the reflow processes that can be performed in SiO_2. The effectiveness of the treatment will be discussed in section 6.2.
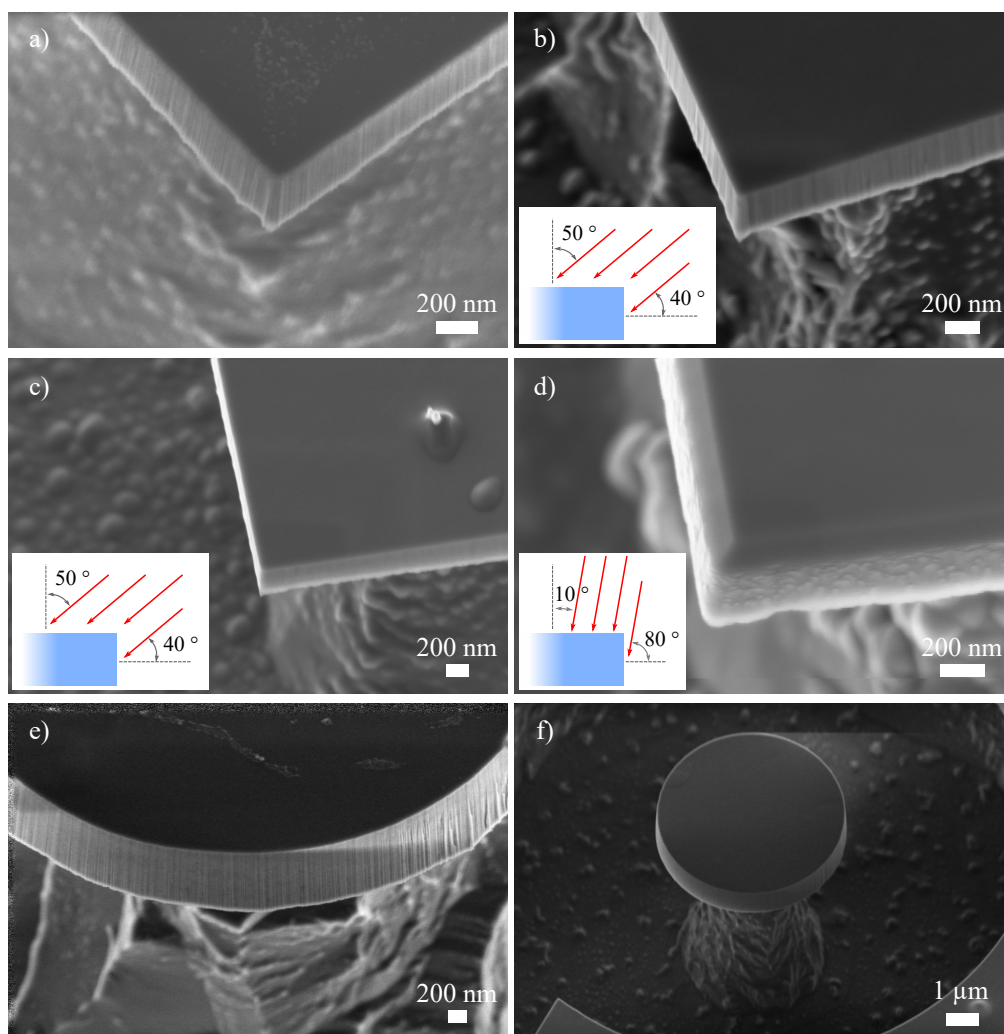
Figure 6.8 – Sidewall polishing with IBE. a) SEM recording of the sidewall of a freestanding diamond structure after crystallographic etch and hard mask stripping. b) Sidewall after 4 min of ion milling at 50 ° incidence from the top surface normal using 500 eV Ar$^+$ ions. c) Sidewall after 14 min of milling with the previous settings. d) Sidewall after 10 min of ion milling at 10 ° incidence from the top surface normal. Due to the high incidence angle with the sidewalls, "steps" are formed. e) Sidewall of a microdisk before IBE treatment. f) Microdisk after 15 min milling at 50 ° and 500 eV. A clean surface before the milling is critical to prevent masking and the formation of protuberances as it is noticeable in figure (c).
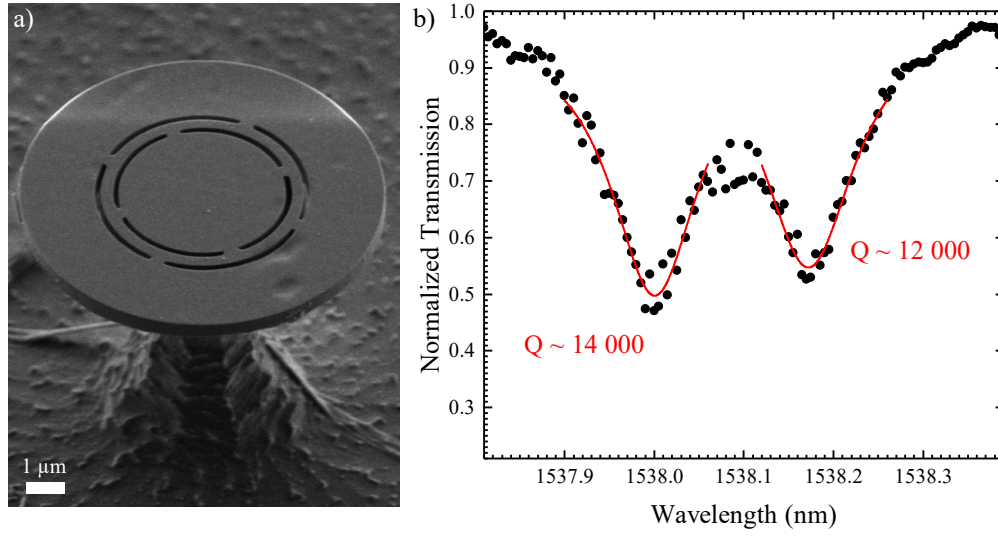
Figure 6.9 – a) Single crystal diamond microring fabricated with recipe UC7. b) Transmission measurement showing optical resonances. The fiber is positioned at the critical coupling for the mode at 1538 nm, and we can measure a quality factor of 1400. The spectrum was obtained by subtracting the fiber transmission (fiber far from resonator) from the raw data (fiber at the critical coupling position).

6.2 Optical transmission characterization

Optical transmission measurement of a diamond microring are shown in figure 6.9. Fitting of the peaks reveals optical quality factors of approximately 14 000. According to optical simulations (figure 4.3), the width of the ring needs to be at least 1.5 µm to avoid scattering from the support tethers. For ring width of less than 1.75 µm typical quality factors are measured in the order of 1000, while rings width of 2 µm can sustain higher Q resonances. If the ring is wider, the undercut may be insufficient, yielding non uniform thickness and thus lower quality factor. The geometry shown in figure 6.9(a) appears to be the sweet spot with the current fabrication strategy. In this case, the quality factor is limited by fabrication defects visible in the top surface and by the smoothness of the bottom surface. We can expect that further optimization of the undercut recipe can improve the bottom surface quality of the wider microrings, ultimately yielding higher optical Q.

Figure 6.10 shows the effect of the sidewall polishing procedure presented in section 6.1.5. The resonances are shifted by several nm, consistent with the reduction of the resonator diameter. According to equation 5.1, the resonance shift is induced by a radius change of about 65 nm. The sidewall polishing step was 15 min long, therefore we can estimate an etch rate of approximately 4.3 nm/min, consistent with the dimensions variation estimated from the SEM images. The optical quality factor improved of more than two times, indicating a reduction of the sidewall scattering, as expected from the SEM recording of figure 6.8. No frequency modulation was measured from the high Q microdisks. The pedestal lateral dimension
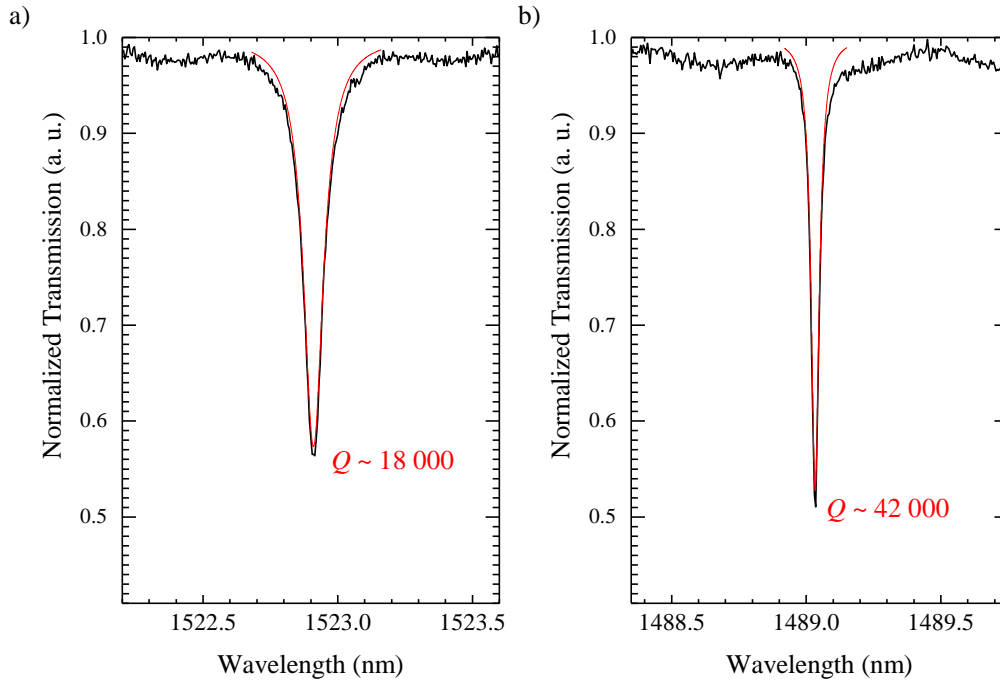
Figure 6.10 – Transmission measurements of 3 µm radius microdisks before (a) and after (b) the sidewall polishing step. The values reported for the quality factors are calculated from a Lorentzian fitting of the resonances. The spectrum was obtained by subtracting the fiber transmission (fiber far from resonator) from the raw data (fiber at the critical coupling position).

at the narrowest point is ~ 1.2 µm. According to COMSOL simulation, the clamping loss limited quality factor should drop below 10^4 when the pedestal approaches these dimensions. However, as reported by Mitchell et al. [184], the pedestal should be particularly narrow (~ 100 nm) to observe the mechanical oscillations.

It should be noted that the before and after spectra were acquired from two different microdisks on the same chip. The two microdisks were patterned starting from the same design using the same exposure dose and current during e-beam lithography, and were patterned 50 µm apart, therefore we can expect them to have very similar optical resonances before the sidewall polishing, both central wavelength and quality factor. We were unable to characterize the same device before and after the polishing because the microdisk of the spectrum in figure 6.10(a) was ruined during the polishing step. As mentioned previously, it is critical to have a clean sample before performing the IBE polishing step to avoid the formation of protuberances during milling. In this case the microdisk was roughened because of dirt on the sidewall, likely deposited by the fiber during the first measurement, and by the presence of particles on the top surface, result of insufficient mask etching or of the exposure to the environment outside the clean room. Dirt and particles mask the diamond surface during milling, resulting in roughness.
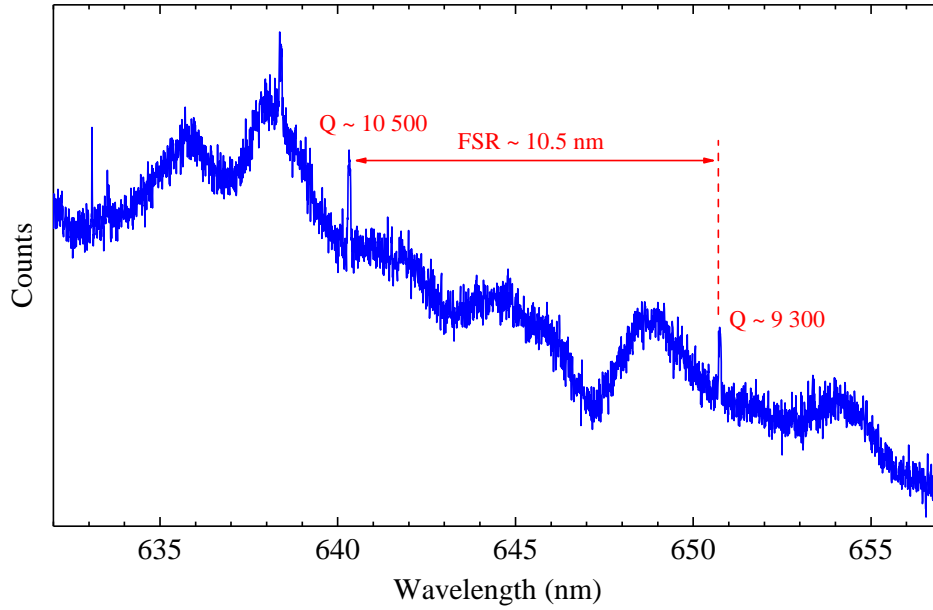
Figure 6.11 – Photoluminescence signal from a 3 µm radius microdisk. The emission from the NV centers in the diamond lattice is enhanced by the optical cavity, revealing optical quality factors of 10^4, obtained by fitting a Lorentzian to the peaks. The emission wavelength of the NV center is at the end of the detection range of the spectrometer which is optimized for UV-blue detection. The longer red signal causes some interference on the detector, observable in the spectrum as oscillations function of the wavelength.

6.3 Photoluminescence

As reported for the FIB milled resonators, photoluminescence spectroscopy was performed. The substrates used in this fabrication method contained some nitrogen defects, therefore photoluminescence could be observed corresponding to the NV defects emission. Using the Ramanscope we could observe the characteristic shape of the NV emission, however given the limited wavelength resolution of the integrated spectroscope, no cavity enhancement of the photoluminescence was observed. Using a custom µ-PL setup with a higher resolution spectroscope revealed optical resonances on top of the NV emission. Figure 6.11 shows the collected spectrum when the pump laser is focused on a 3 µm radius disk. The free spectral range according to equation 2.1 should be 10.5 nm. While we can identify two resonances spaced approximately by this range in the spectrum, the spectrum is not as dense as the one relative to the FIB milled microdisk (figure 5.10). We attribute this to the low detection efficiency of the spectrometer for the red light, as the integrated CCD detector is optimized for UV-blue light. Oscillations are visible in the spectrum at the NV luminescence wavelengths, since the red light interferes in the thinner CCD detector. The collected signal decreases rapidly after 650 nm as the wavelength becomes too long for the detector. Nevertheless, some resonances are visible, and we can measure optical quality factors of 10^4 at 640 nm. The quality factor is calculated from fitting the spectrum peak with a Lorentzian. The spectrum

was acquired with the spectrometer slits not optimized, therefore the real value can be better than the one reported. However, reducing the slit size to increase the wavelength resolution decreased the signal, making the resonance detection more difficult.

6.4   Discussion

This fabrication method demonstrated to be capable of producing resonators with higher optical quality factors compared to the FIB method. The bottom surface is smoother due to the absence of the step, however the undercut recipe can be further optimized to further decrease surface scattering. The optical characterization results are relative to devices fabricated in general grade single crystal plates. Moving to an electronic grade can decrease the optical losses induced by absorption, however, most the impurities present in the general grade substrates (typically nitrogen) absorb predominantly red light, and are transparent to infrared.

Scattering from the sidewalls can be reduced with the sidewall polishing step. Focused Ion Beam milling could be used to remove the outer perimeter of the structures, as we were doing for the FIB structured microresonators. IBE at an appropriate angle however is better suited because it requires less steps (no metal deposition), it can smooth multiple structures in parallel, and it creates negligible lattice damage compared to the high energy gallium beam. As discussed, however, the technique requires to start from a clean sample, as particles and residues can mask the diamond during ion beam milling, increasing the roughness of the structure.

Limited Q_o, of the order of 10^4 and below, were measured for the microrings. As mentioned previously, the etch proceeds primarily from the outer circumference of the microdisk, therefore a long time is required to etch sufficiently the pillar, resulting in insufficient undercut or very thin devices which will be more sensitive to surface scattering. A new design of the resonator geometry is required to take into account the fabrication characteristics. Photonic crystal beams were included in the mask as proof of concept, and the lithography design must be adapted to take into account the size variation induced by the transfer of the pattern into the hard mask and the diamond after the first vertical etch step.

7 Silicon microresonators in the MORPHIC platform

Silicon photonics has become very mature and as a platform it is now routinely used in telecomunications to interface optical links to electronics, thanks to the ability to perform few specific operations very efficiently. While some other material platforms, like lithium niobate or silicon nitride, may be more performant, silicon photonics can benefit from the huge develoment in the material science and processing of CMOS, so that silicon photonics could be fabricated in a CMOS fab [234]. Moreover, foundries started to offer dedicated silicon photonics platforms to serve the growing market. At the current state, however, some important components of a photonic circuit use power consuming designs based on thermo-optic effect or free carrier dispersion [235, 236]. Integrating movable structures can be a viable route to develop power efficient silicon photonics components. One example is the phase shifter: established designs occupy large area and require high power compared to a waveguide movable by electrostatic actuation [237]. Silicon photonic MEMS enable the fabrication of large scale, compact, and efficient switch matrix [238]. The MORPHIC project aim to enhance the functionality of established silicon photonics platform by including MEMS components. In particular, MEMS can be exploited to create reconfigurable photonic integrated circuits, thanks to the development of non-volatile components. The components designed during the project are planned to be included as standard parts of a PDK and as components of a programmable integrated circuit.

Freestanding WGM resonators were included among the test structures of the first fabrication run. Four design variations were implemented: two microrings and two microdisks with different radii. Figure 7.1 shows the mask layout. As previously mentioned in sections 4.1 and 4.2, the smaller resonators have been designed with a radius of 10 µm, and the largest with a radius of 20 µm. The resonators are designed in proximity of a suspended wavegude with different separations, and light is coupled in and out of the sample via grating couplers.
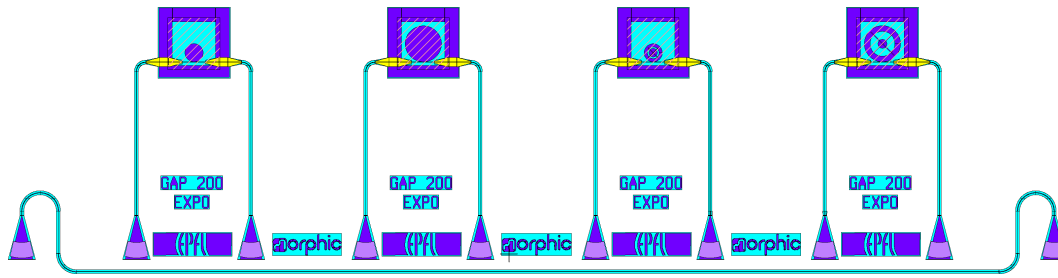
Figure 7.1 – Lithography mask of the WGM resonators.

7.1 MORPHIC MEMS release

Figure 7.2 shows the fabrication process of the silicon microresonators. The mask layout is sent to IMEC for fabrication in the iSiPP50G platform. The resonators are designed in proximity of a waveguide with different gaps ranging form 130 nm to 300 nm. The wafers are received from IMEC and the post-processing is done at CMI. The wafer is separated into coupons. 50 nm of alumina is deposited with atomic layer deposition to achieve good conformal coverage of the entire coupon. It is important to cover also the backside to protect the stress compensation layers from the HF vapor release step. After photolithography, the alumina layer is etched with a $Cl/BCl_3/Ar$ based plasma. The photoresist layer is stripped and the sample is etched in a SPTS uEtch HF vapor etcher to achieve isotropic etching of the buried SiO_2 layer of the SOI coupon. The HF vapor etching ensures that the structures do not collapse since the etching happens entirely in vapor phase, without water condensation beneath the suspended structures. A silicon guard is included in the mask around the structures to prevent excessive etching around the release window.

Due to the different lengths of undercut required to obtain the optimal pillar size in the different resonators, only one resonator geometry can be successfully released for each fabricated chip. From this point of view, microrings are better suited since it is possible to design the central support disk appropriately in order to have the correct support pillar for different external radii. Initial optical characterization showed that the optical resonances with the highest quality factors were supported by the microdisk with radius 10 μm, therefore the undercut process was optimized for the release of these geometry. As a consequence, the undercut was insufficient for the larger microdisks and too long for the microrings. The finalized process achieved a total lateral undercut of ~9 μm. The minimum feature size for the fabrication platform used is 150 nm. When the gap between the waveguide and the resonator is smaller than this value fabrication residues may be present in the gap. Optical quality factor does not appear to be affected by the residue, however it happens when the gap is very narrow, coresponding to a highly overcoupled regime. Critical coupling occurs at around 180 nm separation, when the gap is clear of any residue.
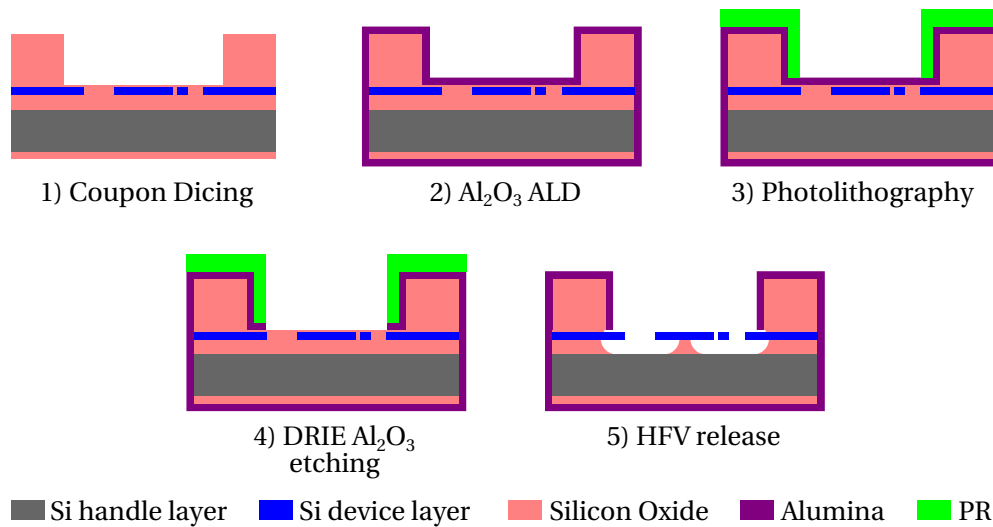
Figure 7.2 – Scheme of the fabrication process to release the silicon photonic MEMS in the MORPHIC platform. 1) Coupons are diced from the wafers received from IMEC. 2) Atomic layer deposition of alumina to protect the backside and the BEOL stack. 3-4) Photolitography and etching of the alumina layer. 5) HF vapor release.
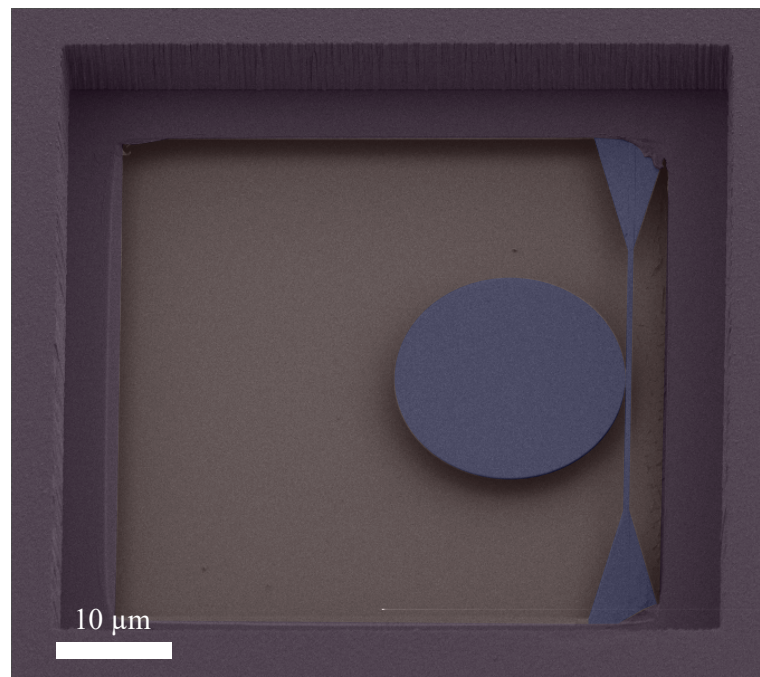
Figure 7.3 – False color SEM recording of a microdisk with radius $10\,\mu m$ after the HFV release step. The pillar diameter is easily measured by increasing the SEM voltage or by imaging with an optical microscope due to the low thickness of the silicon layer. Courtesy of Yuji Takabayashi.
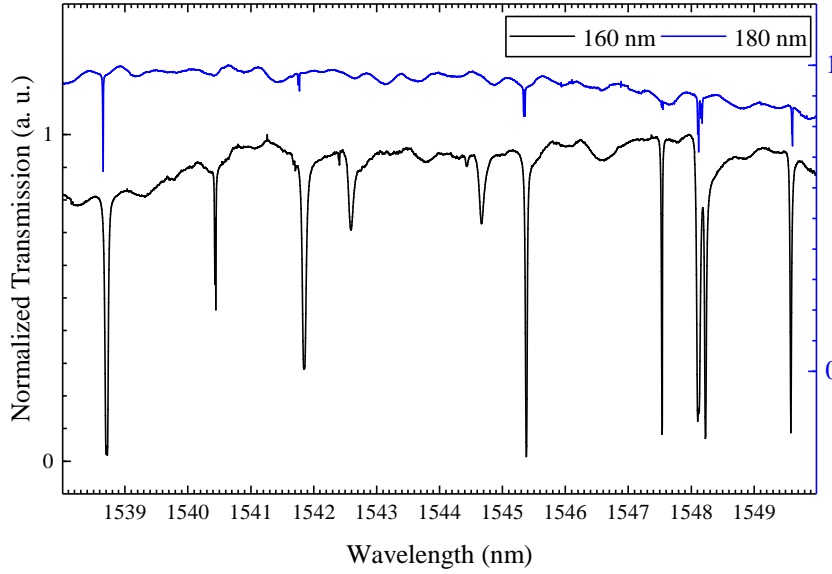
Figure 7.4 – Transmission spectra of a 10 µm radius microdisk at different waveguide gaps. Critical coupling occurs at a separation within the 160 nm to 180 nm. Given the discrete gaps defined by lithogrphy, we cannot probe the resonators in a critical coupling condition. To increase clarity, the the blue spectrum (180 nm gap) is displaced vertically. The right blue vertical axis gives the scale for this spectrum.

7.2 Characterization

The optical characterization is performed by aligning a fiber array to the outer grating couplers (figure 7.1). To know the laser power in the waveguide adjacent to the resonator, it is useful to characterize the losses of the measurement system (figure 4.8). To couple the light in and out of the chip, a fiber array is aligned to an array of grating couplers. The other components used in the optical transmission setup do not contribute substantially to the optical losses, therefore the attenuation of the signal between the laser and the photodetector are attributed to the two grating couplers. Typical losses recorded between the laser and the photodetector are of the order of 14 dB. A lengthy and rigorous alignment can push the losses down to approximately 10 dB. Therefore we can expect the laser signal to be attenuated by 5 to 7 dB before reaching the resonators. The bandwidth of the grating couplers has a maximum at around 1540 nm, and can shift by several nm depending on the thickness of the alumina protection layer used in the postprocessing at CMI and on the angle of the fiber array with the chip surface normal. The bandwidth, however, is large enough to support several FSR even for the smaller resonators (~11 nm). Given the design of the grating coupler, only TE polarization is transmitted to the resonator.

Figure 7.4 shows the transmission spectrum of two 10 µm radius microdisks with different resonator-waveguide gaps, 160 nm and 180 nm. For a gap equal or smaller than 160 nm the resonator is overcoupled. Many resonances are visible in the transmission spectra, corre-
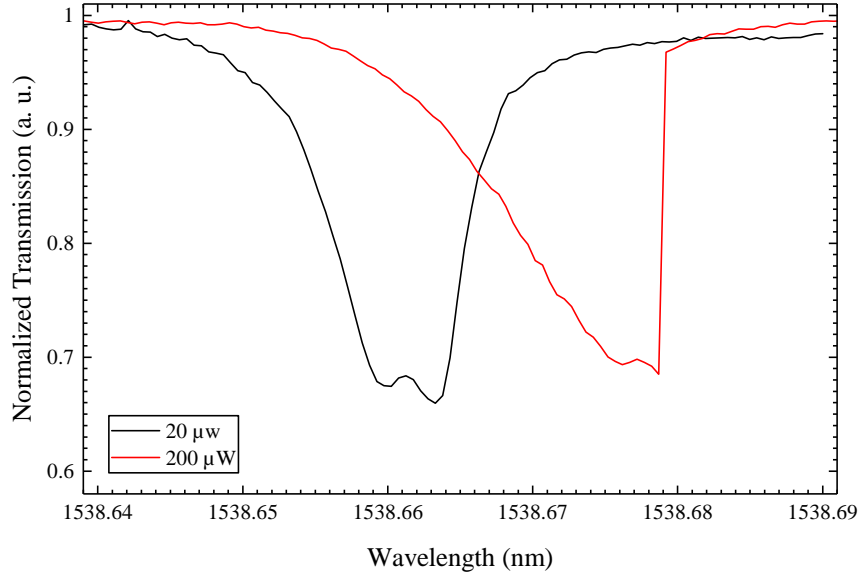
Figure 7.5 – High resolution scan of the optical resonance at 1538.6 nm at approximately 20 μW (black) and 200 μW (red) of laser power in the waveguide (before the resonator). The thermo-optic shift is noticeable when increasing the power, and even at the lowest case the resonance is not symmetric. The measurement shown is for the resonator with 180 nm separation from the waveguide.

sponding to multiple radial orders. For gaps equal to and larger than 180 nm the resonator is undercoupled, and the extinction ratio of the resonances becomes quickly smaller. Critical coupling should occur between 160 nm and 180 nm, but the condition is not accessible due to the discrete gaps defined lithographically. Figure 7.5 shows a high resolution scan of the 1538.6 nm resonance for a resonator with 180 nm separation from the waveguide. The doublet splitting is clearly visible. Fitting a double Lorentzian, we can estimate the optical quality factor of around 300 000 for both the doublets. The measurement is performed by attenuating the laser down to ~20 μW[1] to avoid thermo-optic shift of the resonance. Nevertheless, the resonance is slightly asymmetric even at this very low input power. Gradually increasing the laser power will red-shift the cavity resonance, which can be expressed as [7]

$$\omega(\delta T) = \omega_{LT} \left[1 - \left(\alpha_L + \frac{1}{n_{eff}} \frac{\mathrm{d}n}{\mathrm{d}T} \right) \delta T \right]. \tag{7.1}$$

Following the derivation in [184], and using the appropriate linear expansion parameters, α_L, and refractive index dependence, $\mathrm{d}n / \mathrm{d}T$, [239, 240], we can estimate the effective laser detuning from the central cavity frequency (wavelength). The relationship between the temperature change, δT, and the input power, P_{in}, was estimated by measuring the resonance

---

[1]estimated power in the waveguide after the input grating coupler.
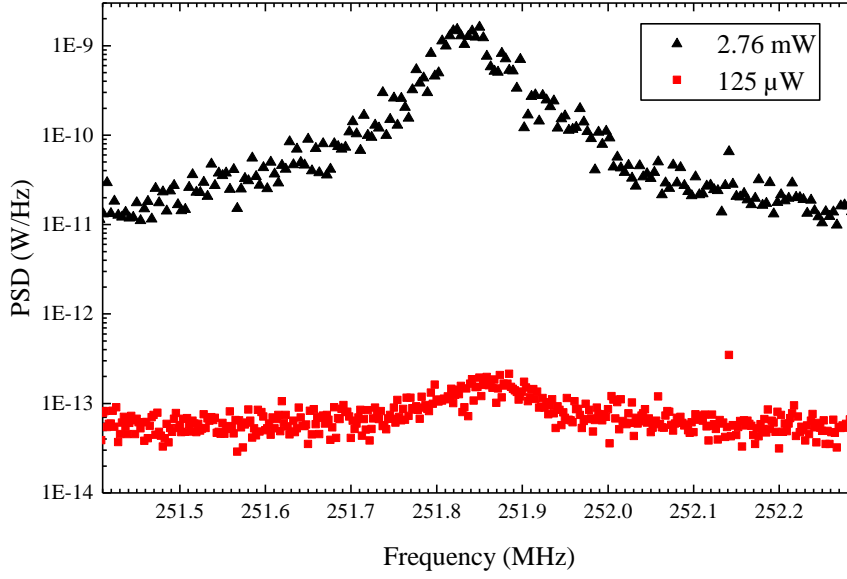
Figure 7.6 – Mechanical spectrum of a 10 μm radius disk with a 1.1 μm radius pillar, corresponding to the RBM. The data reported here was acquired at different optical powers in the waveguide, ~125 μW and ~2.76 mW. By fitting a Lorentzian, the quality factor is estimated to be ~ 1800 and ~ 3600 respectively in air at room temperature. Both measurements are done below the required threshold power. The higher noise floor of the high power measurement is attributed to the EDFA used to amplify the laser signal.

shift at different P_{in}.

7.2.1 Frequency spectrum

To observe the mechanical modulation, the transmitted optical signal was collected with a high speed photodetector and analyzed with an electronic spectrum analyzer (figure 4.9). Given the expected[2] RBM resonance frequency of about 250 MHz, and the measured (loaded) Q_o of about 3×10^5, the optomechanical system operates in the unresolved sideband regime ($\Omega/\kappa \approx 0.4$), therefore we should expect the optimal detuning to be $\Delta \approx \kappa/2$. When the laser wavelength is scanned on the blue side of the resonance, a peak in the frequency spectrum appears at the expected frequency. The peak amplitude increases as the laser wavelength approaches the central cavity resonance, reaching a the maximum when the transmission (DC component) is at half of the dip, corresponding to the optimal detuning. Figure 7.6 shows the RBM modulation measured by the electronic spectrum analyzer for several microdisk with different pillar radii. When the pillar radius is larger than 2 μm, no mechanical modulation is detected by the spectrum analyzer. Finite element simulations predict that the clamping loss limited quality factor drops below 10^3 (figure 4.5). Smaller radii start to support mechanical oscillations that can be detected above the noise floor of our instruments. At 1.7 μm, the

---

[2]From FEM simulations

r_p	$\omega/2\pi$	Q_o	$\Omega/2\pi$	Q_m	m_{eff}	g_{om}
1.7 μm	194.8 THz	80 000	255.5 MHz	500	27 fg	19.5 GHz/nm
1.1 μm	194.8 THz	300 000	251.8 MHz	1800	27 fg	19.5 GHz/nm

Table 7.1 – Characterization of 10 μm radius microdisks with different undercut length. The effective mass was calculated from COMSOL simulations using equation 2.15, and we assumed $g_{om} = \omega/r_d$.

mechanical modulation relative to the RBM supports mechanical quality factors of 500. Reducing the radius further (down to 1.1 μm) allows to support higher Q, measuring $\sim$ 1800 with $P_{in} = 125$ μW. The mechanical oscillation measured with low P_{in} should be predominantly of Brownian nature, as the backaction effect are negligible. Increasing P_{in} results in a clear increase of the mechanical peak amplitude and a reduction of the linewidth, when the laser has the optimal detuning $\Delta \approx \kappa/2$. At $P_{in} = 2.76$ mW, the measured amplitude increases of 4 orders of magnitude, while the quality factor increases to $\sim$ 3600. The narrowing of the resonance indicates that the optomechanical backaction effect starts to increase and it counteracts the intrinsic damping at the selected detuning. As P_{in} increases, the central mechanical frequency shifts towards lower frequencies, caused by the heating and the expansion of the resonator.

Since the resonator is in the unresolved sideband regime, the estimated threshold power required to excite the regenerative oscillations can be expressed as [7]

$$P_{th} \approx \frac{5^3}{2^7} \frac{\Omega}{Q_m} \frac{m_{eff}\omega^4}{g_{om}^2 Q_o^3}. \tag{7.2}$$

Using the values reported in table 7.1, we can estimate the power required to excite the regenerative oscillations to be $P_{th} \approx 5.1$ mW for the best results ($r_p = 1.1$ μm). We did not detect parametric oscillation because of the high power required, which exceeds the maximum output of our tunable laser and requires an EDFA. While power levels of the the order of the expected threshold power could be reached in our system with the help of the fiber amplifier, no parametric oscillation was detected, likely because of an under or overestimations of one of the parameters of table 7.1.

7.2.2 Laser Doppler Vibrometry

Using a laser Doppler vibrometer, we can characterize the out of plane mechanical oscillations of the microresonator. These resonances may not be visible in the frequency spectrum of the transmission signal because of the low optomechanical coupling strength. In fact, given that the moving boundary contribution is negligible for these out of plane oscillations, because the physical cavity length is not affected, and only the photoelastic contribution may have some
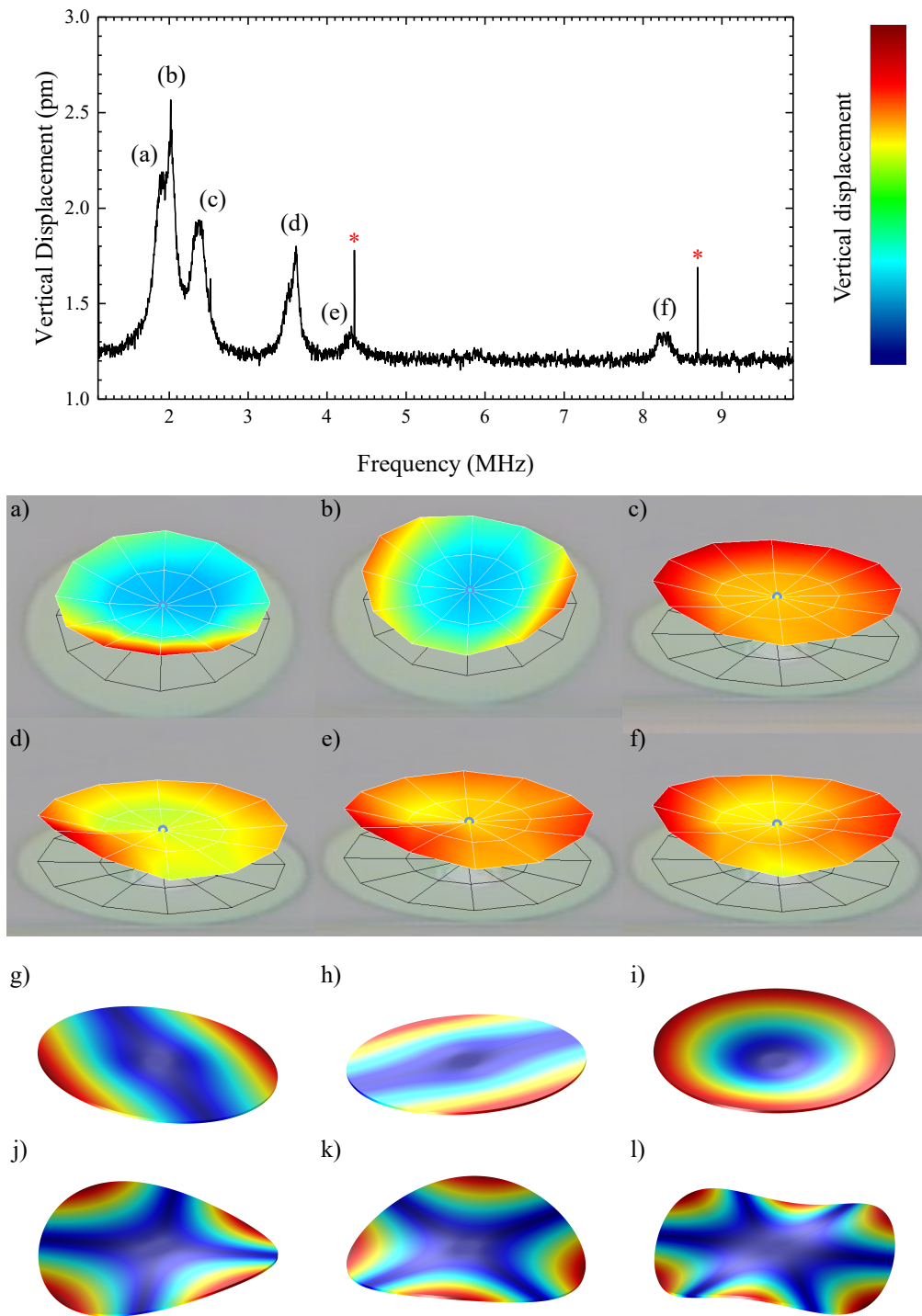
Figure 7.7 – Optical microscope images of a silicon microdisk overlayed with the displacement profile measured by the LDV. The labels (a-f) identify the corresponding peaks in the average displacement spectrum plotted in the graph above. The color scale is normalized to the maximum displacement amplitude (max amplitude = red) of the selected frequency band. g-l) COMSOL eigenfrequency solutions corresponding to the measured resonances (a-f) respectively. The sharp peaks indicated with * do not correspond to any real oscillation modes.

effect.

The LDV used for the caracterization (section 4.4.3) is equipped with a 2D stage and a high magnification objective therefore we can scan the laser spot at different points of the resonator and identify the oscillation modes. Figure 7.7 shows displacement profile measured by the LDV for several modes of a 10 μm radius microdisk. The displacement value for each point of the plot is obtained by selecting the frequency band for each resonance detected in the frequency spectrum. For the plot, the band included the range above the half maximum of the peak to avoid including nearby resonances in the displacement profile plot. However, due to material anisotropy or asymmetry of the structure (e. g. a non centered or elongated support pillar) degenerate resonances may split. In figure 7.7, the splitting is evident for the peaks labelled with (a) and (b), which we can assign to the first order out of plane oscillation (figure 7.7(g-h)). In this case, it is caused by the material anisotropy of single crystal silicon, since the splitting is already predicted by the COMSOL model, which is designed with a well centered circular cross section pillar but using an anisotropic material model for the silicon disk. The mode central frequency is ∼ 20% lower than the numerical solution calculated in COMSOL[3]. The quality factor obtained from fitting the peak in the frequency spectrum is ∼ 50 both for (a) and (b). Spacial accuracy of the 2D stage and the dimension of the laser spot contribute as well to the reduction of the signal-to-noise ratio of the measurement. For these reasons the other displacement profiles are harder to identify, especially higher order modes whose vertical displacement profile varies quickly, requiring a dense scan. However, the corresponding central frequency is consistently ∼ 20% lower than the COMSOL solutions (figure 7.7(i-l)). 20% is a rather high error to attribute only to numerical errors of the simulations. It is possible that the silicon device layer is thinner than expected, as silicon can be etched during the alumina etch step, or due to the device layer variations of different starting substrates, or due to a planarization step used during the fabrication in the foundry. COMSOL simulations with lower thickness (200 nm) show a moderate reduction of the oscillation frequency, converging towards the measured value. Furthermore, as reported in section 4.2, the pillar dimension does influence the oscillation frequency, and the discrepancy between the measurement and the simulations can be due to an error on the pillar size which is measured with an optical microscope. In this case, since a larger pillar will stiffen the structure, we may have overestimated the pillar radius from the microscope images.

No additional resonances that may be attributed to fabrication asymmetries are visible in the spectrum, indicating that the HF vapor undercut process is not influenced by the presence of the suspended waveguide on one side of the resonator and that it can produce a defect free support pillar. One of the strengths of this characterization step is to detect small fabrication defects that may be invisible to other verification steps [207]. The amplitude of the peaks are of the same order of magnitude of the values that can be estimated with equation 2.16 using the values obtained by a COMSOL eigenfrequency simulation, including a penalty factor to

---

[3]The FEM model used takes into account clamping losses only. No viscous damping or squeeze film damping is included in the simulation.

the clamping losses limited quality factor[4]. Higher order modes become increasingly difficult to measure with this technique, since the amplitude is proportional to $\sqrt{\Omega^{-3}}$, therefore we should expect the resonance peaks to fall below the noise floor.

These measurements were performed at ambient pressure, therefore we can expect the damping Γ to be dominated by viscous damping and squeeze film damping. The measured quality factors were 1 order of magnitude smaller the simulated, clamping loss limited, values for the resonances (a-c) and 3 orders of magnitude smaller for the resonances (d-f). The measurement setup is equipped with a small vacuum chamber with a window to perform vibrational measurement in vacuum. Unfortunately, the reduction of the reflected signal coming from the resonator induced by the chamber window reduced the signal below the noise floor.

7.3   Discussion

We demonstrated freestanding high optical quality factor resonators by post-processing foundry chips. This approach is versatile and allows to include freestanding components, other than the freestanding WGM resonators, in a foundry process, while maintaining compatibility with the other processing steps.

We can observe mechanical oscillations with relatively high mechanical quality factors of $\sim 10^3$. Given the ratio between the optical loss rate and the mechanical oscillation frequency, the device operates in an unresolved sideband regime. In this regime, the optomechanical antidamping is dominated by the optical cavity and the required threshold power to excite the self-oscillations is proportional to κ^3. The high optical quality factors of $\sim 10^5$ help reduce the required power to the mW range. The main limitation of the setup is represented by the coupling scheme: typical losses that we can achieve while aligning the fiber array to the grating couplers array are of the order of 6 dB, meaning that the required pump laser power should be $\sim 4\times$ the estimated threshold power. For the devices characterized in section 7.2.1 the required laser power is more than 20 mW (or 50 mW for more common coupling losses achieved during alignment). While this is not an excessive level, it requires the use of an EDFA, which introduces excessive noise in the system.

Since the characterization is performed at ambient pressure, the mechanical damping is strongly limited by viscous damping. While the RBM is much less sensitive to viscous damping compared to other out of plane modes, performing the characterization in vacuum can improve the mechanical quality factor, by 1 order of magnitude typically [7], and reduce proportionally the required threshold power.

---

[4]The penality factor used was $a = 0.01$

8 Analysis of fabrication and results

In this thesis I presented single crystal diamond microresonators fabricated with two different methods, and single crystal silicon microresonators obtained by post-processing foundry chips. The effort was aimed at creating high Qf-product optomechanical resonators, and here I will highlight the advantages and drawbacks of the devices reported in the previous three chapter.

The Focused Ion Beam based method is very versatile and allows for a good control of the shape of the pillar. The introduction of the metal protection layers and of the post-release annealing and cleaning solved three principal problems related to FIB milling: the feature rounding induced by the Gaussian profile of the ion beam; the roughening of sidewall induced by irradiation from a grazing ion beam; and the damage layer induced by high energy Ga^+ ions. The procedure resulted in sharp and smooth sidewalls, with no gallium contamination and no amorphous phase in the diamond lattice. Only photoluminescence from a GR1 defect indicated damage to the diamond lattice. This allowed to measure optical resonances in the infrared with quality factor of up to 5700 at 1492 nm and in the visible with quality factor of up to 3100 at 730 nm. The main limitation to the optical quality factor originates from the alignment of multiple FIB fields that creates a step on the bottom surface, as described in details in section 5.5. To excite the optomechanical self-oscillation, the measured optical quality factors would require several W of optical power dropped in the cavity, which is outside of the capability of the instrumentation of our laboratory (and probably most other laboratories). It should be possible to increase the optical quality factor by improving the fabrication (by reducing the step height to the resolution limit of the instrument) or by using a different resonator geometry (by avoiding aligning multiple FIB fields).

The second process used exploited the etch rate difference of the diamond crystal planes when exposed to an oxygen plasma with zero bias. In contrast with the previous fabrication method, no alignment of multiple patterns is necessary, however it is important to tune the etch recipe to have smooth {100} surfaces and a small pedestal. Most of the effort was aimed at developing this recipe, since every etcher is different and processes presented in literature should be adapted at the equipment available. Initial results showed optical resonances with

Ref.	Substrate	Resonator	Fabrication	λ_c (nm)	Q_o
5.3	Bulk CVD SCD	microdisk	RIE, FIB	1492	5700
6.2	Bulk CVD SCD	microdisk	"quasi-isotropic" undercut	1489	42 000
6.2	Bulk CVD SCD	microring	"quasi-isotropic" undercut	1538	14 000
[176]	Bulk single crystal	microdisk	FIB	627	221
[241]	PCD thin film	microdisk	RIE, FIB sidewall smoothing	~ 1550	~ 100
[186]	PCD thin film	microring	RIE	~ 1550	~ 8500
[177]	H-CVD SCD membrane	1 & 2D photonic crystals	FIB	625	700
[226]	Bulk SCD	1D photonic crystal	RIE, FIB	...	...
[226]	SCD membrane	1D photonic crystal	RIE	567	1700
[242]	SCD membrane	1D photonic crystal	RIE	~ 660	24 000
[173]	Bulk CVD single crystal	racetrack	"angled" RIE	1648	151 000
[173]	Bulk CVD single crystal	1D photonic crystal	"angled" RIE	1609	183 000
[189]	Bulk CVD single crystal	microdisk	"quasi-isotropic" undercut	1540	335 000

Table 8.1 – Comparison of the characterization results of Q_o for the FIB milled microdisk (sec. 5.3), the crystallographically etched microdisk (sec. 6.2), with other results reported in literature. H-CVD, heteroepitaxial CVD thin film.
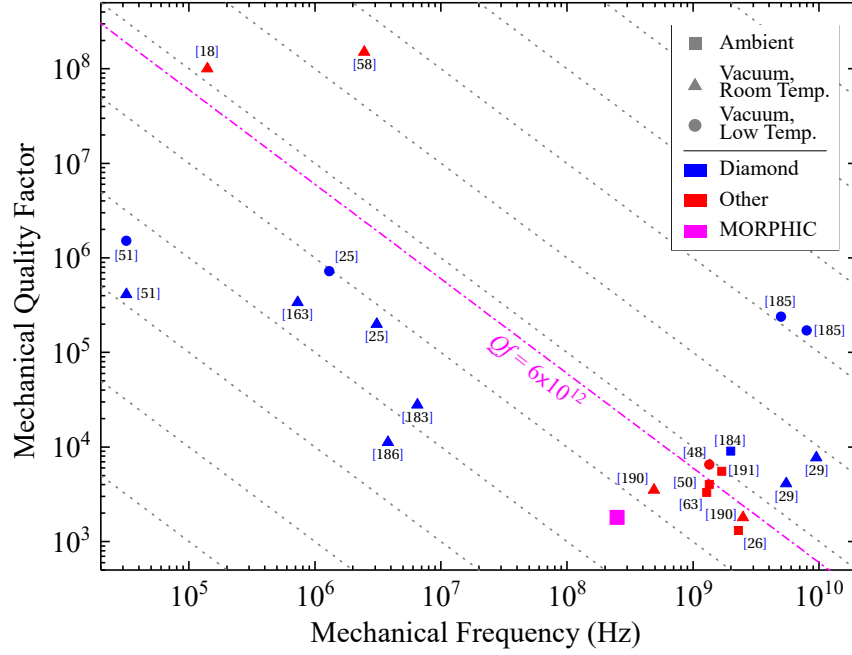
Figure 8.1 – *Qf*-product plot of the reported examples of diamond mechanical and optomechanical resonators (blue) compared to other high *Qf* systems (red), updated with the silicon resonators results (magenta square).

quality factor moderately better than the FIB-milled microdisks. Given that the optical quality factor is strongly influenced by the sidewall roughness, we investigated a method to polish the sidewall. It is based on ion beam milling, as described in section 6.1.5. The process was successful in reducing the roughness created during the vertical etch step. We measured optical quality factors of 42 000 at 1489 nm. A comparison of the optical characterization results achieved in the diamond resonators is reported in table 8.1. Some examples from literature are listed as well. The second method is capable of achieving much higher quality factors, with examples going up to 335 000 reported in literature. In our case the optimization of the crystallographic etch is the limiting factor, but we can expect to achieve high Q within few additional optimization cycles.

As expected, optical resonances measured in the silicon microresonators have much higher quality factors, being fabricated with an established foundry process at IMEC. After the post-processing steps done at the EPFL clean room, we can reliably measure optical quality factors better than 100 000 at ~1550 nm, with some resonances measuring up to ~300 000. Mechanical oscillations from the radial breathing modes are measured with a central frequency of 252 MHz and a quality factor of 1800, for the Brownian regime, yielding a *Qf*-product of 4.5×10^{11}. In figure 8.1 the *Qf*-product plot, previously reported in figure 3.4, has been updated indicating the results of chapter 7. No mechanical oscillation has been measured for the crystallographically etched microresonators, however as discussed in section 6.4, the improve-

ments to include in the process are clear and can be easily integrated in future fabrication runs.

9 Conclusions and outlook

In this manuscript I presented the fabrication and characterization of freestanding single crystal microresonators. The work was focused mostly on single crystal diamond microresonators, but also single crystal silicon structures were investigated. The primary focus was the realization of optomechanical resonators, to be used, as a target application, as low phase noise frequency reference. The practical work involved establishing fabrication processes within the group to structure single crystal diamond, as well as the design of characterization setups.

The chapters 5, 6, and 7 presenting the results are listed in a chronological order. The first fabrication strategy I worked on is the 3D milled microresonators. When I started at the end of 2015, there was no demonstration of cavity optomechanics in structured fabricated in bulk single crystal diamond. The 3D FIB fabrication was aimed at developing microdisks resonators with sufficiently high optical quality factors to excite the self-oscillation at low threshold power, and, most importantly, to have good control on the pedestal shape to minimize the mechanical dissipation induced by the clamping losses. Several extra fabrication steps were included to deal with the typical problems associated with FIB milling. These steps were successful in eliminating feature rounding, caused by the Gaussian profile of the ion beam, sidewall roughening, caused by ion irradiation at grazing angles, and the FIB-induced damage, caused by the implantation and the recoil of the ions in the diamond lattice. This contributed in demonstrating optical cavities with the highest optical quality factor among the single crystal diamond cavities which fabrication involved some form of FIB milling. Further improvements of the fabrication could improve the optical quality factors beyond the measured 5700 at telecom wavelengths, however we would need to put a lot of effort to achieve alignments down to the resolution limit of the machine. Changing the resonator geometry can prevent the need for alignment, for example by designing a photonic crystal beam. This design however is particularly sensitive to fabrication imperfections and a similar fabrication strategy was reported in literature before with limited optical quality.

The crystallographically etched microresonators have, arguably, the best potential to be used successfully as low phase noise optomechanical oscillators. The technique has already a

number of demonstration in literature, and it allows to create many resonators in parallel, and it can work for different geometries. The fabrication procedure is based on using a zero bias oxygen plasma to attack the different crystal planes of the diamond lattice at different speed. The resulting structures will be suspended on a hourglass pillar, with octagonal or square cross section. Given the shape of the pillar, it is important that the lateral undercut is long enough to avoid the perturbation of the optical mode due to the not azimuthal symmetry of the pillar, and to avoid excessive clamping losses of the mechanical oscillation. This step is critical and it would benefit greatly from a plasma etcher specifically designed for the task. Most commercial etchers are not designed to operate in these conditions (high ICP power and zero bias), therefore it is very challenging to obtain a purely crystallographic etch. The concentric, low dissipation microring design was developed with the aim to relax the geometrical requirements of the support pedestal. For the microdisks, in fact, it is very important to minimize the lateral dimension of the pillar to prevent excessive clamping losses. The microrings should be very insensitive to the dimensions of the pillar and the thickness of the supports, provided that the undercut is sufficient to not disrupt the optical mode. Further optimization of the undercut recipe is required, as the measured optical quality factors are limited to 14 000 at telecom wavelengths in the microrings we fabricated. Microdisks showed an increase of the optical quality factor up to 42 000 at telecom wavelengths compared to the FIB milled microresonators. The high optical quality factor was achieved thanks to a sidewall polishing step that is based on low energy ion beam milling. The technique is promising to be used to polish the sidewalls of other microstructures in other materials. Is is better suited to hard and brittle materials like single crystal diamond because of the slow etch rate allowing finer control of the procedure and to limit the geometry variation from the original design.

Unsurprisingly, the best optical results were achieved in the single crystal silicon microresonators, since the devices were fabricated starting from foundry chips. Optical quality factors of up to 300 000 were measured at telecom wavelengths. Mechanical modulation of the optical signal was measured, revealing radial breathing modes with mechanical quality factors of 1800 at 250 MHz. The required threshold power was higher that what we could supply, therefore no self oscillation was observed. The main limiting factor was the coupling losses of the grating couplers, attenuating substantially the laser power. To reduce the threshold power, different things can be improved in further iterations. Since the device operates in the unresolved sideband regime, improving the optical quality factor will have the largest impact on the threshold power. Since most of the fabrication is performed in a foundry, we have control only on the undercut steps. The quality of the surface can be improved, yielding higher Q_o, by different wet etching treatments. Since there are other suspended structures on the chip however, the risk of stiction is high making this route not ideal. Alternatively we could include smaller structures in the mask design to access the resolved sideband regime, in which the threshold power will be smaller than the unresolved sideband regime for comparable optical quality factors. Finally, we could perform the measurements in vacuum, as it should improve the mechanical quality factor of at least one order of magnitude by decreasing the the viscous damping. However, if the device will be used as a sensor or frequency reference in

an integrated photonic circuit, vacuum operation may not be a viable option, therefore the only possible options to reduce the required threshold power is to increase the optical quality factor or to use a smaller disk to operate in a resolved sideband regime.

While the diamond fabrication method based on the crystallographic etch allows some form of parallelism by processing multiple resonators on a chip and eventually multiple chips in parallel, potential applications will be limited to the laboratory due to the need to align external tapered fibers to interface the resonator. While grating couplers are less efficient than a tapered fiber, the packaging of the device is significantly easier. To move further, development of substrates will be necessary, eventually to match what is currently available on silicon by creating a diamond on insulator platform. This would allow the use of the fabrication routines developed over the years for silicon devices and the inclusion of networks of waveguides which can interface with external source/detectors with arrays of (grating) couplers.

Bibliography

1. *Cavity Optomechanics* (eds Aspelmeyer, M., Kippenberg, T. J., Marquardt, F.) (Springer Berlin Heidelberg, Berlin, Heidelberg, 2014).

2. Spillane, S. M. *Fiber-Coupled Ultra-High-Q Microresonators for Nonlinear and Quantum Optics* (California Institute of Technology, 2004).

3. Borselli, M. *High-Q Microresonators as Lasing Elements for Silicon Photonics* (California Institute of Technology, 2006).

4. Anetsberger, G. *Novel Cavity Optomechanical Systems at the Micro- and Nanoscale and Quantum Measurements of Nanomechanical Oscillators* (Ludwig-Maximilians-Universitat Munchen, 2010).

5. Chan, J. *Laser Cooling of an Optomechanical Crystal Resonator to Its Quantum Ground State of Motion* (California Institute of Technology, 2012).

6. Safavi-Naeini, A. H. *Quantum Optomechanics with Silicon Nanostructures* (California Institute of Technology, 2013).

7. Grutter, K. *Optical Whispering-Gallery Mode Resonators for Applications in Optical Communication and Frequency Control* (EECS Department, University of California, Berkeley, Dec. 2013).

8. Burek, M. J. *Free-Standing Nanomechanical and Nanophotonic Structures in Single-Crystal Diamond* (Harvard University, 2016).

9. Khanaliloo, B. *Optomechanical Devices in Single Crystal Diamond* (University of Calgary, 2017).

10. Braginskiĭ, V. B., Manukin, A. B. "Ponderomotive Effects of Electromagnetic Radiation". *Soviet Journal of Experimental and Theoretical Physics* **25,** 653 (Oct. 1967).

11. Braginskiĭ, V. B., Vorontsov, Y. I. "Quantum-Mechanical Limitations in Macroscopic Experiments and Modern Experimental Technique". *Soviet Physics Uspekhi* **17,** 644–650 (May 1975).

12. Braginskiĭ, V. B., Manukin, A. B. *Measurement of Weak Forces in Physics Experiments* (University of Chicago Press, Chicago, 1977).

13. Abramovici, A. *et al.* "LIGO: The Laser Interferometer Gravitational-Wave Observatory". *Science* **256,** 325–333 (1992).

14. Harry, G. M. "Advanced LIGO: The next Generation of Gravitational Wave Detectors". *Classical and Quantum Gravity* **27,** 084006 (Apr. 2010).

15. Acernese, F *et al.* "Advanced Virgo: A Second-Generation Interferometric Gravitational Wave Detector". *Classical and Quantum Gravity* **32,** 024001 (Jan. 22, 2015).

16. Gigan, S. *et al.* "Self-Cooling of a Micromirror by Radiation Pressure". *Nature* **444,** 67–70 (Nov. 1, 2006).

17. Thompson, J. D. *et al.* "Strong Dispersive Coupling of a High-Finesse Cavity to a Micromechanical Membrane". *Nature* **452,** 72 (Mar. 6, 2008).

18. Norte, R. A., Moura, J. P., Gröblacher, S. "Mechanical Resonators for Quantum Optomechanics Experiments at Room Temperature". *Physical Review Letters* **116** (Apr. 5, 2016).

Bibliography

19. Moura, J. P., Norte, R. A., Guo, J., Schäfermeier, C., Gröblacher, S. "Centimeter-Scale Suspended Photonic Crystal Mirrors". *Opt. Express* **26,** 1895–1909 (Jan. 2018).

20. Armani, D. K., Kippenberg, T. J., Spillane, S. M., Vahala, K. J. "Ultra-High-Q Toroid Microcavity on a Chip". *Nature* **421,** 925–928 (Feb. 2003).

21. Rokhsari, H, Kippenberg, T. J., Carmon, T, Vahala, K. J. "Radiation-Pressure-Driven Micro-Mechanical Oscillator", 9 (2005).

22. Anetsberger, G., Rivière, R., Schliesser, A., Arcizet, O., Kippenberg, T. J. "Ultralow-Dissipation Optomechanical Resonators on a Chip". *Nature Photonics* **2,** 627–633 (Oct. 2008).

23. Ding, L. *et al.* "High Frequency GaAs Nano-Optomechanical Disk Resonator". *Phys. Rev. Lett.* **105,** 263903 (Dec. 2010).

24. Pernice, W. H. P., Li, M., Tang, H. X. "Optomechanical Coupling in Photonic Crystal Supported Nanomechanical Waveguides". *Opt. Express* **17,** 12424–12432 (July 2009).

25. Khanaliloo, B. *et al.* "Single-Crystal Diamond Nanobeam Waveguide Optomechanics". *Physical Review X* **5** (Dec. 29, 2015).

26. Eichenfield, M., Chan, J., Camacho, R. M., Vahala, K. J., Painter, O. "Optomechanical Crystals". *Nature* **462,** 78–82 (Nov. 2009).

27. Chan, J., Safavi-Naeini, A. H., Hill, J. T., Meenehan, S., Painter, O. "Optimized Optomechanical Crystal Cavity with Acoustic Radiation Shield". *Applied Physics Letters* **101,** 081115 (Aug. 20, 2012).

28. Makles, K. *et al.* "2D Photonic-Crystal Optomechanical Nanoresonator". *Opt. Lett.* **40,** 174–177 (Jan. 2015).

29. Burek, M. J. *et al.* "Diamond Optomechanical Crystals". *Optica* **3,** 1404 (Dec. 20, 2016).

30. Favero, I. *et al.* "Fluctuating Nanomechanical System in a High Finesse Optical Microcavity". *Opt. Express* **17,** 12813–12820 (July 2009).

31. Purdy, T. P. *et al.* "Tunable Cavity Optomechanics with Ultracold Atoms". *Phys. Rev. Lett.* **105,** 133602 (Sept. 2010).

32. Purcell, E. M. "Spontaneous Emission Probabilities at Radio Frequencies". *Physical Review* **69,** 681 (1946).

33. Weiss, D. S. *et al.* "Splitting of High-Q Mie Modes Induced by Light Backscattering in Silica Microspheres". *Optics Letters* **20,** 1835 (Sept. 15, 1995).

34. Kippenberg, T. J., Spillane, S. M., Vahala, K. J. "Modal Coupling in Traveling-Wave Resonators". *Optics Letters* **27,** 1669 (Oct. 1, 2002).

35. Bing-Jing Li, Pao-Lo Liu. "Analysis of Far-Field Patterns of Microdisk Resonators by the Finite-Difference Time-Domain Method". *IEEE Journal of Quantum Electronics* **33,** 1489–1491 (Sept./1997).

36. Peter, E. *et al.* "Highly Directional Radiation Pattern of Microdisk Cavities". *Applied Physics Letters* **91,** 151103 (Oct. 8, 2007).

37. Cai, M., Painter, O., Vahala, K. J. "Observation of Critical Coupling in a Fiber Taper to a Silica-Microsphere Whispering-Gallery Mode System". *Phys. Rev. Lett.* **85,** 74–77 (July 2000).

38. Villatoro, J., Monzón-Hernández, D., Mejía, E. "Fabrication and Modeling of Uniform-Waist Single-Mode Tapered Optical Fiber Sensors". *Applied Optics* **42,** 2278 (May 1, 2003).

39. Spillane, S. M., Kippenberg, T. J., Painter, O. J., Vahala, K. J. "Ideality in a Fiber-Taper-Coupled Microresonator System for Application to Cavity Quantum Electrodynamics". *Physical Review Letters* **91** (July 22, 2003).

40. Barclay, P. E., Srinivasan, K., Borselli, M., Painter, O. "Probing the Dispersive and Spatial Properties of Planar Photonic Crystal Waveguide Modes via Highly Efficient Coupling from Optical Fiber Tapers". *Applied Physics Letters* **85,** 4–6 (July 5, 2004).

41. Borselli, M., Srinivasan, K., Barclay, P. E., Painter, O. "Rayleigh Scattering, Mode Coupling, and Optical Loss in Silicon Microdisks". *Applied Physics Letters* **85,** 3693–3695 (Oct. 25, 2004).

42. Grillet, C., Bian, S. N., Magi, E. C., Eggleton, B. J. "Fiber Taper Coupling to Chalcogenide Microsphere Modes". *Appl. Phys. Lett.* 4.

43. Rivière, R., Arcizet, O., Schliesser, A., Kippenberg, T. J. "Evanescent Straight Tapered-Fiber Coupling of Ultra-High Q Optomechanical Micro-Resonators in a Low-Vibration Helium-4 Exchange-Gas Cryostat". *Review of Scientific Instruments* **84,** 043108 (Apr. 2013).

44. Yariv, A. "Universal Relations for Coupling of Optical Power between Microresonators and Dielectric Waveguides". *Electronics Letters* **36,** 321 (2000).

45. Gorodetsky, M., Ilchenko, V. "High-Q Optical Whispering-Gallery Microresonators: Precession Approach for Spherical Mode Analysis and Emission Patterns with Prism Couplers". *Optics Communications* **113,** 133–143 (1994).

46. Jing Wang, Butler, J., Feygelson, T., Nguyen, C.-C. *1.51-GHz Nanocrystalline Diamond Micromechanical Disk Resonator with Material-Mismatched Isolating Support.* in *17th IEEE International Conference on Micro Electro Mechanical Systems. Maastricht MEMS 2004 Technical Digest* 17th IEEE International Conference on Micro Electro Mechanical Systems. Maastricht MEMS 2004 Technical Digest (IEEE, Maastricht, Netherlands, 2004), 641–644.

47. Lin, Q. *et al.* "Coherent Mixing of Mechanical Excitations in Nano-Optomechanical Structures". *Nature Photonics* (Feb. 7, 2010).

48. Nguyen, D. T. *et al.* "Ultrahigh Q-Frequency Product for Optomechanical Disk Resonators with a Mechanical Shield". *Applied Physics Letters* **103,** 241112 (Dec. 9, 2013).

49. Wilson-Rae, I. "Intrinsic Dissipation in Nanomechanical Resonators Due to Phonon Tunneling". *Phys. Rev. B* **77,** 245418 (June 2008).

50. Sun, X., Fong, K. Y., Xiong, C., Pernice, W. H. P., Tang, H. X. "GHz Optomechanical Resonators with High Mechanical Q Factor in Air". *Optics Express* **19,** 22316 (Oct. 24, 2011).

51. Tao, Y., Boss, J. M., Moores, B. A., Degen, C. L. "Single-Crystal Diamond Nanomechanical Resonators with Quality Factors Exceeding One Million". *Nature Communications* **5** (Apr. 8, 2014).

52. Hyun Kim, K. *et al.* "Cavity Optomechanics on a Microfluidic Resonator with Water and Viscous Liquids". *Light: Science & Applications* **2,** e110–e110 (Nov. 2013).

53. Gil-Santos, E. *et al.* "High-Frequency Nano-Optomechanical Disk Resonators in Liquids". *Nature Nanotechnology* **10,** 810–816 (Sept. 2015).

54. Zener, C. "Internal Friction in Solids II. General Theory of Thermoelastic Internal Friction". *Physical Review* **53,** 90–99 (Jan. 1, 1938).

55. Roszhart, T. V. *The Effect of Thermoelastic Internal Friction on the Q of Micromachined Silicon Resonators.* in *IEEE 4th Technical Digest on Solid-State Sensor and Actuator Workshop* ISSN: (June 1990), 13–16.

56. Yasumura, K. *et al.* "Quality Factors in Micron- and Submicron-Thick Cantilevers". *Journal of Microelectromechanical Systems* **9,** 117–125 (Mar. 2000).

57. Adiga, V. P. *et al.* "Mechanical Stiffness and Dissipation in Ultrananocrystalline Diamond Microresonators". *Physical Review B* **79** (June 2, 2009).

58. Ghadimi, A. H. *et al.* "Elastic Strain Engineering for Ultralow Mechanical Dissipation". *Science* **360,** 764–768 (2018).

59. Seoánez, C., Guinea, F., Castro Neto, A. H. "Surface Dissipation in Nanoelectromechanical Systems: Unified Description with the Standard Tunneling Model and Effects of Metallic Electrodes". *Phys. Rev. B* **77,** 125107 (Mar. 2008).

60. Nguyen, C. "MEMS Technology for Timing and Frequency Control". *IEEE Transactions on Ultrasonics, Ferroelectrics and Frequency Control* **54,** 251–270 (2007).

61. Aspelmeyer, M., Kippenberg, T. J., Marquardt, F. "Cavity Optomechanics". *Reviews of Modern Physics* **86,** 1391–1452 (Dec. 30, 2014).

Bibliography

62. Cleland, A. N. *Foundations of Nanomechanics : From Solid-State Theory to Device Applications* (Springer, Berlin, 2003).

63. Jiang, W. C., Lu, X., Zhang, J., Lin, Q. "High-Frequency Silicon Optomechanical Oscillator with an Ultralow Threshold". *Optics Express* **20,** 15991–15996 (2012).

64. Balram, K. C., Davanço, M., Srinivasan, K. *Moving Boundary and Photoelastic Contributions to Optomechanical Coupling in GaAs Microcavities.* in *2014 IEEE Photonics Conference* (Oct. 2014), 338–339.

65. Johnson, S. G. *et al.* "Perturbation Theory for Maxwell's Equations with Shifting Material Boundaries". *Phys. Rev. E* **65,** 066611 (June 2002).

66. Hounsome, L. S., Jones, R., Shaw, M. J., Briddon, P. R. "Photoelastic Constants in Diamond and Silicon". *physica status solidi (a)* **203,** 3088–3093 (Sept. 2006).

67. Braginsky, V., Strigin, S., Vyatchanin, S. "Parametric Oscillatory Instability in Fabry–Perot Interferometer". *Physics Letters A* **287,** 331–338 (Sept. 2001).

68. Vahala, K. J. "Back-Action Limit of Linewidth in an Optomechanical Oscillator". *Phys. Rev. A* **78,** 023832 (Aug. 2008).

69. Tallur, S., Sridaran, S., Bhave, S. A. "A Monolithic Radiation-Pressure Driven, Low Phase Noise Silicon Nitride Opto-Mechanical Oscillator". *Optics Express* **19,** 24522 (Nov. 21, 2011).

70. Schliesser, A., Del'Haye, P., Nooshi, N., Vahala, K. J., Kippenberg, T. J. "Radiation Pressure Cooling of a Micromechanical Oscillator Using Dynamical Backaction". *Physical Review Letters* **97** (Dec. 14, 2006).

71. Chan, J. *et al.* "Laser Cooling of a Nanomechanical Oscillator into Its Quantum Ground State". *Nature* **478,** 89–92 (Oct. 5, 2011).

72. Carmon, T., Yang, L., Vahala, K. J. "Dynamical Thermal Behavior and Thermal Self-Stability of Microcavities". *Opt. Express* **12,** 4742–4750 (Oct. 2004).

73. Liu, Y., Davanço, M., Aksyuk, V., Srinivasan, K. "Electromagnetically Induced Transparency and Wideband Wavelength Conversion in Silicon Nitride Microdisk Optomechanical Resonators". *Physical Review Letters* **110** (May 31, 2013).

74. Weis, S. *et al.* "Optomechanically Induced Transparency". *Science* **330,** 1520–1523 (Dec. 10, 2010).

75. Safavi-Naeini, A. H. *et al.* "Electromagnetically Induced Transparency and Slow Light with Optomechanics". *Nature* **472,** 69–73 (Apr. 2011).

76. Hill, J. T., Safavi-Naeini, A. H., Chan, J., Painter, O. "Coherent Optical Wavelength Conversion via Cavity Optomechanics". *Nature Communications* **3,** 1196 (Nov. 13, 2012).

77. Safavi-Naeini, A. H. *et al.* "Squeezed Light from a Silicon Micromechanical Resonator". *Nature* **500,** 185–189 (Aug. 7, 2013).

78. Verlot, P., Tavernarakis, A., Briant, T., Cohadon, P.-F., Heidmann, A. "Backaction Amplification and Quantum Limits in Optomechanical Measurements". *Phys. Rev. Lett.* **104,** 133602 (Mar. 2010).

79. Hoff, U. B. *et al.* "Quantum-Enhanced Micromechanical Displacement Sensitivity". *Opt. Lett.* **38,** 1413–1415 (May 2013).

80. Krause, A. G., Winger, M., Blasius, T. D., Lin, Q., Painter, O. "A High-Resolution Microchip Optomechanical Accelerometer". *Nature Photonics* **6,** 768–772 (Oct. 14, 2012).

81. Liu, F., Alaie, S., Leseman, Z. C., Hossein-Zadeh, M. "Sub-Pg Mass Sensing and Measurement with an Optomechanical Oscillator". *Optics Express* **21,** 19555 (Aug. 26, 2013).

82. Yu, W., Jiang, W. C., Lin, Q., Lu, T. "Cavity Optomechanical Spring Sensing of Single Molecules". *Nature Communications* **7** (Nov. 2016).

83. Rocheleau, T. O. *et al. Enhancement of Mechanical Q for Low Phase Noise Optomechanical Oscillators.* in *Micro Electro Mechanical Systems (MEMS), 2013 IEEE 26th International Conference On* (IEEE, 2013), 118–121.

84. Grine, A. J. *et al. Phase Noise Spectrum and Carrier Power Modeling of High Performance Optomechanical Oscillators*. in *Lasers and Electro-Optics (CLEO), 2013 Conference On* (IEEE, 2013), 1–2.

85. Metcalfe, M. "Applications of Cavity Optomechanics". *Applied Physics Reviews* **1,** 031105 (Sept. 2014).

86. Polikarpov, M., Polikarpov, V., Snigireva, I., Snigirev, A. "Diamond X-Ray Refractive Lenses with High Acceptance". *Physics Procedia* **84,** 213–220 (2016).

87. Woerner, E., Wild, C., Mueller-Sebert, W., Koidl, P. "CVD-Diamond Optical Lenses". *Diamond and Related Materials* **10,** 557–560 (Mar. 2001).

88. Zhu, T.-F. *et al.* "Fabrication of Diamond Microlenses by Chemical Reflow Method". *Optics Express* **25,** 1185 (Jan. 2017).

89. Liu, H. *et al.* "Large Radius of Curvature Micro-Lenses on Single Crystal Diamond for Application in Monolithic Diamond Raman Lasers". *Diamond and Related Materials* **65,** 37–41 (May 2016).

90. Forsberg, P., Karlsson, M. "High Aspect Ratio Optical Gratings in Diamond". *Diamond and Related Materials* **34,** 19–24 (Apr. 2013).

91. Makita, M. *et al.* "Fabrication of Diamond Diffraction Gratings for Experiments with Intense Hard X-Rays". *Microelectronic Engineering* **176,** 75–78 (May 2017).

92. Stepanov, A. L. *et al.* "A Diffraction Grating Created in Diamond Substrate by Boron Ion Implantation". *Technical Physics Letters* **43,** 104–106 (Jan. 2017).

93. Mildren, R. P., Sabella, A. "Highly Efficient Diamond Raman Laser". *Optics Letters* **34,** 2811 (Sept. 15, 2009).

94. Sabella, A., Piper, J. A., Mildren, R. P. "1240 Nm Diamond Raman Laser Operating near the Quantum Limit". *Optics Letters* **35,** 3874 (Dec. 1, 2010).

95. Latawiec, P. *et al.* "On-Chip Diamond Raman Laser". *Optica* **2,** 924 (Nov. 20, 2015).

96. Feve, J.-P. M., Shortoff, K. E., Bohn, M. J., Brasseur, J. K. "High Average Power Diamond Raman Laser". *Optics Express* **19,** 913 (Jan. 17, 2011).

97. Hess, P. "The Mechanical Properties of Various Chemical Vapor Deposition Diamond Structures Compared to the Ideal Single Crystal". *Journal of Applied Physics* **111,** 051101 (Mar. 2012).

98. Butler, J. E., Sumant, A. V. "The CVD of Nanodiamond Materials". *Chemical Vapor Deposition* **14,** 145–160 (July 2008).

99. Hopcroft, M. A., Nix, W. D., Kenny, T. W. "What Is the Young's Modulus of Silicon?" *Journal of Microelectromechanical Systems* **19,** 229–238 (Apr. 2010).

100. Bhushan, B., Li, X. "Micromechanical and Tribological Characterization of Doped Single-Crystal Silicon and Polysilicon Films for Microelectromechanical Systems Devices". *Journal of Materials Research* **12,** 54–63 (Jan. 1997).

101. Rath, P., Ummethala, S., Nebel, C., Pernice, W. H. P. "Diamond as a Material for Monolithically Integrated Optical and Optomechanical Devices: Diamond as a Material for Integrated Optical and Optomechanical Devices". *physica status solidi (a)* **212,** 2385–2399 (Nov. 2015).

102. Okada, Y., Tokumaru, Y. "Precise Determination of Lattice Parameter and Thermal Expansion Coefficient of Silicon between 300 and 1500 K". *Journal of Applied Physics* **56,** 314–320 (July 15, 1984).

103. Parker, J. H., Feldman, D. W., Ashkin, M. "Raman Scattering by Silicon and Germanium". *Physical Review* **155,** 712–714 (Mar. 15, 1967).

104. Eaton-Magaña, S., Shigley, J. E., Breeding, C. M. "OBSERVATIONS ON HPHT-GROWN SYNTHETIC DIAMONDS: A REVIEW." *Gems & Gemology* **53** (2017).

105. Yan, C.-s., Vohra, Y. K., Mao, H.-k., Hemley, R. J. "Very High Growth Rate Chemical Vapor Deposition of Single-Crystal Diamond". *Proceedings of the National Academy of Sciences* **99,** 12523–12525 (Oct. 1, 2002).

106. Wang, W. *et al.* "CVD Synthetic Diamonds from Gemesis Corp." *Gems & Gemology* **48** (2012).

107. Okushi, H. "High Quality Homoepitaxial CVD Diamond for Electronic Devices". *Diamond and Related Materials. 11th European Conference on Diamond, Diamond-like Materials, Carbon Nanotubes, Nitrides and Silicon Carbide* **10,** 281–288 (Mar. 1, 2001).

108. Badzian, A., Badzian, T. "Diamond Homoepitaxy by Chemical Vapor Deposition". *Diamond and Related Materials. Diamond 1992 Proceedings of the Third International Conference on the New Diamond Science and Technology* **2,** 147–157 (Mar. 31, 1993).

109. Hird J. R., Field J. E. "Diamond Polishing". *Proceedings of the Royal Society of London. Series A: Mathematical, Physical and Engineering Sciences* **460,** 3547–3568 (Dec. 8, 2004).

110. Tatsumi, N., Harano, K., Ito, T., Sumiya, H. "Polishing Mechanism and Surface Damage Analysis of Type IIa Single Crystal Diamond Processed by Mechanical and Chemical Polishing Methods". *Diamond and Related Materials. 9th International Conference on New Diamond and Nano Carbons – NDNC 2015* **63,** 80–85 (Mar. 1, 2016).

111. Derry, T. E., van der Berg, N., Makau, N. W. "Diamond Surfaces Polished Both Mechanically and Manually; an Atomic Force Microscopy (AFM) Study". *Diamond and Related Materials* **17,** 127–136 (Feb. 1, 2008).

112. Volpe, P.-N. *et al.* "Defect Analysis and Excitons Diffusion in Undoped Homoepitaxial Diamond Films after Polishing and Oxygen Plasma Etching". *Diamond and Related Materials* **18,** 1205–1210 (Oct. 1, 2009).

113. Schreck, M., Gsell, S., Brescia, R., Fischer, M. "Ion Bombardment Induced Buried Lateral Growth: The Key Mechanism for the Synthesis of Single Crystal Diamond Wafers". *Scientific Reports* **7,** 44462 (Mar. 15, 2017).

114. Zaitsev, A. M. *Optical Properties of Diamond: A Data Handbook* (Springer Science & Business Media, 2013).

115. Aharonovich, I *et al.* "Diamond-Based Single-Photon Emitters". *Reports on Progress in Physics* **74,** 076501 (July 1, 2011).

116. Himics, L., Veres, M., Tóth, S., Rigó, I., Koós, M. "Origin of the Asymmetric Zero-Phonon Line Shape of the Silicon-Vacancy Center in Nanocrystalline Diamond Films". *Journal of Luminescence* **215,** 116681 (Nov. 1, 2019).

117. Zaitsev, A. M. "Vibronic Spectra of Impurity-Related Optical Centers in Diamond". *Physical Review B* **61,** 12909–12922 (May 15, 2000).

118. Rogers, L. J. *et al.* "Electronic Structure of the Negatively Charged Silicon-Vacancy Center in Diamond". *Physical Review B* **89** (June 2, 2014).

119. Kennedy, T. A., Colton, J. S., Butler, J. E., Linares, R. C., Doering, P. J. "Long Coherence Times at 300 K for Nitrogen-Vacancy Center Spins in Diamond Grown by Chemical Vapor Deposition". *Applied Physics Letters* **83,** 4190–4192 (Nov. 17, 2003).

120. Kurtsiefer, C., Mayer, S., Zarda, P., Weinfurter, H. "Stable Solid-State Source of Single Photons". *PHYSICAL REVIEW LETTERS* **85,** 4 (2000).

121. Wei, C., Manson, N. B. "Observation of the Dynamic Stark Effect on Electromagnetically Induced Transparency". *Physical Review A* **60,** 2540–2546 (Sept. 1, 1999).

122. Santori, C. *et al.* "Coherent Population Trapping in Diamond N-V Centers at Zero Magnetic eld", 9 (2006).

123. Fuchs, G. D. *et al.* "Excited-State Spectroscopy Using Single Spin Manipulation in Diamond". *Physical Review Letters* **101** (Sept. 12, 2008).

124. Taylor, J. M. *et al.* "High-Sensitivity Diamond Magnetometer with Nanoscale Resolution". *Nature Physics* **4,** 810–816 (Oct. 2008).

125. Hall, L. T., Cole, J. H., Hill, C. D., Hollenberg, L. C. L. "Sensing of Fluctuating Nanoscale Magnetic Fields Using Nitrogen-Vacancy Centers in Diamond". *Physical Review Letters* **103** (Nov. 25, 2009).

126. Hall, L. T. *et al.* "Monitoring Ion-Channel Function in Real Time through Quantum Decoherence". *Proceedings of the National Academy of Sciences* **107,** 18777–18782 (Nov. 2, 2010).

127. Ajoy, A., Cappellaro, P. "Stable Three-Axis Nuclear-Spin Gyroscope in Diamond". *Physical Review A* **86** (Dec. 11, 2012).

128. Ledbetter, M. P., Jensen, K., Fischer, R., Jarmola, A., Budker, D. "Gyroscopes Based on Nitrogen-Vacancy Centers in Diamond". *Physical Review A* **86** (Nov. 19, 2012).

129. Rabl, P. *et al.* "A Quantum Spin Transducer Based on Nanoelectromechanical Resonator Arrays". *Nature Physics* **6,** 602–608 (Aug. 2010).

130. Wilson-Rae, I., Zoller, P., Imamoğlu, A. "Laser Cooling of a Nanomechanical Resonator Mode to Its Quantum Ground State". *Physical Review Letters* **92** (Feb. 20, 2004).

131. Yeo, I. *et al.* "Strain-Mediated Coupling in a Quantum Dot–Mechanical Oscillator Hybrid System". *Nature Nanotechnology* **9,** 106–110 (Feb. 2014).

132. MacQuarrie, E. R., Gosavi, T. A., Jungwirth, N. R., Bhave, S. A., Fuchs, G. D. "Mechanical Spin Control of Nitrogen-Vacancy Centers in Diamond". *Physical Review Letters* **111** (Nov. 27, 2013).

133. Teissier, J., Barfuss, A., Appel, P., Neu, E., Maletinsky, P. "Strain Coupling of a Nitrogen-Vacancy Center Spin to a Diamond Mechanical Oscillator". *Physical Review Letters* **113** (July 10, 2014).

134. Kepesidis, K. V., Bennett, S. D., Portolan, S., Lukin, M. D., Rabl, P. "Phonon Cooling and Lasing with Nitrogen-Vacancy Centers in Diamond". *Physical Review B* **88** (Aug. 27, 2013).

135. Shinoda, M. *et al.* "High-Density Near-Field Readout Using Diamond Solid Immersion Lens". *Japanese Journal of Applied Physics* **45,** 1311–1313 (2B Feb. 24, 2006).

136. Siyushev, P. *et al.* "Monolithic Diamond Optics for Single Photon Detection". *Applied Physics Letters* **97,** 241902 (Dec. 13, 2010).

137. Hadden, J. P. *et al.* "Strongly Enhanced Photon Collection from Diamond Defect Centers under Microfabricated Integrated Solid Immersion Lenses". *Applied Physics Letters* **97,** 241901 (Dec. 13, 2010).

138. Marseglia, L. *et al.* "Nanofabricated Solid Immersion Lenses Registered to Single Emitters in Diamond". *Applied Physics Letters* **98,** 133107 (Mar. 28, 2011).

139. Jamali, M. *et al.* "Microscopic Diamond Solid-Immersion-Lenses Fabricated around Single Defect Centers by Focused Ion Beam Milling". *Review of Scientific Instruments* **85,** 123703 (Dec. 2014).

140. Babinec, T. M. *et al.* "A Diamond Nanowire Single-Photon Source". *Nature Nanotechnology* **5,** 195–199 (Mar. 2010).

141. Faraon, A., Barclay, P. E., Santori, C., Fu, K.-M. C., Beausoleil, R. G. "Resonant Enhancement of the Zero-Phonon Emission from a Colour Centre in a Diamond Cavity". *Nature Photonics* **5,** 301–305 (May 2011).

142. Lim, T.-S. *et al.* "Fluorescence Enhancement and Lifetime Modification of Single Nanodiamonds near a Nanocrystalline Silver Surface". *Physical Chemistry Chemical Physics* **11,** 1508 (2009).

143. Tisler, J. *et al.* "Fluorescence and Spin Properties of Defects in Single Digit Nanodiamonds". *ACS Nano* **3,** 1959–1965 (July 28, 2009).

144. Ofori-Okai, B. K. *et al.* "Spin Properties of Very Shallow Nitrogen Vacancy Defects in Diamond". *Physical Review B* **86** (Aug. 13, 2012).

145. Hauf, M. V. *et al.* "Chemical Control of the Charge State of Nitrogen-Vacancy Centers in Diamond". *Physical Review B* **83** (Feb. 14, 2011).

146. Eichhorn, T. R., McLellan, C. A., Jayich, A. C. B. "Optimizing the Formation of Depth-Confined Nitrogen Vacancy Center Spin Ensembles in Diamond for Quantum Sensing". arXiv: 1901.11519 [cond-mat, physics:quant-ph] (Jan. 31, 2019).

147. Becker, J. N., Becher, C. "Coherence Properties and Quantum Control of Silicon Vacancy Color Centers in Diamond". *physica status solidi (a)* **214,** 1700586 (Nov. 2017).

148. Sipahigil, A. *et al.* "Indistinguishable Photons from Separated Silicon-Vacancy Centers in Diamond". *Physical Review Letters* **113** (Sept. 11, 2014).

149. Gianfrani, L., Gagliardi, G., Pesce, G., Sasso, A. "High-Sensitivity Detection of NO2 Using a 740 Nm Semiconductor Diode Laser". *Applied Physics B* **64,** 487–491 (Mar. 1, 1997).

150.   Lee, J. C., Aharonovich, I., Magyar, A. P., Rol, F., Hu, E. L. "Coupling of Silicon-Vacancy Centers to a Single Crystal Diamond Cavity". *Optics Express* **20,** 8891 (Apr. 9, 2012).

151.   Riedrich-Möller, J. *et al.* "Deterministic Coupling of a Single Silicon-Vacancy Color Center to a Photonic Crystal Cavity in Diamond". *Nano Letters* **14,** 5281–5287 (Sept. 10, 2014).

152.   Evans, R. E., Sipahigil, A., Sukachev, D. D., Zibrov, A. S., Lukin, M. D. "Narrow-Linewidth Homogeneous Optical Emitters in Diamond Nanostructures via Silicon Ion Implantation". *Physical Review Applied* **5** (Apr. 18, 2016).

153.   Zhang, J. L. *et al.* "Strongly Cavity-Enhanced Spontaneous Emission from Silicon-Vacancy Centers in Diamond". *Nano Letters* **18,** 1360–1365 (Feb. 14, 2018).

154.   Lemonde, M.-A. *et al.* "Phonon Networks with Silicon-Vacancy Centers in Diamond Waveguides". *Physical Review Letters* **120** (May 25, 2018).

155.   Meesala, S. *et al.* "Strain Engineering of the Silicon-Vacancy Center in Diamond". *Physical Review B* **97** (May 29, 2018).

156.   Jing Wang, Butler, J., Hsu, D., Nguyen, T.-C. *CVD Polycrystalline Diamond High-Q Micromechanical Resonators.* in *Technical Digest. MEMS 2002 IEEE International Conference. Fifteenth IEEE International Conference on Micro Electro Mechanical Systems (Cat. No.02CH37266)* Technical Digest. MEMS 2002 IEEE International Conference. Fifteenth IEEE International Conference on Micro Electro Mechanical Systems (IEEE, Las Vegas, NV, USA, 2002), 657–660.

157.   Hutchinson, A. B. *et al.* "Dissipation in Nanocrystalline-Diamond Nanomechanical Resonators". *Applied Physics Letters* **84,** 972–974 (Feb. 9, 2004).

158.   Imboden, M., Mohanty, P., Gaidarzhy, A., Rankin, J., Sheldon, B. W. "Scaling of Dissipation in Megahertz-Range Micromechanical Diamond Oscillators". *Applied Physics Letters* **90,** 173502 (Apr. 23, 2007).

159.   Gaidarzhy, A., Imboden, M., Mohanty, P., Rankin, J., Sheldon, B. W. "High Quality Factor Gigahertz Frequencies in Nanomechanical Diamond Resonators". *Applied Physics Letters* **91,** 203503 (Nov. 12, 2007).

160.   Najar, H. *et al.* "High Quality Factor Nanocrystalline Diamond Micromechanical Resonators Limited by Thermoelastic Damping". *Applied Physics Letters* **104,** 151903 (Apr. 14, 2014).

161.   Srikar, V., Senturia, S. "Thermoelastic Damping in Fine-Grained Polysilicon Flexural Beam Resonators". *Journal of Microelectromechanical Systems* **11,** 499–504 (Oct. 2002).

162.   Zalalutdinov, M. K. *et al.* "Ultrathin Single Crystal Diamond Nanomechanical Dome Resonators". *Nano Letters* **11,** 4304–4308 (Oct. 12, 2011).

163.   Ovartchaiyapong, P., Pascal, L. M. A., Myers, B. A., Lauria, P., Bleszynski Jayich, A. C. "High Quality Factor Single-Crystal Diamond Mechanical Resonators". *Applied Physics Letters* **101,** 163505 (Oct. 15, 2012).

164.   Burek, M. J., Ramos, D., Patel, P., Frank, I. W., Lončar, M. "Nanomechanical Resonant Structures in Single-Crystal Diamond". *Applied Physics Letters* **103,** 131904 (Sept. 23, 2013).

165.   Fairchild, B. A. *et al.* "Mechanism for the Amorphisation of Diamond". *Advanced Materials* **24,** 2024–2029 (Apr. 17, 2012).

166.   Drumm, V. S. *et al.* "Surface Damage on Diamond Membranes Fabricated by Ion Implantation and Lift-Off". *Applied Physics Letters* **98,** 231904 (June 6, 2011).

167.   Fairchild, B. A. *et al.* "Fabrication of Ultrathin Single-Crystal Diamond Membranes". *Advanced Materials* **20,** 4793–4798 (Dec. 17, 2008).

168.   Aharonovich, I. *et al.* "Homoepitaxial Growth of Single Crystal Diamond Membranes for Quantum Information Processing". *Advanced Materials* **24,** OP54–OP59 (Mar. 8, 2012).

169.   Wu, H. *et al.* "Reducing Intrinsic Energy Dissipation in Diamond-on-Diamond Mechanical Resonators toward One Million Quality Factor". *Physical Review Materials* **2,** 090601 (Sept. 28, 2018).

170.   Tao, Y., Degen, C. "Facile Fabrication of Single-Crystal-Diamond Nanostructures with Ultrahigh Aspect Ratio". *Advanced Materials* **25,** 3962–3967 (Aug. 7, 2013).

171. Héritier, M. *et al.* "Nanoladder Cantilevers Made from Diamond and Silicon". *Nano Letters* **18,** 1814–1818 (Mar. 14, 2018).

172. Burek, M. J. *et al.* "Free-Standing Mechanical and Photonic Nanostructures in Single-Crystal Diamond". *Nano Letters* **12,** 6084–6089 (Dec. 12, 2012).

173. Burek, M. J. *et al.* "High Quality-Factor Optical Nanocavities in Bulk Single-Crystal Diamond". *Nature Communications* **5,** 5718 (Dec. 16, 2014).

174. Atikian, H. A. *et al.* "Freestanding Nanostructures via Reactive Ion Beam Angled Etching". *APL Photonics* **2,** 051301 (May 2017).

175. Sohn, Y.-I., Burek, M. J., Kara, V., Kearns, R., Lončar, M. "Dynamic Actuation of Single-Crystal Diamond Nanobeams". *Applied Physics Letters* **107,** 243106 (Dec. 14, 2015).

176. Bayn, I., Meyler, B., Salzman, J., Kalish, R. "Triangular Nanobeam Photonic Cavities in Single-Crystal Diamond". *New Journal of Physics* **13,** 025018 (Feb. 21, 2011).

177. Riedrich-Möller, J. *et al.* "One- and Two-Dimensional Photonic Crystal Microcavities in Single Crystal Diamond". *Nature Nanotechnology* **7,** 69–74 (Jan. 2012).

178. Khanaliloo, B., Mitchell, M., Hryciw, A. C., Barclay, P. E. "High- Q / V Monolithic Diamond Microdisks Fabricated with Quasi-Isotropic Etching". *Nano Letters* **15,** 5131–5136 (Aug. 12, 2015).

179. Dory, C. *et al.* "Optimized Diamond Quantum Photonics". arXiv: 1812.02287 [`cond-mat, physics:physics`] (Dec. 5, 2018).

180. Wan, N. H., Mouradian, S., Englund, D. "Two-Dimensional Photonic Crystal Slab Nanocavities on Bulk Single-Crystal Diamond". *Applied Physics Letters* **112,** 141102 (Apr. 2, 2018).

181. Wang, C. F. *et al.* "Observation of Whispering Gallery Modes in Nanocrystalline Diamond Microdisks". *Applied Physics Letters* **90,** 081110 (Feb. 19, 2007).

182. Wang, C. F. *et al.* "Fabrication and Characterization of Two-Dimensional Photonic Crystal Microcavities in Nanocrystalline Diamond". *Applied Physics Letters* **91,** 201112 (Nov. 12, 2007).

183. Ummethala, S. *et al.* "High-Q Optomechanical Circuits Made from Polished Nanocrystalline Diamond Thin Films". *Diamond and Related Materials* **44,** 49–53 (Apr. 2014).

184. Mitchell, M. *et al.* "Single-Crystal Diamond Low-Dissipation Cavity Optomechanics". *Optica* **3,** 963 (Sept. 20, 2016).

185. Chia, C. *et al. Diamond Optomechanical Crystals at Cryogenic Temperatures.* in *Conference on Lasers and Electro-Optics* CLEO: Science and Innovations (OSA, San Jose, California, 2018), SF2J.2.

186. Rath, P., Khasminskaya, S., Nebel, C., Wild, C., Pernice, W. H. "Diamond-Integrated Optomechanical Circuits". *Nature Communications* **4** (Dec. 2013).

187. Rath, P. *et al.* "Diamond Electro-Optomechanical Resonators Integrated in Nanophotonic Circuits". *Applied Physics Letters* **105,** 251102 (Dec. 22, 2014).

188. Jayakumar, H., Khanaliloo, B., Lake, D. P., Barclay, P. E. "Cooling and Amplifying Motion of a Diamond Resonator with a Microscope". arXiv: 1810.04196 [`cond-mat, physics:physics`] (Oct. 9, 2018).

189. Mitchell, M., Lake, D. P., Barclay, P. E. "Realizing Q > 300 000 in Diamond Microdisks for Optomechanics via Etch Optimization". *APL Photonics* **4,** 016101 (Jan. 2019).

190. Balram, K. C., Davanço, M., Lim, J. Y., Song, J. D., Srinivasan, K. "Moving Boundary and Photoelastic Coupling in GaAs Optomechanical Resonators". *Optica* **1,** 414 (Dec. 20, 2014).

191. Lu, X., Lee, J. Y., Lin, Q. "High-Frequency and High-Quality Silicon Carbide Optomechanical Microresonators". *Scientific Reports* **5** (Dec. 2015).

192. Lake, D. P., Mitchell, M., Kamaliddin, Y., Barclay, P. E. "Optomechanically Induced Transparency and Cooling in Thermally Stable Diamond Microcavities". *ACS Photonics* **5,** 782–787 (Mar. 21, 2018).

193. Lake, D. P., Mitchell, M., Barclay, P. E. "Demonstration of All–Optical Switching with Bichromatic Cavity Optomechanics". *Frontiers in Optics,* 2 (2018).

Bibliography

194. Mitchell, M., Lake, D. P., Barclay, P. E. *All Optical Control of Pulse Storage Time and Retrieval Phase Using a Diamond Microdisk.* in *Conference on Lasers and Electro-Optics* CLEO: Science and Innovations (OSA, San Jose, California, 2019), STh1H.4.

195. Mitchell, M., Lake, D. P., Barclay, P. E. *Optomechanically Mediated Wavelength Conversion in Diamond Microdisks.* in *Conference on Lasers and Electro-Optics* CLEO: Science and Innovations (OSA, San Jose, California, 2018), SF2J.1.

196. Mitchell, M., Lake, D. P., Barclay, P. E. "Optomechanically Amplified Wavelength Conversion in Diamond Microcavities". arXiv: 1902.07763 [`physics`] (Feb. 20, 2019).

197. Dory, C. *et al.* "Inverse-Designed Diamond Photonics". *Nature Communications* **10,** 1–7 (July 25, 2019).

198. Magyar, A. P. *et al.* "Fabrication of Thin, Luminescent, Single-Crystal Diamond Membranes". *Applied Physics Letters* **99,** 081913 (Aug. 22, 2011).

199. Barson, M. S. J. *et al.* "Nanomechanical Sensing Using Spins in Diamond". *Nano Letters* **17,** 1496–1503 (Mar. 8, 2017).

200. Ovartchaiyapong, P., Lee, K. W., Myers, B. A., Jayich, A. C. B. "Dynamic Strain-Mediated Coupling of a Single Diamond Spin to a Mechanical Resonator". *Nature Communications* **5** (Dec. 2014).

201. Meesala, S. *et al.* "Enhanced Strain Coupling of Nitrogen-Vacancy Spins to Nanoscale Diamond Cantilevers". *Physical Review Applied* **5** (Mar. 18, 2016).

202. Barfuss, A., Teissier, J., Neu, E., Nunnenkamp, A., Maletinsky, P. "Strong Mechanical Driving of a Single Electron Spin". *Nature Physics* **11,** 820–824 (Oct. 2015).

203. Sohn, Y.-I. *et al.* "Controlling the Coherence of a Diamond Spin Qubit through Its Strain Environment". *Nature Communications* **9** (Dec. 2018).

204. Ziegler, J. F., Ziegler, M. D., Biersack, J. P. *SRIM: The Stopping and Range of Ions in Matter* (Ion Implantation Press, 2008).

205. Sun, X., Zhang, X., Tang, H. X. "High- Q Silicon Optomechanical Microdisk Resonators at Gigahertz Frequencies". *Applied Physics Letters* **100,** 173116 (Apr. 23, 2012).

206. Pinto Moura, J. *Making Light Jump: Photonic Crystals on Trampoline Membranes for Optomechanics Experiments* (Delft University of Technology, 2019).

207. Wang, Z., Lee, J., Feng, P. X. L. "Spatial Mapping of Multimode Brownian Motions in High-Frequency Silicon Carbide Microdisk Resonators". *Nature Communications* **5** (Dec. 2014).

208. Graziosi, T., Mi, S., Kiss, M., Quack, N. "Single Crystal Diamond Micro-Disk Resonators by Focused Ion Beam Milling". *APL Photonics* **3,** 126101 (Dec. 2018).

209. Mayer, J., Giannuzzi, L. A., Kamino, T., Michael, J. "TEM Sample Preparation and FIB-Induced Damage". *MRS Bulletin* **32,** 400–407 (May 2007).

210. Schaffer, M., Schaffer, B., Ramasse, Q. "Sample Preparation for Atomic-Resolution STEM at Low Voltages by FIB". *Ultramicroscopy* **114,** 62–71 (Mar. 2012).

211. *The World's Smallest Snowman.* 2009.

212. Bayn, I. *et al.* "Processing of Photonic Crystal Nanocavity for Quantum Information in Diamond". *Diamond and Related Materials* **20,** 937–943 (July 2011).

213. Jung, T. *et al.* "Reproducible Fabrication and Characterization of Diamond Membranes for Photonic Crystal Cavities: Reproducible Fabrication and Characterization of Diamond Membranes". *physica status solidi (a)* **213,** 3254–3264 (Dec. 2016).

214. Babinec, T. M., Choy, J. T., Smith, K. J. M., Khan, M., Lončar, M. "Design and Focused Ion Beam Fabrication of Single Crystal Diamond Nanobeam Cavities". *Journal of Vacuum Science & Technology B, Nanotechnology and Microelectronics: Materials, Processing, Measurement, and Phenomena* **29,** 010601 (Jan. 2011).

215. Martin, A. A., Randolph, S., Botman, A., Toth, M., Aharonovich, I. "Maskless Milling of Diamond by a Focused Oxygen Ion Beam". *Scientific Reports* **5** (Aug. 2015).

216. Scholder, O. *et al.* "Helium Focused Ion Beam Fabricated Plasmonic Antennas with Sub-5 Nm Gaps". *Nanotechnology* **24,** 395301 (Oct. 4, 2013).

217. Gorelick, S., Marco, A. D. "Fabrication of Glass Microlenses Using Focused Xe Beam". *Opt. Express* **26,** 13647–13655 (May 2018).

218. Ding, X *et al.* "Fabrication of a Micro-Size Diamond Tool Using a Focused Ion Beam". *Journal of Micromechanics and Microengineering* **18,** 075017 (July 1, 2008).

219. Nagase, T., Kato, H., Pahlovy, S. A., Miyamoto, I. "Nanosmoothing of Single Crystal Diamond Chips by 1 keV Ar+ Ion Bombardment". *Journal of Vacuum Science & Technology B* **28,** 263–267 (2010).

220. Jamali, M. *et al.* "Microscopic Diamond Solid-Immersion-Lenses Fabricated around Single Defect Centers by Focused Ion Beam Milling". *Review of Scientific Instruments* **85,** 123703 (Dec. 2014).

221. Norris, S. A., Aziz, M. J. "Ion-Induced Nanopatterning of Silicon: Toward a Predictive Model". *Applied Physics Reviews* **6,** 011311 (2019).

222. Toros, A. *et al.* "Precision Micro-Mechanical Components in Single Crystal Diamond by Deep Reactive Ion Etching". *Microsystems & Nanoengineering* **4** (Dec. 2018).

223. Bayn, I. *et al.* "Diamond Processing by Focused Ion Beam—Surface Damage and Recovery". *Applied Physics Letters* **99,** 183109 (2011).

224. Kawasegi, N. *et al.* "Removal and Characterization of Focused-Ion-Beam-Induced Damaged Layer on Single Crystal Diamond Surface and Application to Multiple Depth Patterning". *Diamond and Related Materials* **70,** 159–166 (Nov. 2016).

225. Walker, J. "Optical Absorption and Luminescence in Diamond". *Reports on Progress in Physics* **42,** 1605–1659 (Oct. 1979).

226. Li, L., Schröder, T., Chen, E. H., Bakhru, H., Englund, D. "One-Dimensional Photonic Crystal Cavities in Single-Crystal Diamond". *Photonics and Nanostructures - Fundamentals and Applications* **15,** 130–136 (June 2015).

227. Shaw, K. A., Zhang, Z., MacDonald, N. C. "SCREAM I: A Single Mask, Single-Crystal Silicon, Reactive Ion Etching Process for Microelectromechanical Structures". *Sensors and Actuators A: Physical* **40,** 63–70 (1994).

228. Mi, S., Toros, A., Graziosi, T., Quack, N. "Non-Contact Polishing of Single Crystal Diamond by Ion Beam Etching". *Diamond and Related Materials* **92,** 248–252 (Feb. 2019).

229. Mi, S., Santschi, C., Kiss, M., Martin, O. J. F, Quack, N. *Size Control of Self-Organized Gold Nanoparticles on Nanopatterned Single Crystal Diamond.* in *2018 International Conference on Optical MEMS and Nanophotonics (OMN)* ISSN: (July 2018), 1–5.

230. Lee, D. B. "Anisotropic Etching of Silicon". *Journal of Applied Physics* **40,** 4569–4574 (Oct. 1, 1969).

232. De Theije, F. K., Roy, O., Van der Laag, N. J., Van Enckevort, W. J. P. "Oxidative Etching of Diamond". *Diamond and Related Materials* **9,** 929–934 (2000).

233. Paci, J. T., Schatz, G. C., Minton, T. K. "Theoretical Studies of the Erosion of (100) and (111) Diamond Surfaces by Hyperthermal O(3P)". *The Journal of Physical Chemistry C* **115,** 14770–14777 (Aug. 4, 2011).

234. Stojanović, V. *et al.* "Monolithic Silicon-Photonic Platforms in State-of-the-Art CMOS SOI Processes". *Optics Express* **26,** 13106–13121 (May 14, 2018).

235. Thomson, D. J. *et al.* "50-Gb/s Silicon Optical Modulator". *IEEE Photonics Technology Letters* **24,** 234–236 (Feb. 2012).

236. Harris, N. C. *et al.* "Efficient, Compact and Low Loss Thermo-Optic Phase Shifter in Silicon". *Optics Express* **22,** 10487–10493 (May 5, 2014).

237. Sattari, H. *et al.* "Silicon Photonic MEMS Phase-Shifter". *Optics Express* **27,** 18959–18969 (June 24, 2019).

238. Seok, T. J., Quack, N., Han, S., Muller, R. S., Wu, M. C. "Large-Scale Broadband Digital Silicon Photonic Switches with Vertical Adiabatic Couplers". *Optica* **3,** 64–70 (Jan. 20, 2016).

Bibliography

239. Cocorullo, G., Rendina, I. "Thermo-Optical Modulation at 1.5 Mu m in Silicon Etalon". *Electronics Letters* **28,** 83–85 (Jan. 1992).

240. Johnson, T. J., Borselli, M., Painter, O. "Self-Induced Optical Modulation of the Transmission through a High-Q Silicon Microdisk Resonator". *Optics Express* **14,** 817 (2006).

241. Wang, C. F. *et al.* "Observation of Whispering Gallery Modes in Nanocrystalline Diamond Microdisks". *Applied Physics Letters* **90,** 081110 (Feb. 19, 2007).

242. Lee, J. C. *et al.* "Deterministic Coupling of Delta-Doped Nitrogen Vacancy Centers to a Nanobeam Photonic Crystal Cavity". *Applied Physics Letters* **105,** 261101 (Dec. 29, 2014).

List of common abbreviations

ALD	Atomic Layer Deposition
CVD	Chemical Vapor Deposition
DRIE	Deep Reactive Ion Etching
EDX	Energy Dispersive X-Ray spectroscopy
FIB	Focused Ion Bean
FPC	Fiber Polarization Controller
FSR	Free Spectral Range
GIS	Gas Injection System
ICP	Inductively Coupled Plasma
MEMS	MicroElectroMechanical Systems
µPL	Micro Photoluminescence
NCD	Nano-Crystalline Diamond
PCD	Poly-Crystalline Diamond
PML	Perfectly Matched Layer
RBM	Radial Breathing Mode
RF	Radio Frequency
RMS	Root Mean Square
SCD	Single Crystalline Diamond
SRIM	Stopping and Range of Ions in Matter [204]
TE	Transverse Electric
TEM	Transmission Electron Microscope
TM	Transverse Magnetic
WGM	Whispering Gallery Mode

Images credits

- Figure 3.2[162] Reprinted with permission from Zalalutdinov, M. K., Ray, M. P., Photiadis, D. M., Robinson, J. T., Baldwin, J. W., Butler, J. E., Feygelson, T. I., Pate, B. B., Houston, B. H. "Ultrathin Single Crystal Diamond Nanomechanical Dome Resonators". *Nano Letters* **11,** 4304–4308 (Oct. 12, 2011). Copyright (2011) American Chemical Society.

- Figure 3.2[163] Reprinted from Ovartchaiyapong, P., Pascal, L. M. A., Myers, B. A., Lauria, P., Bleszynski Jayich, A. C. "High Quality Factor Single-Crystal Diamond Mechanical Resonators". *Applied Physics Letters* **101,** 163505 (Oct. 15, 2012), with the permission from AIP Publishing.

- Figure 3.2[51] Reprinted by permission from Springer Nature: Tao, Y., Boss, J. M., Moores, B. A., Degen, C. L. "Single-Crystal Diamond Nanomechanical Resonators with Quality Factors Exceeding One Million". *Nature Communications* **5** (Apr. 8, 2014), Copyright © 2014, Springer Nature

- Figure 3.2[164] Reprinted from Burek, M. J., Ramos, D., Patel, P., Frank, I. W., Lončar, M. "Nanomechanical Resonant Structures in Single-Crystal Diamond". *Applied Physics Letters* **103,** 131904 (Sept. 23, 2013), with the permission of AIP Publishing.

- Figure 3.3[29] Reprinted from Burek, M. J., Cohen, J. D., Meenehan, S. M., El-Sawah, N., Chia, C., Ruelle, T., Meesala, S., Rochman, J., Atikian, H. A., Markham, M., Twitchen, D. J., Lukin, M. D., Painter, O., Lončar, M. "Diamond Optomechanical Crystals". *Optica* **3,** 1404 (Dec. 20, 2016)

- Figure 3.3[183] Reprinted from Ummethala, S., Rath, P., Lewes-Malandrakis, G., Brink, D., Nebel, C., Pernice, W. "High-Q Optomechanical Circuits Made from Polished Nanocrystalline Diamond Thin Films". *Diamond and Related Materials* **44,** 49–53 (Apr. 2014), Copyright (2014), with permission from Elsevier.

- Figure 3.3[25] Reprinted from Khanaliloo, B., Jayakumar, H., Hryciw, A. C., Lake, D. P., Kaviani, H., Barclay, P. E. "Single-Crystal Diamond Nanobeam Waveguide Optomechanics". *Physical Review X* **5** (Dec. 29, 2015).

- Figure 3.3[184] Reprinted from Mitchell, M., Khanaliloo, B., Lake, D. P., Masuda, T., Hadden, J. P., Barclay, P. E. "Single-Crystal Diamond Low-Dissipation Cavity Optomechanics". *Optica* **3,** 963 (Sept. 20, 2016)

Image credits

- Figure 6.2(c) © Sichen Mi.

- Figure 7.3 © Yuji Takabayashi.

List of publications

Over the course of the thesis, I coauthored the following journal articles, conference contributions, and patent applications:

P01 Kiss, M., Graziosi, T., Toros, A., Scharf, T., Santschi, C., Martin, O. J. F., Quack, N. "High Quality Single Crystal Diamond Diffraction Gratings Fabricated by Crystallographic Etching". *Optics Express - in publication*

P02 Sattari, H., Graziosi, T., Kiss, M., Seok, T. J., Han, S., Wu, M. C., Quack, N. "Silicon Photonic MEMS Phase-Shifter". *Optics Express* **27,** 18959–18969 (June 24, 2019)

P03 Mi, S., Toros, A., Graziosi, T., Quack, N. "Non-Contact Polishing of Single Crystal Diamond by Ion Beam Etching". *Diamond and Related Materials* **92,** 248–252 (Feb. 2019)

P04 Toros, A., Kiss, M., Graziosi, T., Sattari, H., Gallo, P., Quack, N. "Precision Micro-Mechanical Components in Single Crystal Diamond by Deep Reactive Ion Etching". *Microsystems & Nanoengineering* **4** (Dec. 2018)

P05 Graziosi, T., Mi, S., Kiss, M., Quack, N. "Single Crystal Diamond Micro-Disk Resonators by Focused Ion Beam Milling". *APL Photonics* **3,** 126101 (Dec. 2018)

P06 Sattari, H., Toros, A., Graziosi, T., Quack, N. *Bistable Silicon Photonic MEMS Switches.* in *MOEMS and Miniaturized Systems XVIII* MOEMS and Miniaturized Systems XVIII. **10931** (International Society for Optics and Photonics, Mar. 4, 2019), 109310D

P07 Quack, N., Seok, T. J., Han, S., Sattari, H., Graziosi, T., Kiss, M., Muller, R. S., Wu, M. C. *Surface Micromachined Silicon Photonic MEMS: A Scalable Technology Platform for Photonic Network Components.* in *Advanced Photonics 2018 (BGPP, IPR, NP, NOMA, Sensors, Networks, SPPCom, SOF) (2018), Paper NeM4F.1* Photonic Networks and Devices (Optical Society of America, July 2, 2018), NeM4F.1

P08 Kiss, M., Graziosi, T., Toros, A., Scharf, T., Martin, O. J. F., Quack, N. *Characterization of Crystallographically Etched Single Crystal Diamond Diffraction Gratings.* in *2018 International Conference on Optical MEMS and Nanophotonics (OMN)* 2018 International Conference on Optical MEMS and Nanophotonics (OMN) (July 2018), 1–2

P09 Graziosi, T., Mi, S., Kiss, M., Quack, N. *Freestanding Optical Micro-Disk Resonators in Single-Crystal Diamond by Reactive Ion Etching and Multidirectional Focused Ion-Beam Milling*. in *Proc. SPIE 10547* Advances in Photonics of Quantum Computing, Memory, and Communication XI (eds Hasan, Z. U., Hemmer, P. R., Migdall, A. L., Craig, A. E.) (SPIE, Feb. 22, 2018), 26

P10 Kiss, M., Graziosi, T., Quack, N. *Trapezoidal Diffraction Grating Beam Splitters in Single Crystal Diamond*. in *Components and Packaging for Laser Systems IV* Components and Packaging for Laser Systems IV. **10513** (International Society for Optics and Photonics, Feb. 20, 2018), 105131K

P11 Graziosi, T., Sattari, H., Seok, T. J., Han, S., Wu, M. C., Quack, N. *Silicon Photonic MEMS Variable Optical Attenuator*. in *MOEMS and Miniaturized Systems XVIII* (ed Piyawattanametha, W and Park, YH and Zappe, H) **10545** (2018)

P12 Graziosi, T., Mi, S., Kiss, M., Quack, N. *Enhancement of Optical Quality Factor by Thermal Annealing of Single Crystal Diamond Micro-Resonators*. in *2018 International Conference on Optical MEMS and Nanophotonics (OMN)* (2018), 20–21

P13 Kiss, M., Graziosi, T., Quack, N. *Demonstration of V-Groove Diffraction Gratings in Single Crystal Diamond*. Sept. 2017

P14 Sattari, H., Graziosi, T., Kiss, M., Seok, T. J., Han, S., Wu, M. C., Quack, N. *Analog Silicon Photonic MEMS Phase-Shifter with Double-Step Electrostatic Actuation*. in *2017 International Conference on Optical MEMS and Nanophotonics (OMN)* 2017 International Conference on Optical MEMS and Nanophotonics (OMN) (Aug. 2017), 1–2

P15 Jacobs, J., Graziosi, T., Kiss, M., Han, S., Scok, T. J., Wu, M. C., Quack, N. *Die Level Release of Silicon Photonic MEMS*. in *2016 International Conference on Optical MEMS and Nanophotonics (OMN)* (2016)

P16 Kiss, M., Graziosi, T., Quack, N., Restori, N. *pat. Method for flattening of substrates using 3D printing and proportional etching - filed 19/10/2019*

P17 Quack, N., Mi, S., Graziosi, T., Toros, A. *pat. Non-contact polishing of single crystal diamond by ion beam etching - filed 27/07/2019*

P18 Quack, N., Toros, A., Kiss, M., Graziosi, T., Gallo, P. *pat. Single crystalline diamond part production method for stand alone single crystalline mechanical and optical component production, WO2019043432A1* (WO) (2019)

P19 Quack, N., Kiss, M., Graziosi, T. *pat. Single crystalline diamond diffractive optical elements and method of fabricating the same, WO2019043570A1* (WO) (2019)

Teodoro Graziosi

Personal Informations

address	Rue de Verdeaux 17B, 1020 Renens
email	teodoro.graziosi@epfl.ch, tgraziosi@protonmail.com
phone	+41 (0)76 47 79 339
date of birth	13th August 1991

Education and Training

November 2015 – December 2019

PhD, *Fabrication and Characterization of Freestanding Single Crystal Diamond and Silicon Microresonators*

Photonics Doctoral School, Q-Lab, EPFL, Switzerland

Design, microfabrication, and characterization of single crystal diamond and single crystal silicon whispering gallery mode microresonators for applications in integrated photonics and optomechanics.

Design of MEMS integrated phase shifters and variable optical attenuators.

Design of measurements setups for the characterization of integrated photonics components.

September 2013 – September 2015

MRes Nanoscale Engineering

INSA Lyon, France

January 2015 – August 2015

Master thesis internship, *Design of a Tunable Optomechanical Cavity*

Gröblacher Lab, TU Delft, Netherlands

Design and simulations of an optomechanical "zipper" cavity for cold atoms experiments. Design of an electrostatic actuator to tune the central wavelength of the optomechanical cavity.

July 2014 – August 2014

Internship, *Coating of Glass Insulators*

EKD Italy, Italy

Characterization of coating techniques of RTV silicone on HV glass insulators.

April 2014 – June 2014

Internship, *Design of Single Photon Avalanche Photodetectors*

INSA Lyon, France

Simulations and optimization of CMOS vertically aligned single photon avalanche photodetectors.

January 2014 – March 2014

Internship, *Integrated Sensor for Monitoring Bruxism*

INSA Lyon, France

Realization of a capacitive sensor integrated within a dental retainer to monitor bruxism activity during sleep.

September 2010 – September 2013	**BSc Materials and Nanotechnology Engineering**
	Politecnico di Milano, Italy
February 2013 – August 2013	**Bachelor thesis internship,** *Synthesis of Graphene by Oxidation and Reduction of Graphite*
	Politecnico di Milano, Italy
	Synthesis and characterization of graphene flakes obtained by chemical oxidation of graphite and reduction of graphene oxide.
September 2007 – June 2013	**Maturità scientifica**
	Scuola Militare "G. Douhet", Firenze, Italy

Personal Skills

mother thongue	Italian
other languages	English
	reading C2, listening C2, speaking C1, writing C2
	French
	reading B2, listening B1, speaking B1, writing B1
skills	Clean room fabrication
	Experience with clean room fabrication on standard and non-standard substrates. Experience with e-beam and photolithography, reactive ion etching, wet etching, sputtering of thin film, atomic layer deposition, focused ion beam, scanning electron microscopy.
	Testing of photonics components
	Design of characterization setup and testing of microresonators on different substrates
	Computer proficiency
	Competent with Microsoft Office, Open Office, Solidworks, Catia, COMSOL, L-edit, Klayout, Inkscape, Photoshop, GIMP, Blender.
	Experience with Inventor, Lumerical, Matlab, Python.
	Oral presentations
	Several scientific conference oral and poster presentations
	Teaching and supervision
	Teaching assistance for Bachelor and Master level classes, supervision of Master semester projects.
	Technical writing
	Contributions as first author or coauthor to scientific papers, contributions to patent applications.
	Team work
	Interaction with other researchers on multiple projects.

other skills and hobbies	I am passionate about photography, travel, indoor climbing, karting and simracing.
driving license	B

Selected Publications

journal articles	Sattari, H., Graziosi, T., Kiss, M., Seok, T.J., Han, S., Wu, M.C., Quack, N., 2019. *Silicon Photonic MEMS Phase-Shifter*. Opt. Express, OE 27, 18959–18969.
	Mi, S., Toros, A., Graziosi, T., Quack, N., 2019. *Non-contact polishing of single crystal diamond by ion beam etching*. Diamond and Related Materials 92, 248–252.
	Graziosi, T., Mi, S., Kiss, M., Quack, N., 2018. *Single crystal diamond micro-disk resonators by focused ion beam milling*. APL Photonics 3, 126101.
	Toros, A., Kiss, M., Graziosi, T., Sattari, H., Gallo, P., Quack, N., 2018. *Precision micro-mechanical components in single crystal diamond by deep reactive ion etching*. Microsystems & Nanoengineering 4.
patents	Quack, N., Kiss, M., Graziosi, T., 2019. *Single crystalline diamond diffractive optical elements and method of fabricating the same*. WO2019043570A1.
	Quack, N., Toros, A., Kiss, M., Graziosi, T., Gallo, P., 2019. *Single crystalline diamond part production method for stand alone single crystalline mechanical and optical component production*. WO2019043432A1.